GEO FOREST CARBON TRACKING

Tasmania National Demonstrator

RADAR PROCESSING METHODOLOGIES FOR THE GENERATION OF WALL-TO-WALL MOSAICS

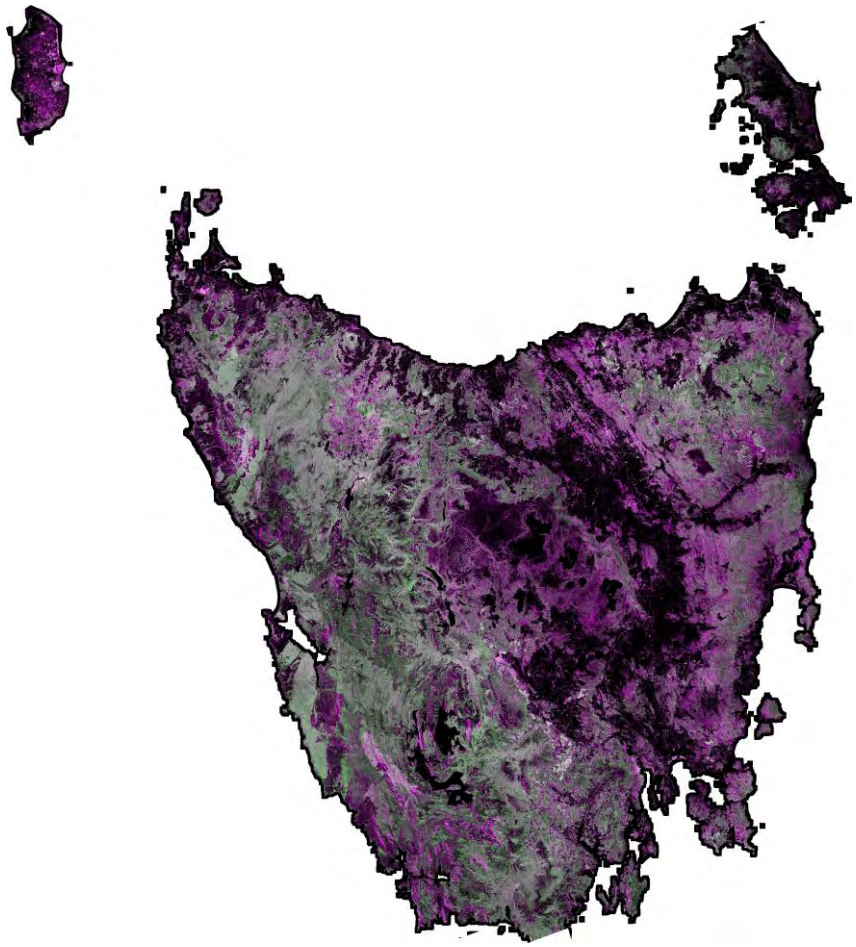

Volume I

Sept 2012

Prepared by IFCI Research Alliance

A.L. Mitchell, I. Tapley, A.K. Milne, M. Williams and K. Lowell

CRC for Spatial Information

Radar processing methodologies for the generation of wall-to-wall mosaics

Editors: Anthea L. Mitchell, Ian Tapley, Anthony K. Milne, Mark Williams, and Kim Lowell

Contributors: Anthea L. Mitchell, Ian Tapley, Anthony K. Milne, Mark Williams, Kim Lowell, Peter Caccetta, Eric Lehmann, Zheng-Shu Zhou, and Alex Held

2012

This document was prepared by members of the International Forest Carbon Initiative Research Alliance (IFCI RA), Australia. The RA was a collaborative effort between scientists from the Cooperative Research Centre for Spatial Information and CSIRO.
It is intended as a guidance document for the calibration and generation of radar mosaics suitable for extraction of forest and land cover information. The processing strategy developed herein is based on R&D undertaken through the Tasmania National Demonstrator program.

For further information, please contact:
Anthea Mitchell (a.mitchell@unsw.edu.au)
Tony Milne (t.milne@unsw.edu.au)

CRC for Spatial Information

TABLE OF CONTENTS

1. RADAR FUNDAMENTALS

This section provides a brief introduction to Synthetic Aperture Radar (SAR) principles, describes the SAR sensors used by the IFCI Research Alliance (RA) in generating forest information products, and describes future SAR sensors for continuous forest measurement.

1.1 Radar theory

RADAR refers to Radar Detection and Ranging and comprises both active and passive, coherent remote sensing systems. Active sensors transmit pulses of microwave energy in a side-looking direction towards the earth's surface, while passive sensors detect the energy reflected from the terrain. The sensor measures the amplitude and phase history of the reflected signal, or backscatter from each target. The magnitude of the backscatter is influenced by both system parameters, including incidence angle, wavelength and polarisation, and surface conditions such as target structure, roughness and dielectric properties (moisture content). Unlike optical sensors, radar emits its own energy and can operate 24 hours a day, independent of solar illumination, and is also cloud-, smoke- and haze-penetrating. The all-weather capability is most beneficial in tropical and sub-tropical regions where cloud cover and rainfall can obscure the terrain.

Synthetic Aperture Radar (SAR) systems were developed to overcome the limitations of Real Aperture Radar (RAR) Systems. The systems differ primarily in the method used to achieve resolution in the azimuth direction (parallel to direction of platform motion). Azimuth resolution improves with longer antennas, and so RAR uses an antenna of maximum practical length to produce a narrow angular beam width in the azimuth direction. SAR on the other hand, uses the motion of the airborne or satellite platform to simulate a large antenna or aperture electronically (Figure 1). The received phase and amplitude components of the signals acquired over successive transmit/receive cycles are processed, taking into account Doppler effects, to generate a high resolution image of the terrain. In this way, SAR can achieve fine resolutions which would otherwise require impractical real aperture antennas with arrays up to 10 m in size.

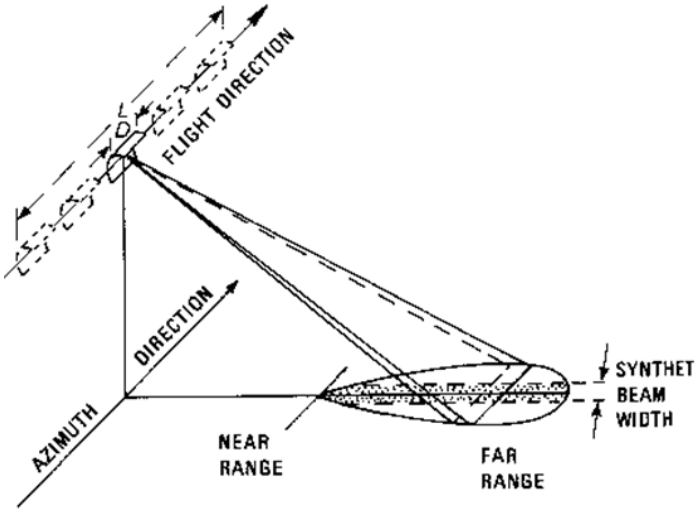

Figure 1. Azimuth resolution of a SAR system. The physical antenna length D is synthetically lengthened to L, by recombining the signals collected over successive transmit/receive cycles with forward movement of the platform. In this way, high resolution images of the terrain are generated.

SAR imaging geometry is complex and characterised differently in range and azimuth directions. The side-viewing geometry of SAR leads to inherent distortions in the data, particularly in the presence of steep topography. These distortions are most severe in the range direction and at near range. The distortions in azimuth are smaller but more complex to circumvent.

Target position is directly related to pulse transit time and the distance between the sensor and target on the ground. The projection of ground targets onto the radar image plane (slant range) results in non-linear compression of the imaged data. In the presence of topography, these distortions are manifest as foreshortening, layover and shadow (Figure 2). Foreshortening occurs when terrain slopes illuminated by side-viewing radar appear compressed in scale (Figure 2a), the effect of which is more pronounced for steeper slopes when observed at steeper incidence angles. Layover is an extreme form of foreshortening or elevation displacement, and occurs when the top of an object is closer to the radar and is imaged before its base (Figure 2b). In imagery, it appears as though the feature has collapsed over towards the radar. Radar shadow occurs in the absence of incident radar illumination (Figure 2c). The occurrence and amount of radar shadow is dependent on imaging parameters including radar look direction, incidence angle and satellite altitude, and terrain features such as orientation and slope. Shadow predominates in terrain viewed at large incidence angles, and the lack of signal return means a loss of thematic information.

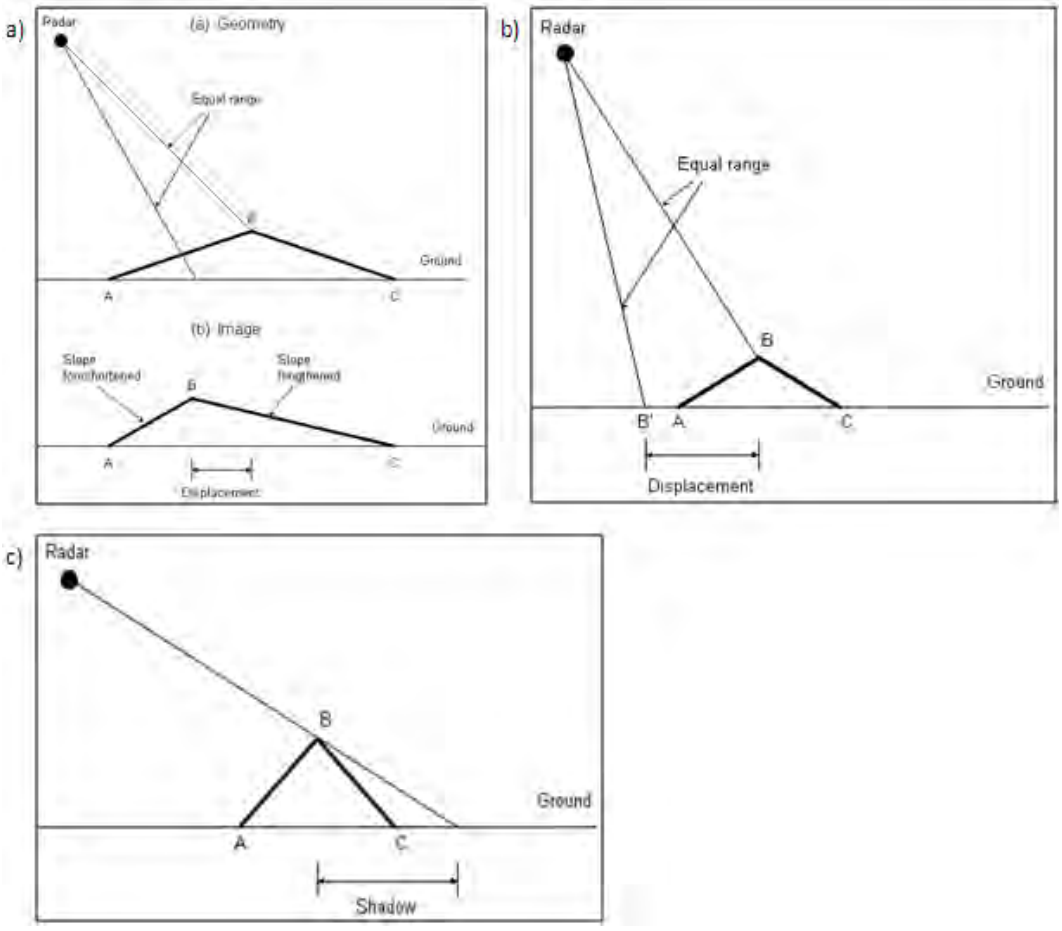

Figure 2. Range distortion in SAR imagery: a) Foreshortening, where terrain slopes appear compressed; b) Layover, where the top of a feature is viewed before its base; and c) Shadow, in the absence of radar illumination (Source: ASAR Glossary Terms, http://envisat.esa.int/handbooks/asar/CNTR5-5.htm#eph.asar.gloss.geo:FORESHORT).

Radar operates in the microwave region of the electromagnetic spectrum (Figure 3). Imaging radars sense in multiple wavelengths, transmitting and receiving polarized energy in wavelengths ranging typically from 3 cm (X-band), 5 cm (C-band), 8 cm (S-band), 24 cm (L-band) and 60 - 100 cm (P-band). Table 1 lists the microwave band designations most commonly used in satellite and airborne SAR systems. The K-band wavelength is comparable in size to rain drops, especially in tropical regions, and is more sensitive to weather conditions. Longer wavelength P-band tends to be increasingly affected and delayed by the ionosphere. Accordingly, most of the satellite SAR systems operate in wavelengths from X- to L-band.

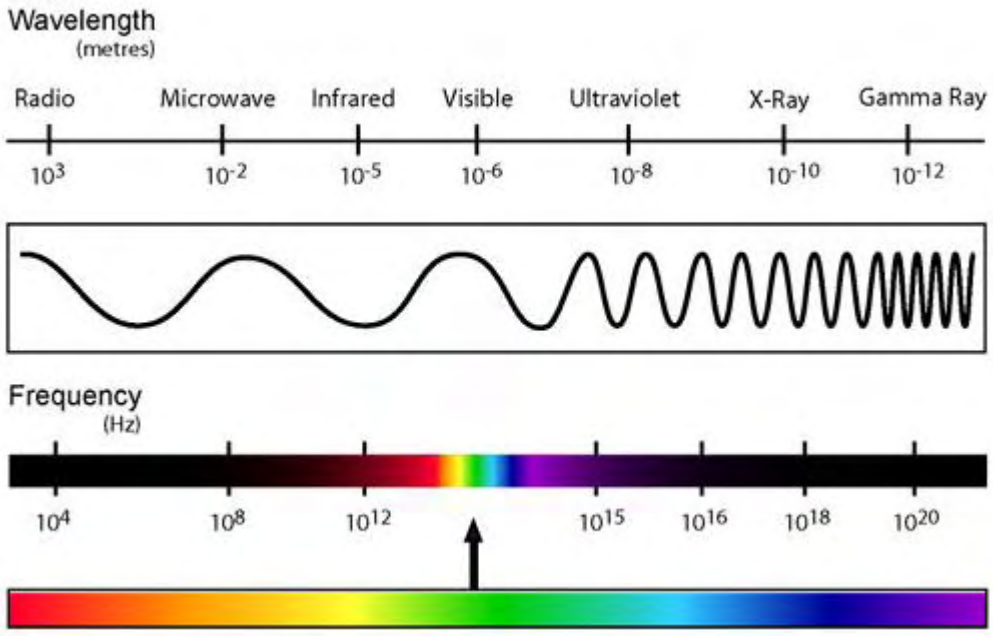

Figure 3. The electromagnetic spectrum (Source: http://labs.ciid.dk/workshops/physical-spectrums-of-perception/attachment/electromagnetic-spectrum/).

Table 1. SAR band allocation and wavelengths.

Band	Wavelength (cm)	Frequency (GHz)
K	1.1 – 1.7	18.5 - 26.5
X	2.4 – 3.8	8 - 12
C	3.8 – 7.5	4 - 8
S	7.5 – 15	2 - 4
L	15 – 30	1 - 2
P	30 – 100	0.3 - 1

Radar waves can penetrate dry materials with low conductivity (low dielectric constant), such as dry sand or snow. Longer wavelengths tend to penetrate deeper through a surface than shorter wavelengths. Radar transmits at a single frequency (or single wavelength) so that the signals are coherent. The backscattered signals from an imaged pixel can act constructively if they are in-phase, i.e., with no phase difference between the signals, or destructively if they are out of phase, i.e., with 180° phase difference between the signals. The constructive and destructive nature of coherent

signals results in the speckle appearing in radar images, and is a key reason why filtering plays an important role in radar image analysis.

Most operational SAR sensors acquire data at a single frequency and in one polarisation mode. Polarisation refers to the orientation of the electric field vectors, which are transmitted or received in either horizontal (H) or vertical (V) directions. Following interaction with the surface, the radar energy returning to the antenna usually maintains the same polarisation as the transmitted pulse, termed parallel, like- or co-polarised imagery (i.e., HH or VV). A proportion of the returning energy is depolarised by surface features, vibrating in various directions and so produces cross-polarised imagery (HV or VH).

Surface roughness strongly influences the strength of the radar return. Smooth surfaces reflect all incident radar energy away from the antenna. Intermediate surfaces reflect part of the incident energy and diffusely scatter the remainder at all angles. Rough surfaces diffusely scatter the incident energy at all angles. Typical radar-surface interactions and the resulting appearance on imagery are illustrated in Figure 4. Bare ground and calm, open water act as specular reflectors, with little return (backscatter) being directed towards the radar, with the resulting surfaces appearing black on co-polarised imagery. Vegetation and wind induced waves have the effect of increasing the surface roughness and so vegetated terrain and ocean signatures appear brighter. Highlights appear on slopes facing the radar, while shadows occur on slopes facing away from the radar. Buildings can induce double bounce scattering where the incident energy reflects off two surfaces (one horizontal, one vertical) appearing quite bright on imagery.

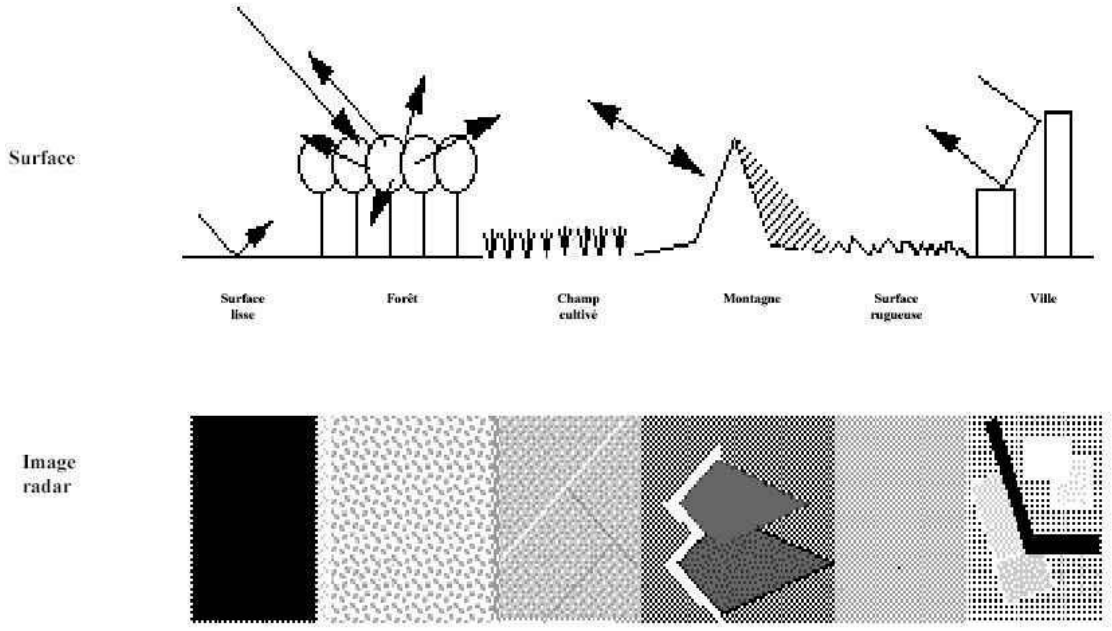

Figure 4. Typical radar-surface interactions and their appearance on imagery.

Radar penetrates vegetation to varying degree depending on the incident wavelength and canopy structure (size and density of components). Short wavelengths (X- and C-band) are diffusely scattered by leaves and small branches in the canopy, while longer wavelengths (L- and P-band) penetrate the canopy and interact with larger branches, trunks and the ground surface (Figure 5). Penetration depth and scattering mechanisms vary with canopy openness and growth stage.

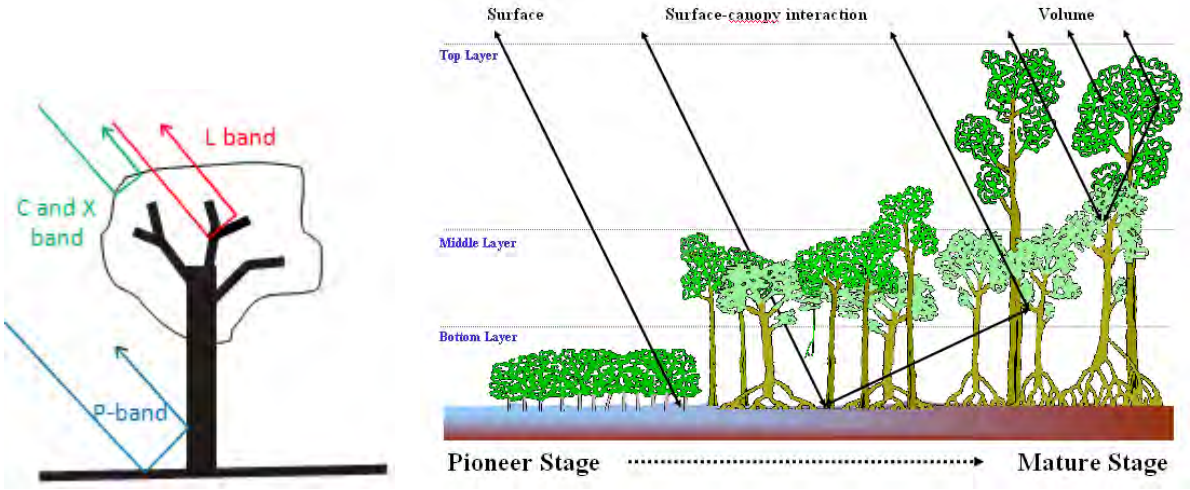

Figure 5. Radar penetration of forest canopies at different wavelengths (Left) and typical scattering mechanisms within forest (Right).

Backscatter is measured in units of area, i.e., the radar cross section (RCS). For science applications, the normalized RCS, or σ°, which is dimensionless, is used (decibels, dB). The backscatter usually ranges between -45 dB (very dark) to 0 dB (very bright).

Used independently, single frequency and single polarisation data are often limited for mapping surface cover. The integration of multi-frequency data from different sensors and both co- and cross-polarised channels can greatly improve the feature extraction capabilities. SAR data often complements optical data acquisition, with each sensor contributing different information about the scene.

1.2 Sources of SAR data used by IFCI RA

Agreements between the Group on Earth Observations (GEO) and CEOS member agencies led to the provision of data for the National Demonstrators (ND). A key objective of the ND program was to evaluate the forest mapping accuracies associated with SAR data acquired at different wavelengths, when used independently and interoperably. For the Tasmania Demonstrator, L-band data was sourced from the Japanese Space Agency's (JAXA) ALOS PALSAR instrument, and C-band data was sourced from RADARSAT-2 and ENVISAT ASAR, provided by the Canadian Space Agency (CSA) and the European Space Agency (ESA) respectively. Historic L-band data was also available from JERS-1 but was not processed due to poor imaging geometry and lack of automated tools to achieve adequate co-registration with the PALSAR data. X-band data from TerraSAR-X was not available within the timeframe of the project but is described below given its high utility in forest information monitoring.

Detailed specifications of these systems are provided in Table 2 below. DLR launched TerraSAR-X in 2007. The instrument is a multi-modal, steerable radar capable of acquiring fine resolution data (1.5 - 3.5 m) over narrow to coarse swaths (10 - 100 km; Figure 6). The satellite is in a near-polar, sun-synchronous orbit at an altitude of 514 km, inclination angle of 97.4° and can revisit each site on the earth's surface at least every 11 days. X-band data can be acquired in spotlight, stripmap or scansar modes, and in single (SP), dual (DP) and quad polarisation (QP). The sensor has left and right looking capability. Incidentally, as a follow-on and extension to TerraSAR-X, TanDEM-X was launched in

2010. Capability is near identical to TerraSAR-X, and when flown together in close formation, they provide interferometric imaging for global DEM generation.

Following on from RADARSAT-1 and to ensure continuity of C-band data, CSA launched RADARSAT-2 into an identical orbit in 2007. The orbit is sun-synchronous, crossing the equator in a southerly direction at dawn and northerly direction at dusk, with the ascending node at 18:00 ±15 min local mean time, and completing 14.3 orbits in 24 hours. Orbit altitude is around 798 km and with inclination angle of 98.6°. Nominal repeat visit time is 24 days. RADARSAT-2 provides improved capabilities in multi-modal imaging and acquisition of data in left or right looking modes (Figure 7). RADARSAT-2 maintains the operating modes of its predecessor and includes new quad polarisation, multilook fine and ultrafine modes.

ESA launched ENVISAT ASAR in 2002. Operating beyond its expected lifetime, communication with the satellite was only lost recently and mission end of life was declared in April 2012. ENVISAT was launched into a sun synchronous orbit at an altitude of 800 km and inclination angle of 98°. Nominal repeat visit time is 35 days. The ASAR instrument acquires C-band data in a variety of imaging modes, including SP image mode, alternating DP, SP wide swath and SP wave mode (Figure 8). Spatial resolution varies from 30 to 1000 m and with swaths ranging from 5 - 100 km wide. Look direction is to the right.

Both JERS-1 and ALOS PALSAR originate from JAXA and operated at L-band. JERS-1 operated between 1992 and 1998 acquiring near global coverage of the earth's surface. The satellite was launched into a sun-synchronous orbit at an altitude of 570 km and inclination angle of 98°. JERS-1 acquires 18 m spatial resolution data in a single polarisation (HH) over a 75 km wide swath. The off-nadir viewing angle ranges between 32 - 38°.

The Advanced Land Observing System (ALOS) was launched in January, 2006, and was considered the continuum satellite to JERS-1. ALOS comprises 3 instruments: the Phase Arrayed L-band SAR (PALSAR), the Advanced Visible and Near Infrared Radiometer type 2 (AVNIR-2) and the Panchromatic Remote Sensing Instrument for Stereo Mapping (PRISM). The satellite was launched into a sun-synchronous orbit at an altitude of 692 km, with a 98.2° inclination angle, and has a revisit time of 46 days. PALSAR acquires data in 3 imaging modes, including fine resolution, polarimetric and wide beam (Figure 9). In these modes, data are acquired at 10 - 20 m, 30 m and 100 m spatial resolution, and over an area of ~70 km, 30 km and 350 km wide respectively. The view angles for the default modes range from 34.3 - 41.5°, 21.5° and 18 - 43° respectively. Global coverage can be achieved annually at fine resolution, every 2 years at selected sites in polarimetric mode, and 1 - 8 times/year using ScanSAR. ALOS-1 ceased operations in May 2011, and ALOS-2 is scheduled for launch in 2013.

Table 2. SAR satellite data sources and system parameters relevant to IFCI RA forest monitoring.

Sensor (Operator)	Operational dates	Orbit alt. (km) Inclin. angle (°) Revisit (days)	Swath width (km)	Spatial resolution (m)	Frequency and operating modes	Incidence angle (°) Look Dir
TerraSAR-X (DLR, Germany)	2007-	514 km 97.4° 11 days			**X-band**	
			10	1.5 - 3.5	Spotlight SP (HH or VV), or DP (HH+HV)	20 - 55
			30	1.7 - 3.5	Stripmap SP or DP (HH+HV or HH+VV or VV+VH)	20 - 45
			100	1.7 - 3.5	ScanSAR SP (HH)	20 - 45 L or R looking
RADARSAT-2 (CSA, Canada)	2007-	798 km 98.6° 24 days			**C-band**	
			20	3	Ultra fine SP	30 - 49
			50	8	Multi-look Fine SP	30 - 50
			50	8	Fine SP/DP	30 - 50
			100	25	Standard SP/DP	20 - 49
			150	30	Wide SP/DP	20 - 45
			300	50	ScanSAR Narrow SP/DP	20 - 46
			500	100	ScanSAR Wide SP/DP	20 - 49
			75	18	Extended High SP	49 - 60
			25	12	Fine QP	20 - 41
			25	25	Standard QP	20 - 41 L or R looking
ENVISAT ASAR (ESA, Italy)	2002-2012	800 km 98° 35 days			**C-band** ASAR	15 - 45 R looking
			100	30	Image SP (VV or HH)	
			100	30	Alternating DP (VV+HH or VV+VH or HH+HV)	
			400	150	Wide swath SP (HH or VV)	
			400	1000	Global monitoring SP (HH or VV)	
			5	30	Wave mode SP (VV or HH)	
ALOS PALSAR (JAXA, Japan)	2006-2011	691 km 98.2° 46 days			**L-band**	
			70	10	Fine Beam Single (HH)	34.3
			70	20	Fine Beam Dual (HH+HV)	34.3
			30	30	Quad pol	21.5
			350	100	ScanSAR (HH)	18 - 43 R looking
JERS-1 (JAXA, Japan)	1992-1998	570 km 98° 44 days	75	18	**L-band** HH	32 - 38 R looking

* DLR – German Space Agency; CSA - Canadian Space Agency; ESA - European Space Agency; JAXA – Japanese Space Agency.

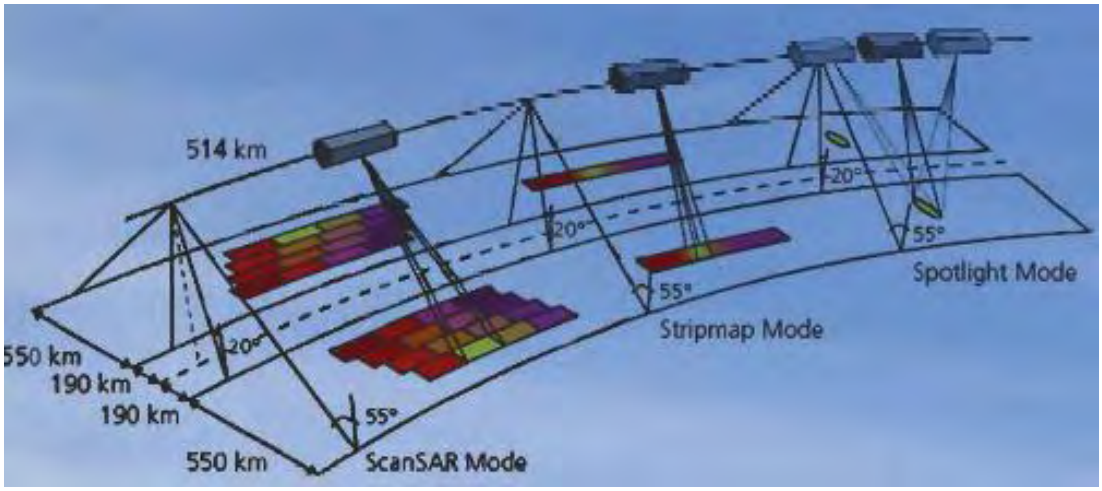

Figure 6. TerraSAR-X default imaging modes (Source: Apogee Imaging International).

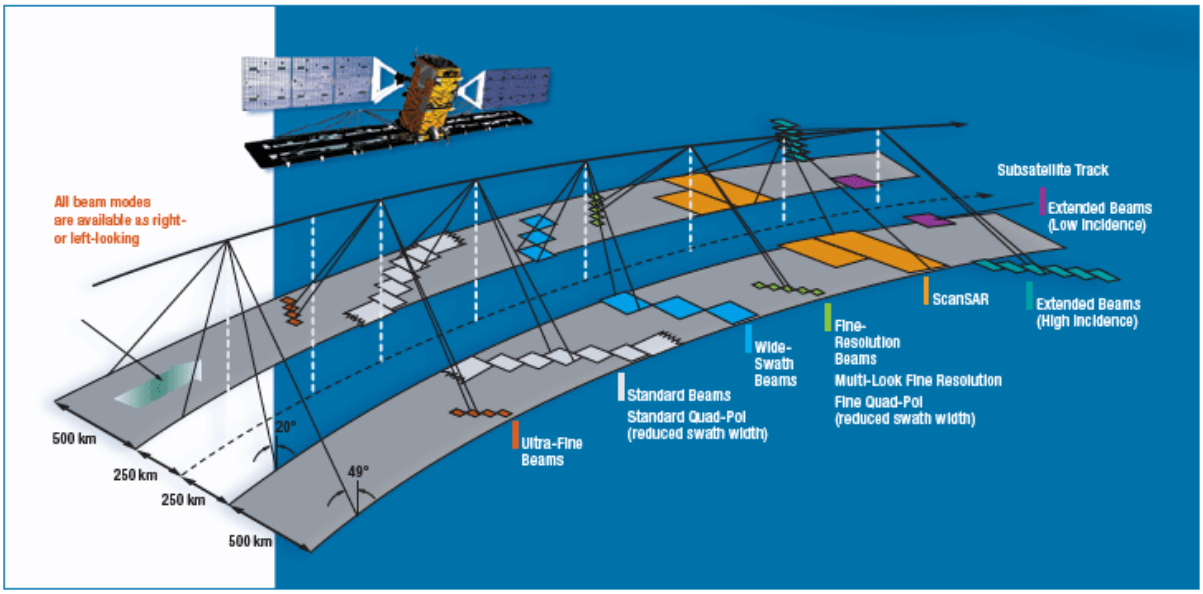

Figure 7. RADARSAT-2 imaging modes
(Source: CSA; http://www.asc-csa.gc.ca/eng/satellites/radarsat2/inf_data.asp)

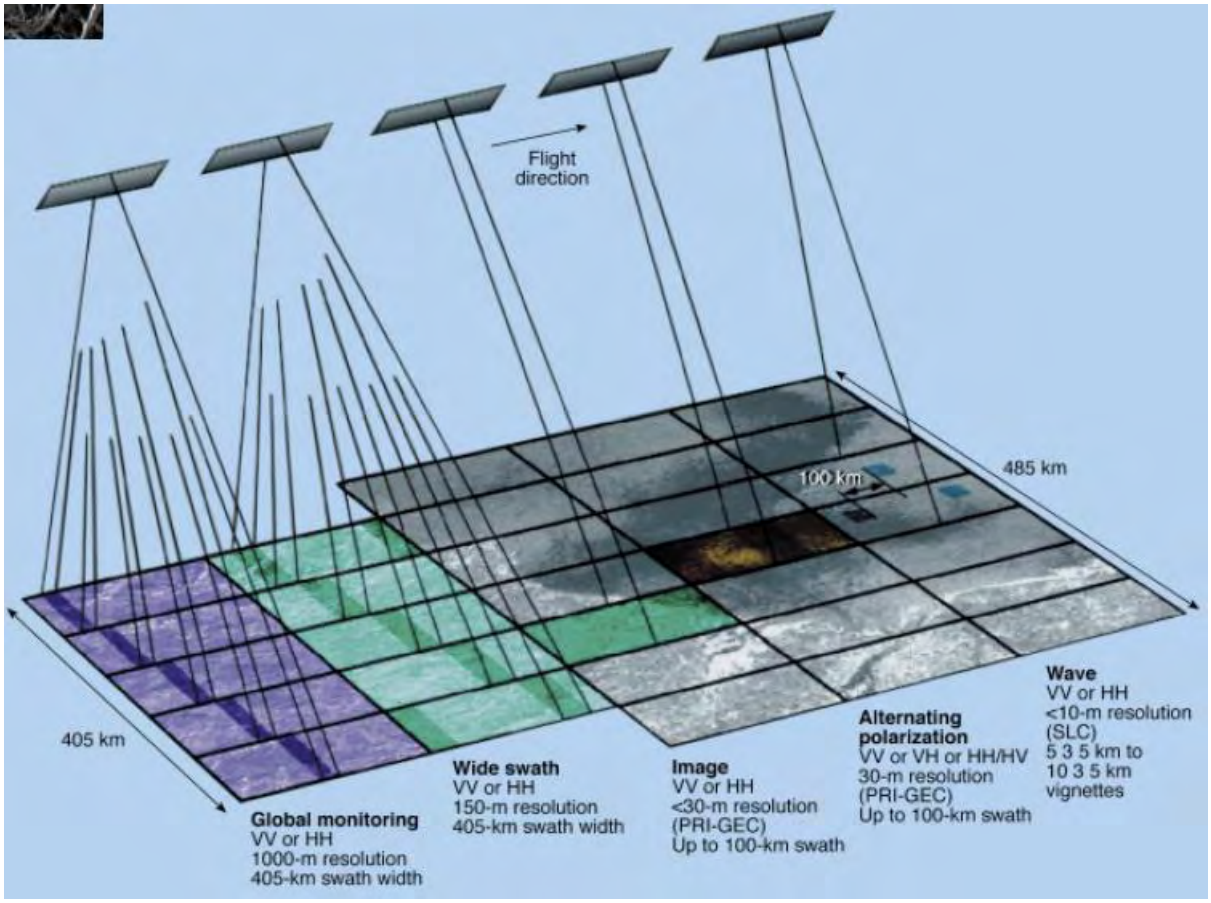

Figure 8. ENIVSAT ASAR imaging modes
(Source: ESA; http://www.esa.int/esapub/bulletin/bullet102/Desnos102.pdf).

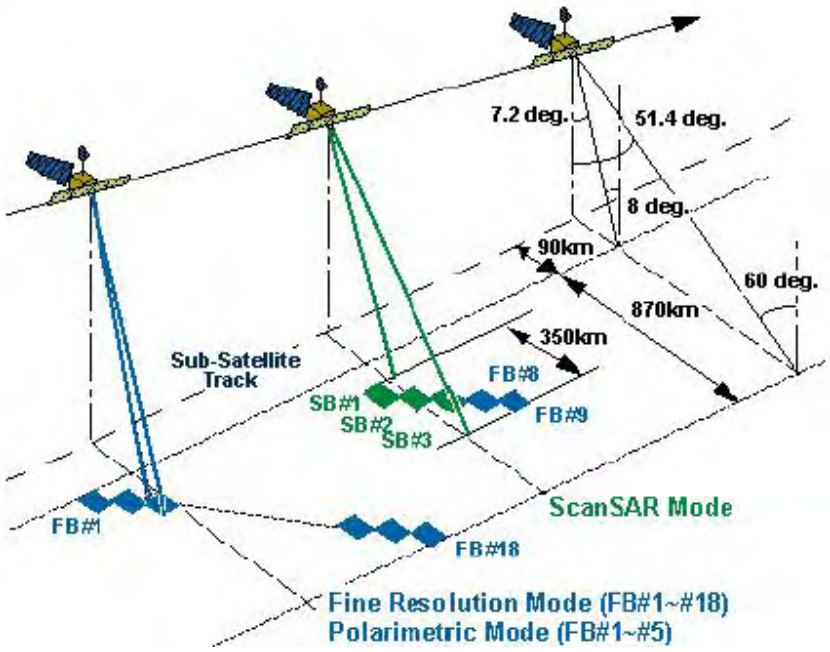

Figure 9. ALOS PALSAR imaging modes
(Source: http://www.eorc.jaxa.jp/ALOS/en/about/palsar.htm).

1.2.1 Specifics of data acquired for the Tasmania Demonstrator

The main SAR data sources used by the IFCI RA include ALOS PALSAR (L-band), RADARSAT-2 and ENVISAT ASAR (C-band; Table 3). A total of 189 Fine Beam Dual (FBD; HH and HV) polarisation ALOS PALSAR images were available between an August to October timeframe for the years 2007 to 2010 (Figure 10). This provided complete, wall-to-wall coverage of Tasmania and a 4-year time-series. Data were acquired on an ascending pass in right-looking mode, at an incidence angle of 34.3° and over a 70 km swath. A total of 51 Fine Beam Single (FBS; HH only) polarisation PALSAR images were available between January and February 2011 (Figure 11). This was the final wall-to wall coverage of Tasmania prior to system failure in April, 2011. Imaging parameters are as for the FBD collect, albeit at slightly finer spatial resolution. Fully Polarimetric data (PLR; HH+HV+VV+VH) were also available over 3 nominated calibration sites. These sites were selected on the basis of variable forest/land cover, terrain and land use history, and were visited in Sept/Oct 2010 as part of a ground truth campaign. A total of 9 images were available, acquired on an ascending pass and in right-looking mode, at an incidence angle of 21.5° and over a 30 km swath (Figure 12).

Table 3. SAR data available for the Tasmania Demonstrator.

Sensor	Mode	Availability	Incidence angle (°)	Spatial resolution (m)	Swath width (km)
		L-BAND			
ALOS PALSAR	FBD (HH+HV) Asc., R looking	189 images Aug-Oct 2007-2010	34.3	9.37 rng x 3.13 az (1 look)	70
	FBS (HH) Asc., R looking	51 images Jan-Feb 2011	34.3	4.68 rng x 3.13 az (1 look)	70
	PLR (HH+HV+VV+VH) Asc., R looking	9 images Mar-Apr 2007, Mar 2011 (Takone) May 2007 (Mathinna) Apr 2011 (Warra)	21.5	9.37 rng x 3.49 az (1 look)	30
		C-BAND			
RADARSAT-2	W3 (VV+VH) Asc., R looking	34 images July-Dec 2009 4 images Jan 2010	39 - 45	13.5 rng x 7.7 az (1 look)	120
ENVISAT ASAR	AP IS4 (VV+VH) Desc., R looking	18 images July-Sept 2009	34	7.8 rnge x 4 az (1 look)	56 - 100

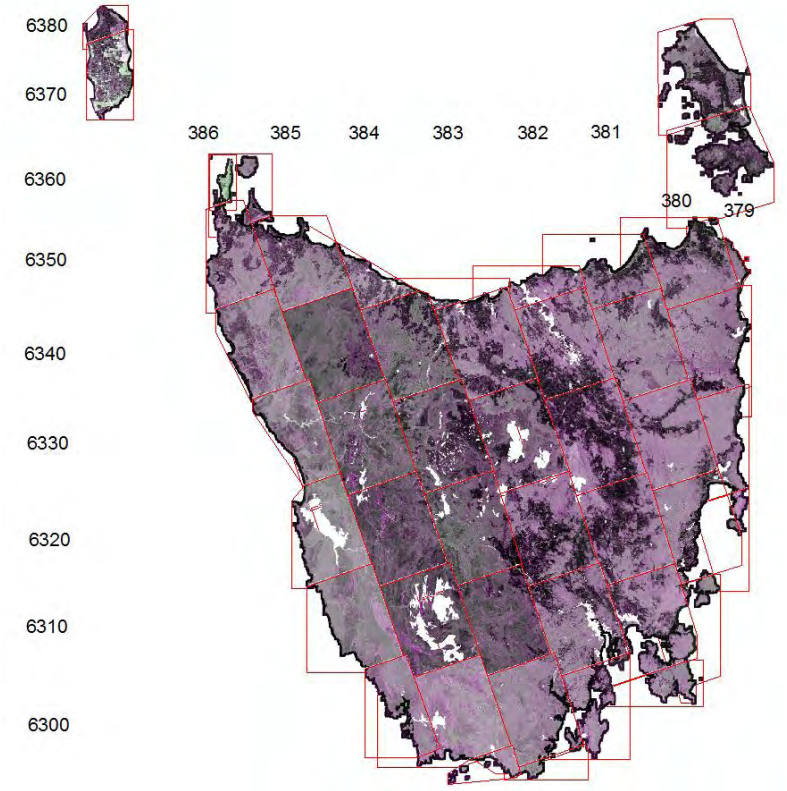

Figure 10. ALOS PALSAR Fine Beam Dual (FBD) polarisation coverage of Tasmania: FBD image extents for 2007 - 2010 (Paths: 379 - 283, Rows: 6300 - 6380).

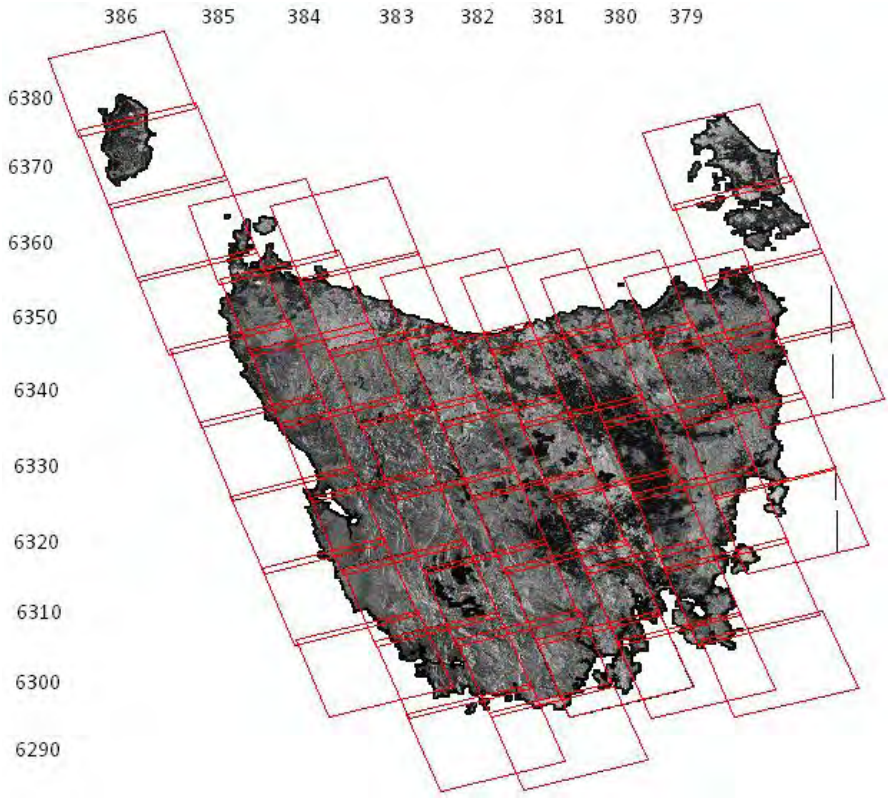

Figure 11. ALOS PALSAR Fine Beam Single (FBS) coverage of Tasmania: FBS image extents for 2011.

Figure 12. ALOS PALSAR full polarimetric (PLR) coverage over calibration sites in Tasmania: PLR image extents for 2007 and 2011.

A total of 34 RADARSAT-2 images were acquired over Tasmania, with the majority (30) acquired during July to December, 2009, and 4 images acquired in January 2010. The 2009 data provided complete wall-to-wall coverage of Tasmania (Figure 12). Dense time-series data were available over the 3 calibration sites. Data were acquired in Wide Swath Beam 3 mode (W3) on an ascending pass in right-looking mode, at an incidence angle of between 39 – 45° and over a 120 km swath.

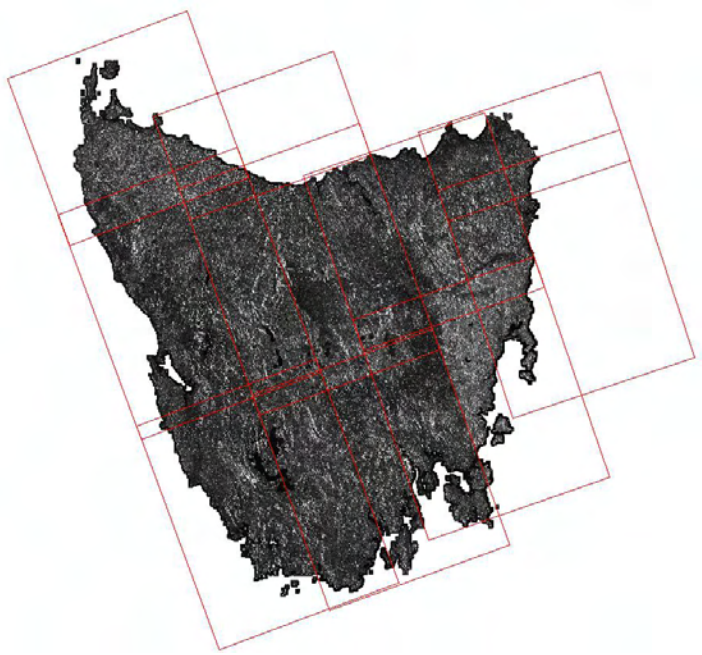

Figure 12. RADARSAT-2 Wide Swath Beam 3 (W3) coverage of Tasmania: W3 image extents for 2009.

A total of 18 ENVISAT ASAR images were acquired during July to September 2009. Data were acquired on a descending pass in right-looking mode, at an incidence angle of 34° and over a 81 km swath (Figure 13). This provided 1 complete wall-to-wall coverage of Tasmania for 2009.

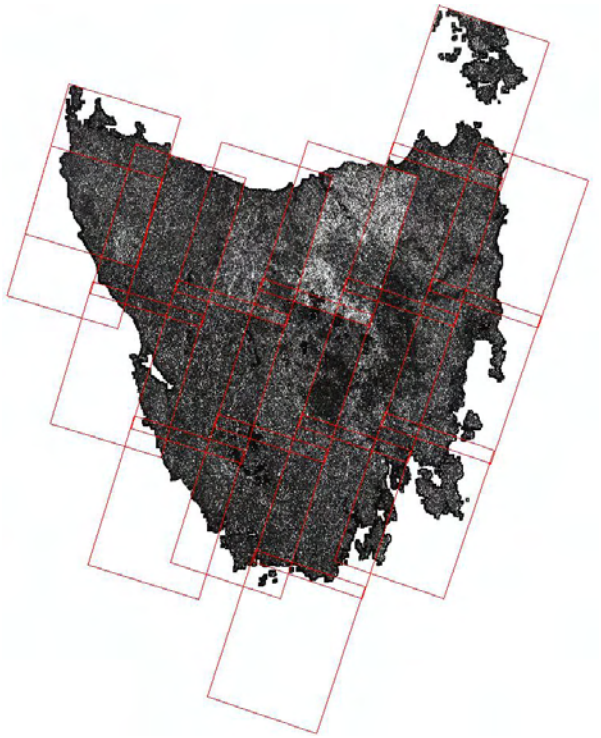

Figure 13. ENVISAT ASAR Alternating Polarisation (AP) coverage of Tasmania: AP mode image extents for 2009.

1.2.2 Future SAR data sources for operational forest monitoring

A number of proposed satellite SARs will ensure continuity of data for operational forest monitoring (Table 4). Numerous space agencies worldwide are committed to future launches for continuity of operational programs and exploration of new imaging technologies. These include continuity C- and X-band missions and a second L-band PALSAR system. Both S- and P-band systems have also been proposed.

Ongoing access to C-band SAR data seems ensured with the proposed CSA Radarsat Constellation Mission (RCM) and ESA's Sentinel program if these systems proceed to launch. The RCM comprises 3 EO satellites with probable launch dates of 2014 (C1 and C2) and 2015 (C3) and expected lifetime of around 7 years. Following on from RADARSAT-2, data will be acquired in multiple imaging modes at low-high resolution to suit a diversity of applications. ESA's Sentinel-1 mission comprises 2 C-band satellites, with a third under consideration, with anticipated launch dates of 2013 (1A), 2015 (1B) and 2019 (1C). Given ESA's open data policy, free access to C-band data will continue.

Continuing access to X-band SAR data also seems ensured, with DLRs proposed TerraSAR-X2. DLR has indicated a commercial follow-on to the existing TerraSAR-X mission, with a proposed launch in 2015. TerraSAR-X2 will acquire fine to medium resolution data (1 – 50 m) in spotlight, stripmap and scansar modes.

SSTL in the UK have developed an S-band system NovaSAR-S for launch in 2013. It can be launched into either a sun-synchronous or low inclination equatorial orbit. NovaSAR-S provides moderate resolution data (6 – 30 m), suitable for a range of natural resource and disaster management applications.

Regarding an L-band continuation, JAXA has approved ALOS PALSAR-2 for launch in 2013. However, the data access policy has not yet been determined. PALSAR-2 will provide additional quad and circular polarimetry imaging modes, and shorter revisit times in scansar wide and fine modes of operation. DLR, in partnership with NASA JPL, is also considering a TanDEM-L satellite as a complement to their current X-band constellation.

There is the potential for the supply of P-band data through ESA's BIOMASS initiative if this is chosen for development and launch in the 2016+ time period.

Table 4. Future/proposed satellite SARs of relevance to forest monitoring.

Sensor (Operator)	Operational dates	Orbit alt. (km) Inclin. angle (°) Revisit (days)	Swath width (km)	Spatial resolution (m)	Operating modes	Incidence angle (°) Look Dir
			X-BAND			
TerraSAR-X2 (DLR)	2015-2018		 10 – 40 50 – 500	0.5 1 – 4 5 – 50	Spotlight Stripmap ScanSAR	
			C-BAND			
RADARSAT Constellation mission (RCM) C-1, C-2, C-3 (CSA)	C1 2014-2021 C2 2014-2021 C3 2015-2022	592.7 km 97.74° 12 days	 500 350 30 125 30 20 350 350	 100 50 16 30 5 3 100 variable	HH,VV,HV,VH Low resolution Med resolution (maritime) Med resolution (land) Med resolution (land) High resolution Very high resolution Ice/oil low noise 25 m ship mode	 19 – 54 19 – 58 20 – 47 21 – 47 19 – 54 18 – 54 19 – 58 19 – 58 R looking
Sentinel-1 A,B,C (ESA)	A 2012-2020 B 2014-2022 C 2019-2026	693 km 98.18° 12 days	 80 250 400	 5 5 x 20 20 x 40 5	VV+VH, HH+HV Stripmap Interferometric wide swath Extra wide swath Wave mode	20 – 45
			S-BAND			
NovaSAR-S (SSTL)	2013-2020	580 km Daily – 4 days	 15 – 20 100 150 750	 6 20 30 30	SP/DP/TP Stripmap Scansar Scansar wide Maritime surveillance	 16 – 34 16 – 30 15 – 31 48 – 73
			L-BAND			
ALOS PALSAR-2 (JAXA)	2013 – 2017	628 km 97.9° 14 days	25 50 50	3 3 6	Spotlight SP Ultra Fine SP/DP High sensitive SP/DP/QP/CP	30 – 44 L or R looking

		66 days	70	10	Fine SP/DP/QP/CP	
		42 days	350	100	Scansar nominal SP/DP	
		14 days	490	60	Scansar wide SP/DP	
TanDEM-L (DLR)	2017 – 2022	760 km 8 days	350	20 – 100	Single-pass InSAR Polarimetry QP Wide swath mode	26.3 – 46.6
			P-BAND			
BIOMASS (ESA)	2016 – 2021	642 km 25 – 45 days	60 105	50	InSAR QP Stripmap Scansar	23 – 32 L or R looking

2. SAR DATA SELECTION, PROCESSING AND SOFTWARE

This section describes standard data formats and typical processing steps applied to SAR data. Data selection is discussed, with recommendations for the timing of acquisition and application dependency. Available software for the processing of SAR data is also outlined.

2.1 SAR processing flow

A typical processing sequence applied to SAR data is illustrated in Figure 14. Further details of individual processing steps will be dealt with in subsequent sections. Single Look Complex (SLC) data are typically acquired for scientific use, and require specialist software to process. Data import functions vary depending on the type of data and level of processing. Multi-looking is applied to reduce speckle noise and obtain approximately square pixels. Multi-looked intensity data can be co-registered if multiple images are available over the same area for different dates. Single or multi-date filtering can be applied to reduce image speckle and preserve or enhance certain features.

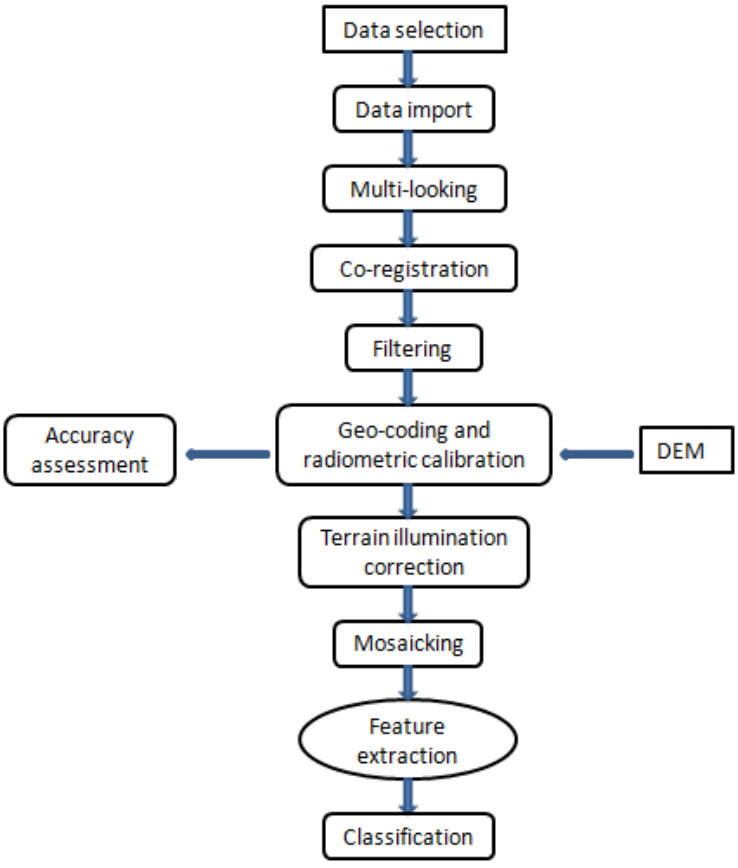

Figure 14. Typical processing sequence applied to radar data.

Geocoding (or orthorectification) is performed with the use of a Digital Elevation Model (DEM) to associate pixels with map coordinates. Geo-location accuracy is typically assessed using Ground Control Points (GCPs) sourced in the field using differential GPS or from data of known higher positional accuracy. Radiometric calibration is applied to counter systematic noise and normalise intensity data to facilitate comparison between images acquired at different times. When appropriate, Terrain Illumination Correction (TIC) is applied to correct the brightness variations resulting from topography and SAR viewing geometry.

Orthorectified, radiometrically corrected, and terrain illumination corrected intensity data are then mosaicked to produce path mosaics or wall-to-wall mosaics. With the completion of this sequence of steps, the SAR data are now ready for analysis. Feature extraction and methods for the generation of forest information products from radar mosaics are outlined in Volume II "Radar processing methodologies for generation of forest information products".

2.2 Data selection

SAR data is heavily influenced by dielectric properties and variations in backscatter may be evident within and between strip data or single scene products acquired during or after rainfall events. This banding is problematic when generating regional mosaics and for those studies reliant on consistent backscatter relationships, e.g., land cover mapping and retrieval of biophysical attributes such as biomass. Increased soil and/or canopy moisture can enhance the backscatter signal by a few dB. As such, only those images acquired under dry or like conditions should be used to create a seamless mosaic.

A case study from Queensland, Australia, published by Lucas *et al.* (2010) highlights the importance of data selection with reference to environmental conditions for the compilation of wide-area mosaics. ALOS PALSAR strip data acquired as part of the Kyoto and Carbon (K&C) Initiative have been used to generate relatively seamless mosaics for many areas worldwide, but several strips acquired over northern Australia had noticeably higher backscatter values compared to neighbouring strips despite implementation of appropriate across track correction routines (Figure 15). Reference to meteorological records and satellite measurements of soil moisture and vegetation water content suggested that rainfall during or several days prior to image acquisition and subsequent rates of evapotranspiration were primarily responsible.

It was not possible to correct the backscattering coefficient because of the high variability in these meteorological parameters. Their solution involved using data from dry periods only, either from 1 year or several, and resulted in a mosaic with relative consistency in data values (Figure 16). The results demonstrate the importance of consulting meteorological data acquired at ground stations or as measured by spaceborne sensors (e.g., AMSR-E and SILO) prior to scene selection, particularly in areas with irregular rainfall and evapotranspiration.

Images may also have been acquired several weeks apart, depending on the revisit time of the sensor. The ALOS PALSAR, for example, has a 46-day repeat cycle and it is therefore possible that real on-ground change could have occurred in the overlapping area of adjacent images acquired on different dates. The change may be in the form of, for example, increased soil moisture due to rainfall or a flood event, or a change in spectral or textural properties due to crop/canopy growth or a change in land cover, e.g., clear felling of timber. It may be necessary to exclude the area of overlap or use averaging techniques when creating the mosaic.

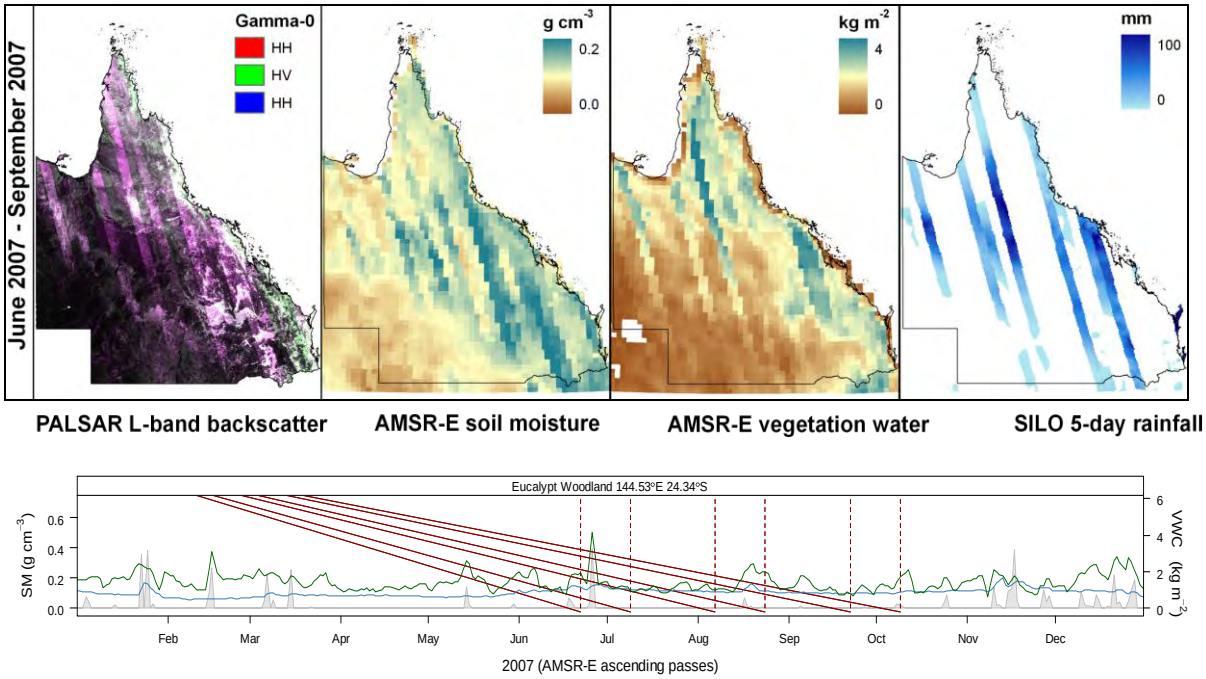

Figure 15. The importance of environmental conditions on data selection: independent comparison of PALSAR strip data with surface moisture and rainfall data (Source: R. Lucas, University of Wales).

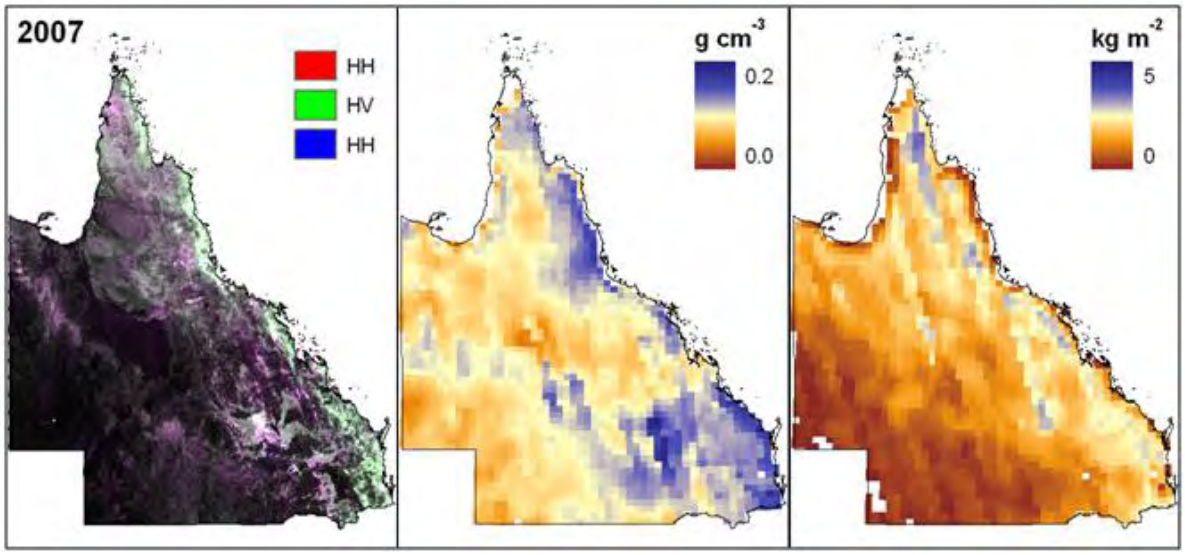

Figure 16. Generation of annual (2007) PALSAR mosaic for Queensland, Australia, using strip data captured under the driest conditions (Source: R. Lucas, University of Wales).

2.3 SAR data and formats

SAR products are available as framed scenes or continuous strip data, and in unprocessed (level 1.0; raw signal), partially processed (level 1.1; single look complex) or fully processed form (level 1.5 and above; geo-coded products or mosaics).

Standard SAR product specifications have been formulated by the Committee on Earth Observation Satellites (CEOS). CEOS comprises representatives of numerous international organisations engaged

in earth observation, and provides a forum for the exchange of ideas and technical information. Working groups were established to tackle issues such as mission coordination, future sensors, data and calibration.

Standard formats for storage and delivery of image data include Hierarchical Data Format (HDF), GeoTIFF, and the CEOS Superstructure format, which is widely used for SAR data (http://wgiss.ceos.org/archive/archive.pdf/sardata.pdf). Although widely adopted, the CEOS format has been modified by various Space Agencies (e.g., ESA, NASDA), often leading to software incompatibilities. The basic CEOS format comprises a volume directory (descriptive file management information), leader file (annotation data, ancillary and other data), image file (image data), trailer file (quality control and final information related to image data) and null volume directory. The actual image data can be stored as Band Interleaved by Pixel (BIP), Band Interleaved by Line (BIL) or Band Sequential (BSQ). Data products generated from ERS-1, SIR-C/X-SAR, JERS-1, RADARSAT and ALOS PALSAR are supplied in CEOS format. Individual agencies should be contacted for specific documentation on product formats and software.

2.4 Software for processing SAR data

Mainstream image processing packages such as ENVI and Imagine comprise radar processing modules, with basic processing functionality. ENVI also has a specialised add-on module for SAR/InSAR processing called SARscape. GAMMA and Geomatica packages are also available for specialised SAR processing. Free radar processing toolkits and viewers are available through the European Space Agency (ESA).

SARscape is an add-on module to the mainstream ENVI/IDL package, and available through Exelis VIS (http://www.exelisvis.com). The module was developed by the Swiss company Sarmap (http://www.sarmap.ch/), and provides pre-processing functions for all product levels, and interferometric and polarimetric processing capability for both airborne and spaceborne SAR data.

ENVI SARscape was the software of choice by the IFCI RA for processing of SAR data acquired over the Tasmania National Demonstrator. It facilitated the full suite of processing from SLC to a radiometrically calibrated and orthorectified product, suitable for extracting forest cover information. The processing sequence and examples provided throughout this chapter are the direct result of processing within the ENVI/SARscape environment.

Gamma SAR was developed by Gamma Remote Sensing (http://www.gamma-rs.ch/software/). It comprises a number of modules for processing SAR data, interferometric SAR (InSAR) and differential SAR (DInSAR) data. Processing of raw signal and higher level data products is supported.

PCI Geomatica (http://www.pcigeomatics.com) comprises core image processing functions as well as featuring a radar suite for advanced processing of airborne and spaceborne SAR data. Image enhancement, filtering, orthorectification, SAR coherent change detection, polarimetric analysis and mosaicking functions are supported.

ESA has developed a number of free toolboxes for processing of SAR data (http://earth.esa.int/resources/softwaretools/). These are available as a complement to the processing capabilities within mainstream packages. POLSARPRO facilitates the processing of polarimetric data. BEAM provides viewing and analysis capabilities for SAR and optical data. BEST was developed for processing of Envisat ASAR and ERS-1/2 AMI data. NEST provides tools for visualisation, analysis, orthorectification and mosaicking of various SAR data.

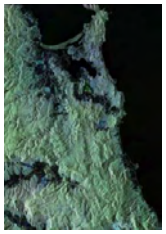

3. DATA IMPORT, MULTI-LOOKING AND CO-REGISTRATION

This section describes SAR data pre-processing functions including data import, multi-looking to produce quasi-square pixels, and co-registration of multi-date data. Examples in this and subsequent sections illustrate processing of ALOS PALSAR data only. Other SAR data including RADARSAT-2 and ASAR are similarly processed, with some modification of input parameters. All image examples are the result of processing using ENVI SARscape v4.3.

3.1 Supported data formats

All software packages are different and support for specific data types and formats varies. The relevant product guide should be consulted for detailed information regarding support of data acquired by particular sensors and for different processing levels.

SAR data is typically read directly by the software or imported through a dedicated import function. ENVI SARscape supports the import of ENVI format files, single layer generic binary, shapefiles and other standard formats for ALOS PALSAR (ERSDAC and JAXA CEOS formats), ENVISAT ASAR, ERS-1/-2 SAR, Cosmo-SkyMed, JERS-1, RADARSAT and TerraSAR-X. If available, precise orbital information such as DORIS for ENVISAT ASAR can be imported in the same step.

When importing data in one of the SARscape supported standard formats (e.g., Figure 17), the following input parameters are required: sensor, data type (acquisition mode and processing level), and the version (typically default, or that adopted by a particular data provider). Path names, image data and header files are also specified. SARscape generates its own header files through the import process. These include:

i. SARscapeParameterExtracted.sml – temporary processing parameters
ii. .xml – geographic coordinates of scene corners
iii. .shp – shape file and headers (.sml, .hdr) with image perimeter
iv. .kml – ascii file with image perimeter for automatic location in Google Earth.

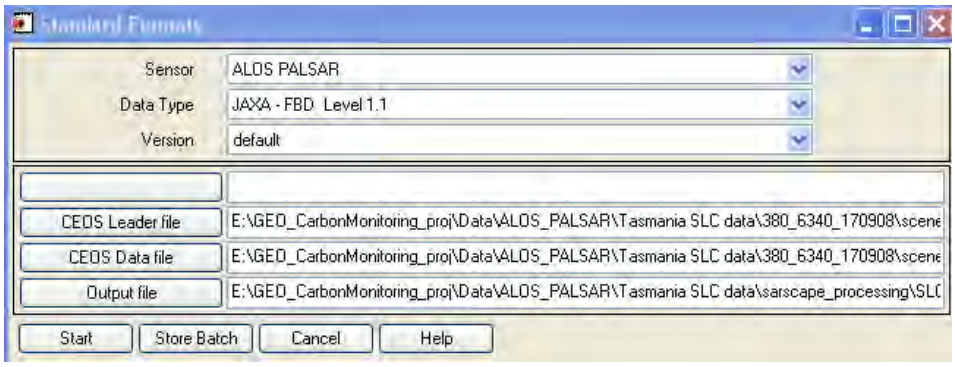

Figure 17. Importing PALSAR FBD data through the standard data import utility in SARscape.

DEMs, SAR derived classifications, coherence and other single layer data in ENVI format should be imported through the ENVI Original menu. The imported image and corresponding header files (.sml and .hdr) will be created in the process. The input and output file name must be specified, together with the data units and dummy (no data) value. Data unit options include classification, coherence, DEM, DEM slope, digital number, intensity and amplitude.

3.2 Multi-looking

The full SAR signal data can be used to produce the highest resolution Single Look Complex (SLC) product. SLC data are quite noisy however, and multi-looking is applied to improve the radiometric resolution, albeit at the expense of spatial resolution, and change the grid cell (pixel) size. Multi-looked intensity images are generated by averaging over the range and azimuth cells to obtain approximately square pixels. The intended spatial resolution of the geocoded product should be taken into account when selecting the number of looks.

Following successful import of data using SARscape, the appropriate multi-looking factors can be calculated automatically using the 'Looks' button (Figure 18). The user must first set the output cartographic grid size (i.e., pixel size in metres of the geocoded product) in the SARscape Default values panel. As an example, the best spatial resolution that can be achieved using ALOS PALSAR Fine Beam Dual (FBD) polarisation data is around 15 m. In order to process a quasi-square pixel approximating 12.5 m, multi-looking using 1 look in range and 4 looks in azimuth is appropriate. The output pixel size in this example is 14.9 x 12.5 m.

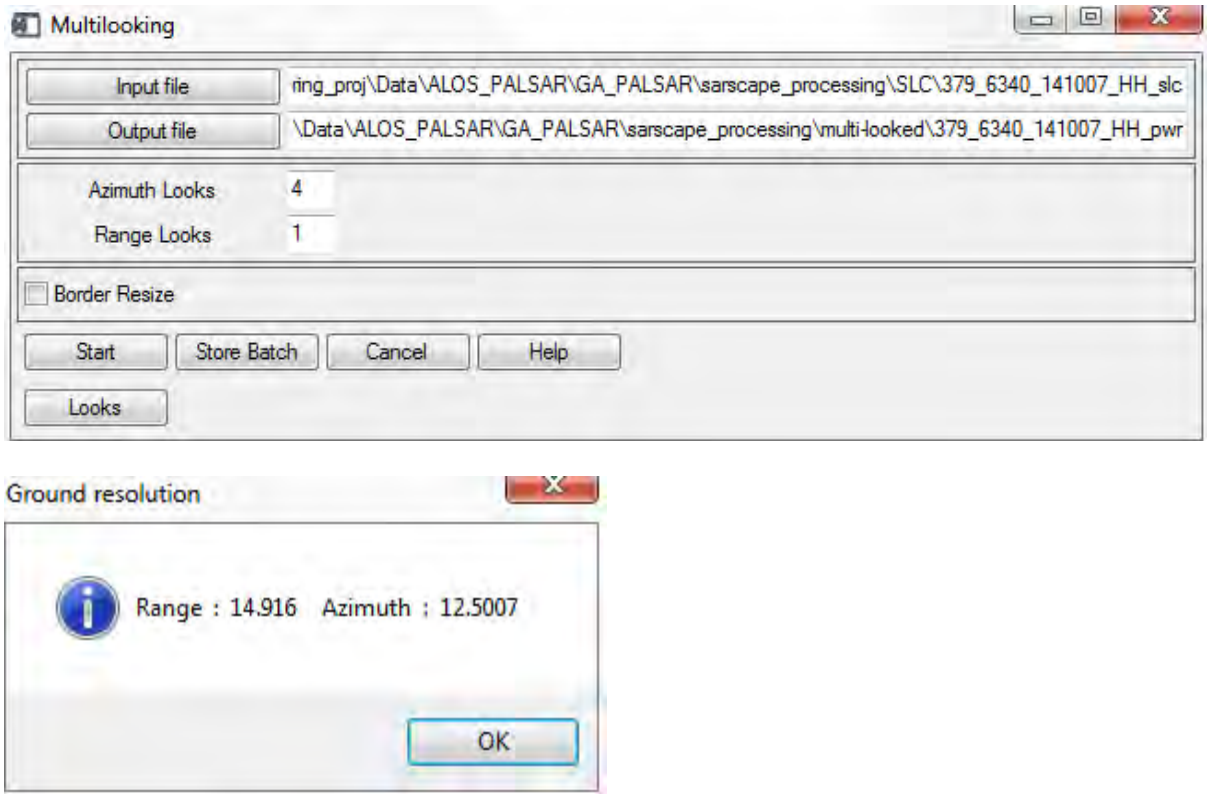

Figure 18. Multi-looking of ALOS PALSAR FBD data in SARscape. Data are multi-looked using 1 look in range and 4 looks in azimuth to achieve a pixel size approximating 12.5 m, which is the intended spatial resolution of the final geocoded product.

ALOS PALSAR FBD data processed using a range of multi-looking factors are illustrated in Figure 19. The output geocoded cell size was set to 12.5 m. The original SLC (1-look) data, with a pixel size of 14.9 x 3.1 m, is shown in (a). Maintaining 1 look in range, the number of azimuth looks was increased to 3 (b), 4 (c) and 7 (d), with output pixel sizes of 14.9 x 9.4 m, 14.9 x 12.5 m, and 14.9 x 21.9 m respectively. Data appears quite compressed when using a low number of looks (e.g., 3 looks in azimuth; (b)). The topography appears better preserved using a higher number of looks (e.g., 7 looks in azimuth; (d)), but the resulting image has odd pixel sizes. Multi-looking using 4 looks in azimuth presents a compromise between radiometric quality (and hence feature preservation) and best spatial resolution.

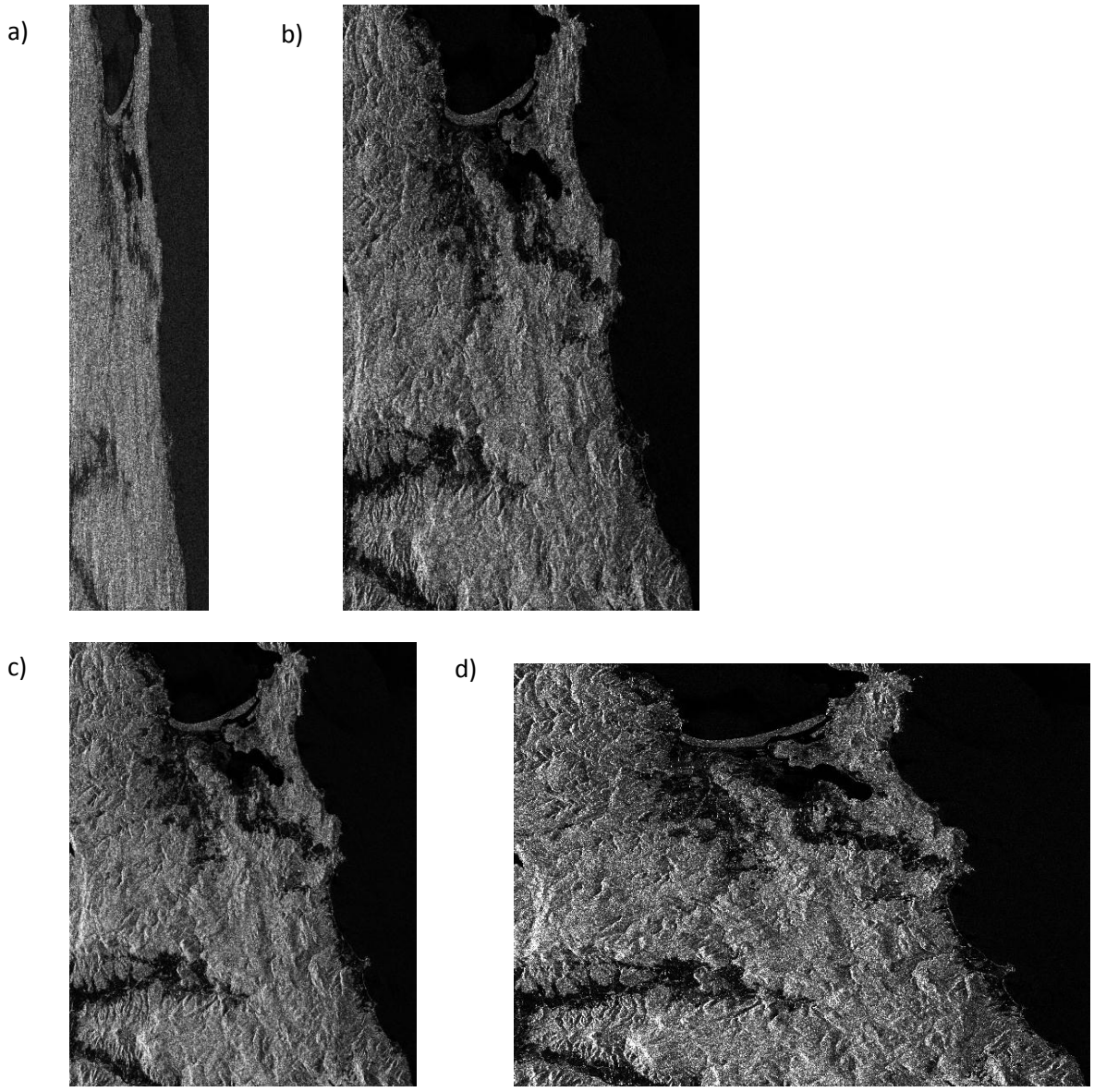

Figure 19. Examples of multi-looked ALOS PALSAR intensity data processed using different range and azimuth factors: a) Single Look Complex (1-look) data as reference; b) Data processed using 3 looks in azimuth and 1 in range; c) Data processed using 4 looks in azimuth and 1 in range; and d) Data processed using 7 looks in azimuth and 1 in range. The output pixels sizes are 14.9 x 3.1 m in (a), 14.9 x 9.4 m in (b), 14.9 x 12.5 m in (c), and 14.9 x 21.9 m in (d).

3.3 Co-registration of multi-date imagery

Co-registration is the process of superimposing multi-date, slant range images of the same area. Co-registered imagery is often a requirement to time-series filtering and processing of layer stacks. Best results are achieved using images with the same acquisition geometry, i.e., acquired at the same incidence angle, in the same swath and of like polarisation. The process is distinct from geocoding, where pixel location in slant range is converted to ground range and associated with a cartographic reference system. Sub-pixel co-registration accuracy is typically achieved, even without the use of a DEM. An input DEM is usually only required for co-registration of very high resolution data (better than 5 m) or in very steep terrain.

The co-registration process is an automated function within SARscape, and proceeds as follows:

i. Calculation of local non-parametric shift estimate using orbital data (and DEM if provided);
ii. Establish cross-correlation grid (set of windows) on reference image;
iii. Calculation of cross-correlation function for each window;
iv. Identify actual shift for selected location using maximum of cross-correlation function;
v. Co-register data through polynomial based calculation of residual parametric shift.

Multi-date (2007 – 2009) ALOS PALSAR FBD data acquired over an area in NE Tasmania is used as an example. Following multi-looking using 4 looks in azimuth and 1 look in range, slight differences in output pixel size are observed:
2007 HH and HV: 14.907933 x 12.526016 m
2008 HH and HV: 14.909544 x 12.527050 m
2009 HH and HV: 14.906967 x 12.526751 m

Resampling is required for images with different pixel sizes, so that data are precisely co-registered for further analysis. The earliest acquired scene (2007 HH polarisation) was used as the reference file, with subsequent images from 2008 and 2009 as input (Figure 20). Either the HH or HV polarisation image could have been used as the reference file. Given the moderate (12.5 m) spatial resolution of the images, a DEM was not required for co-registration. The option for 'Always compute shift' is selected as the input images are not already co-registered. Co-registration shifts between the reference and input images are calculated and stored in the shift parameter file if the 'Compute Shift Parameters' option is selected. Given the slight variation in pixel size amongst the input images, resampling was required, and in this case, 4^{th} order cubic convolution was selected.

Following co-registration, the multi-date images overlay exactly, as shown in the RGB colour composite of 2007HV:2008HV:2009HV images (Figure 21). Co-registered images all have the same pixel size and total dimensions.

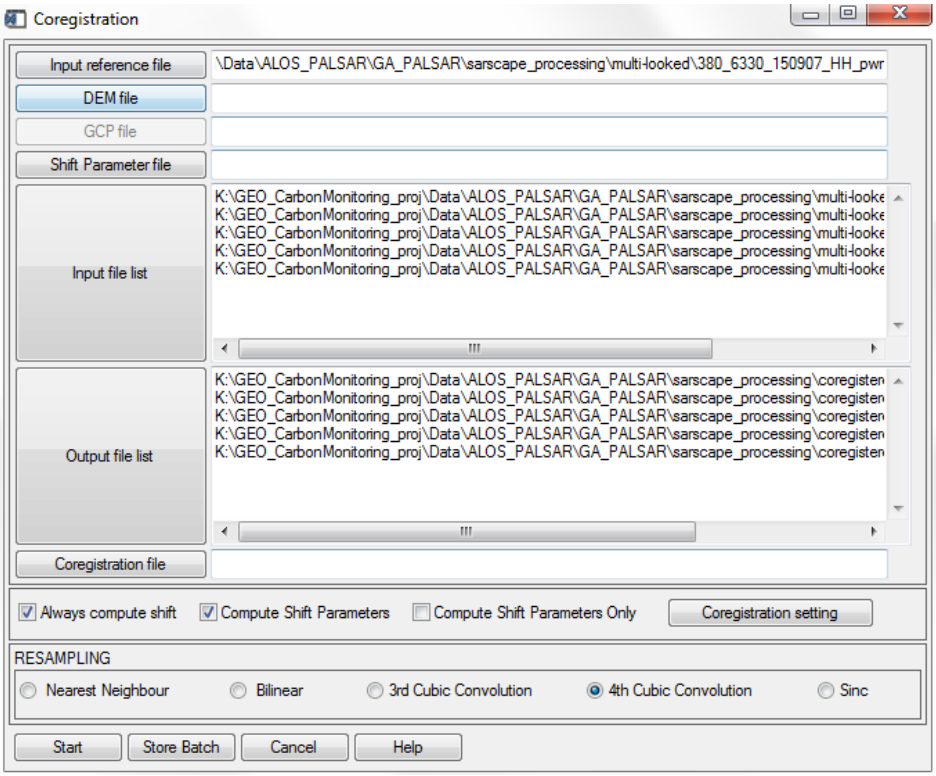

Figure 20. Co-registration of multi-date ALOS PALSAR FBD data through the SARscape Co-registration menu.

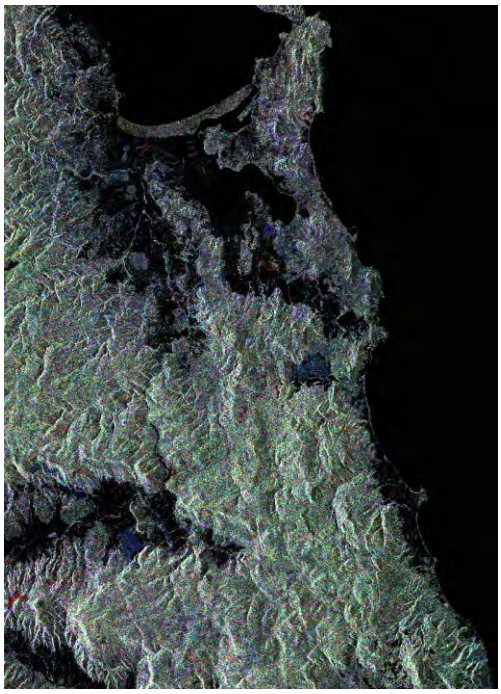

Figure 21. Successful co-registration of multi-date ALOS PALSAR images over NE Tasmania. Data from 3 different dates have been multi-looked and co-registered using SARscape. The colour composite has been generated by assigning 2007 HV, 2008 HV, and 2009 HV in Red (R), Green (G) and Blue (B) channels respectively.

Occasionally, the co-registration process can fail when multi-date images have highly variable areal extent or a greater proportion of non-land surface (i.e., more ocean/water; Figure 22a). In the first case, the image with the least spatial extent should be used as the reference image, otherwise co-registration windows will be located in dummy (no data) areas. In the second case, the default number of cross-correlation windows for extracting relevant parameters might not be sufficient over the land area. The situation can be countered by increasing the number and size of windows in azimuth and range directions in the SARscape default settings, or by manually identifying and creating a Ground Control Points (GCPs) file for use in co-registration. Both options increase the opportunities of finding land based features in the cross-correlation windows. The user can manually identify points across the land area (Figure 22b) and create a GCP file for use in the co-registration process. Points can be added as vectors in ENVI, from which a ground control point file (.xml) is generated using SARscape tools. Co-registration is then run using the .xml file as the co-registration file.

a)

b)

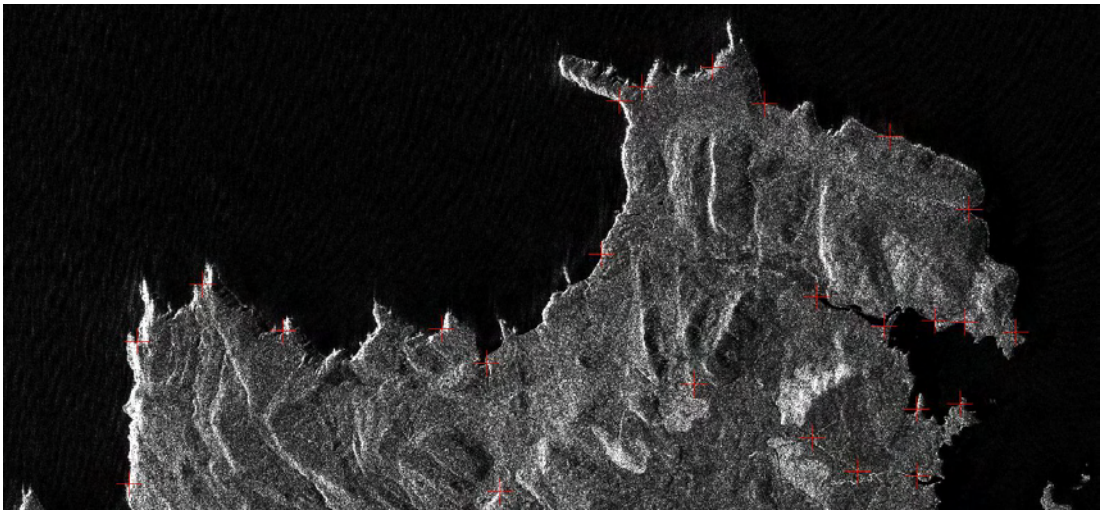

Figure 22. Instance of failure of the co-registration process: a) 2007 HH image with limited land cover over which to establish the cross correlation grid and compute shift parameters; and b) Manual identification of ground control points over the reference image to improve the co-registration.

4. SPECKLE FILTERING

In this section, the necessity of speckle filtering is discussed and the various filter options including single-date, multi-temporal and Gamma and Gaussian are described in detail.

4.1 Image speckle and filtering

SAR imagery is corrupted by speckle noise as a result of differential surface interactions. Speckle appears as the characteristic but random array of pixels with variable brightness. The brightness of a pixel is attributed to the coherent summation of constructive and destructive interferences on the incident radar wave. Image speckle is distinct from system noise, but its reduction is fundamental to SAR image analysis and interpretation.

There are two basic strategies to reducing speckle: multi-looking and adaptive filtering. Multi-looking is part of the image formation process, while adaptive filtering occurs post-image formation (Zhang *et al*., 2002). When multi-looking data, the greater the number of looks used, the greater the speckle reduction, but this comes at the expense of spatial resolution. Adaptive methods, based on multiplicative (e.g., Lee and Frost) or Gamma and Gaussian-distributed models (e.g., Gamma-Gaussian MAP) use local statistics to filter the data. Filtering should be application driven to achieve the desired outcome, e.g., reduced speckle or edge enhancement, and avoid undesirable outcomes, e.g., a reduction in dynamic range leading to loss of image detail. Post-processing steps such as segmentation are also effective in further reducing image speckle.

SARscape comprises a basic filtering module with single-date and multi-temporal filter options, and a separate Gamma and Gaussian filtering module. Additional non-SAR specific filters, such as mean and median are also included in the basic filter module. SAR-specific speckle filters within SARscape include:

i. Minimum Mean Square Error (multiplicative model)
   - Lee
   - Frost
   - Kuan

ii. Gamma and Gaussian MAP
   - Single channel detected
   - Multi-channel detected
   - Complex data

iii. Annealed Correlated MAP

iv. Multi-temporal
   - De Grandi
   - Anisotropic Non-Linear Diffusion (ANLD)

v. Polarimetric
    - Wishart Gamma MAP
    - Wishart De MAP

Using examples from ALOS PALSAR FBD data acquired over Tasmania, the application of select filters is demonstrated below.

4.2 Single-date filters

SARscape includes the following SAR-specific single-date filters in its basic filtering module: Frost, Lee, Refined Lee and Anisotropic Non-Linear Diffusion (ANLD). They are based on a multiplicative speckle noise model, and are adaptive in using local statistics to filter intensity data. Some filters allow a lower and upper limit to be set for better smoothing and preservation of texture or point targets respectively (Exelis VIS, 2010).

The Lee filter is widely used because of its simplicity, computational efficiency and general reliability of the results (Lee *et al*., 2009). It is not without shortcomings however, including the lack of preservation of the mean value, smoothing of point targets and limited impact on dark spotty pixels (Lee *et al*., 2009). Application of the Lee filter to multi-looked HH ALOS PALSAR intensity data over NE Tasmania using SARscape is shown in Figures 23 – 26.

The Lee filter is selected by navigating through the main SARscape menu > Basic > Filtering > Single image. Input and output filenames are first entered, followed by selection of the Lee filter (Figure 23a). A second menu opens (Figure 23b) where the required filter parameters are entered, including the azimuth and range window sizes and Equivalent Number of Looks (ENL).

a)

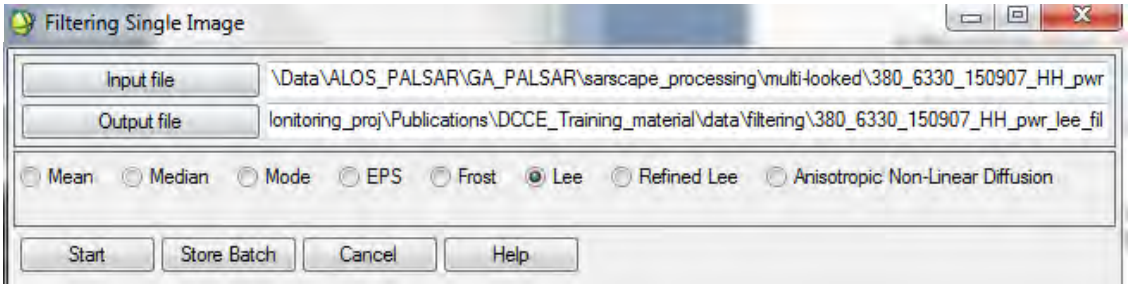

b)

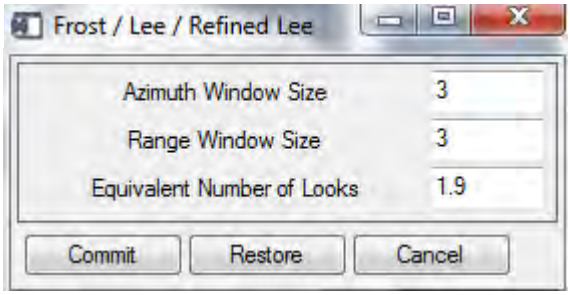

Figure 23. Single image filtering in SARscape: a) The basic single image filter menu; and b) Lee filter parameters menu. In the example, Lee filtering is applied to multi-looked HH ALOS PALSAR intensity data using a 3x3 window and ENL of 1.9.

In the example above, filtering is applied to multi-looked data where the size of azimuth and range pixels is roughly the same (14.9 X 12.5 m), and so a square 3x3 filter window is used. Using a larger

window size tends to have a greater smoothing effect, and this is demonstrated using a 3x3 window, 5x5 window and 7x7 window in Figure 24. The Lee filtered results all exhibit an unusual scattering of very bright pixels throughout the images.

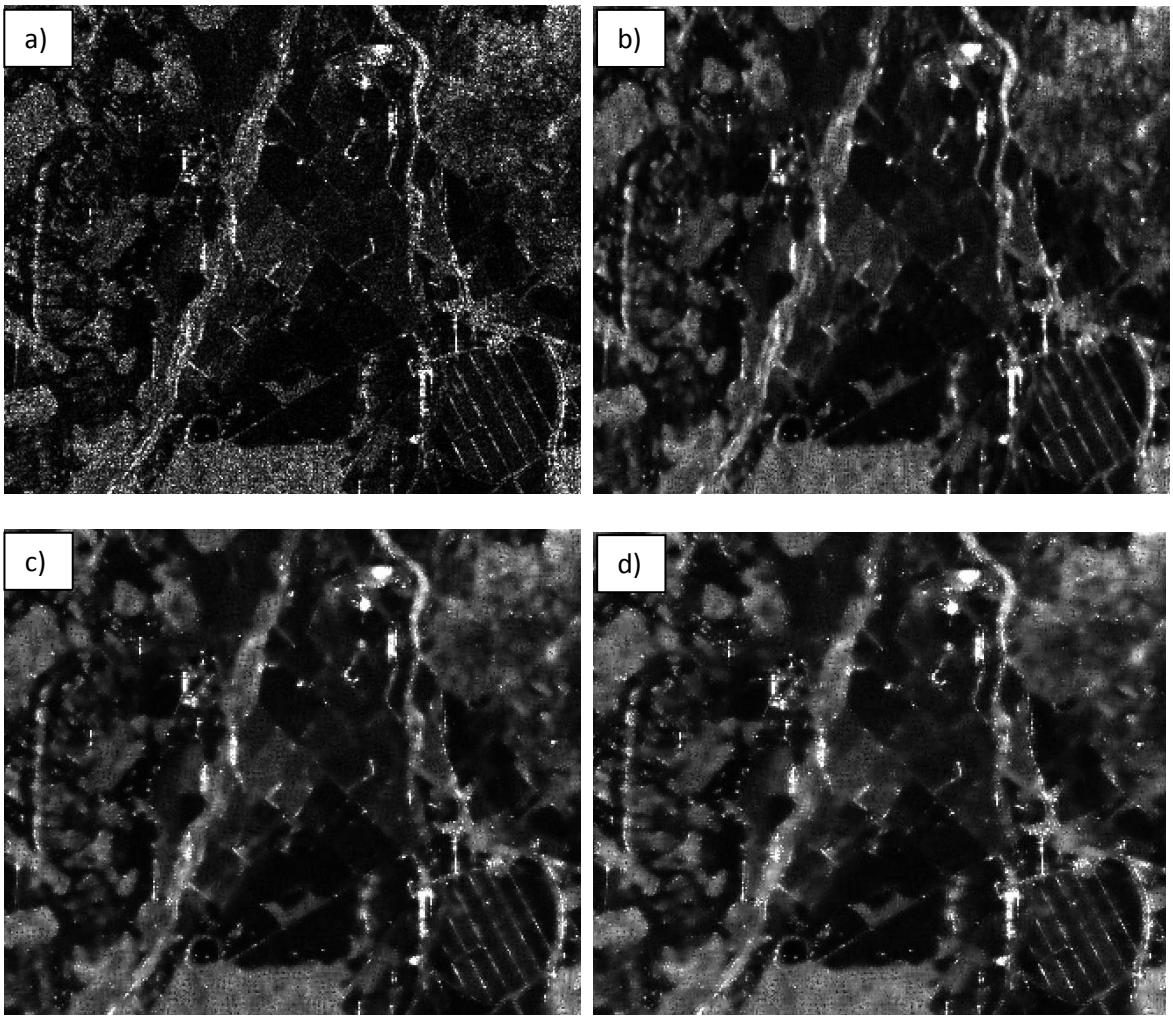

Figure 24. The impact of changing filter window size: a) Multi-looked HH ALOS PALSAR intensity data, and SARscape Lee filter results using a window size of b) 3x3; c) 5x5; and d) 7x7. The ENL is set to 1.9 in all cases.

The ENL is the number of independent intensity values averaged per pixel in the multi-looking process. It is calculated from statistics retrieved from a homogeneous area using the following equation:

$$ENL = mean^2 / standard\ deviation^2$$

To calculate the ENL, Regions of Interest (ROIs) can be established in homogeneous areas, including for example, areas of even forest cover or bare paddocks. Using ENVI quick stats, the mean and standard deviation of the polygon ROIs can be extracted, from which the ENL is calculated. In the example, polygon ROIs were established in dry eucalypt forest and bare paddocks. The ENL averaged 2.3 for forest areas and 1.4 for paddocks. The impact of changing the ENL parameter is demonstrated using minimum (0.9), mean (1.9) and maximum (2.5) ENL values and a fixed window

size (3x3) in Figure 25. A trade-off is evident between resulting image quality and preservation of image detail and sharpness while suppressing unwanted noise.

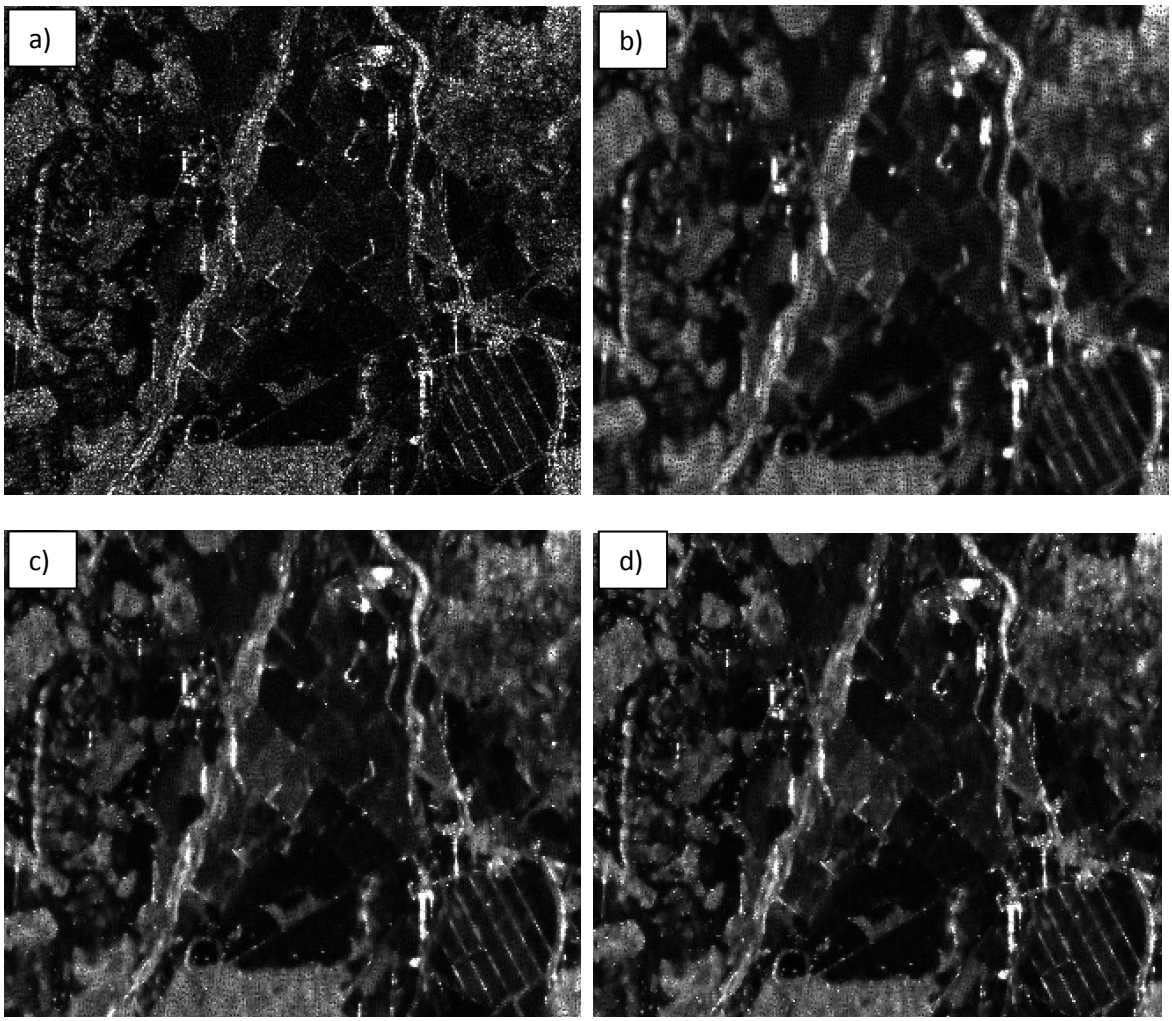

Figure 25. The impact of increasing the Equivalent Number of Looks (ENL) parameter: a) Multi-looked HH ALOS PALSAR intensity data, and Lee filter results using a 3x3 window and ENL of b) 0.9; c) 1.9; and d) 2.5. Compared to (c) which uses the mean ENL, image quality in (b) is quite poor with a high degree of smoothing and pitting in the data. Bright scattered pixels are most evident in (d).

The effectiveness of filtering can be assessed both visually and by computing statistics for the scene or ROIs for specific cover types. The coefficient of variation (CV) is calculated using the ratio of standard deviation to mean (s.d/mean), and provides a good indicator of heterogeneity in the scene, or the extent of variability in relation to the image mean. Ideally you want to preserve the mean value and reduce the s.d (Table 5). Frequency histograms can be generated showing the change in distribution of image values for a ROI or scene (Figure 26).

Table 5. Comparison of Coefficient of Variation (CV) calculated for unfiltered and Lee filtered ROIs.

ROI	Multi-looked data			Filtered data		
	Mean	SD	CV	Mean	SD	CV
Forest1	48517456687.64	33614922012.42	0.693	48349541557.42	14289815544.95	0.296
Forest2	42580320124.17	27005115713.73	0.634	42304425024.06	13221360284.88	0.313
Forest3	47257370787.80	31498733618.32	0.667	47200019434.45	14869493503.51	0.315
Ag1	3921983924.76	3967598265.46	1.012	3901536690.58	2391521842.02	0.613
Ag2	3766752714.54	2792735745.82	0.741	3762935426.54	1360515038.59	0.362
Ag3	6540640264.15	5340545700.05	0.817	6482383647.68	3330614562.96	0.514
Full scene	21989230447.74	46617496587.55	2.12	21859421533.30	37952209945.43	1.74

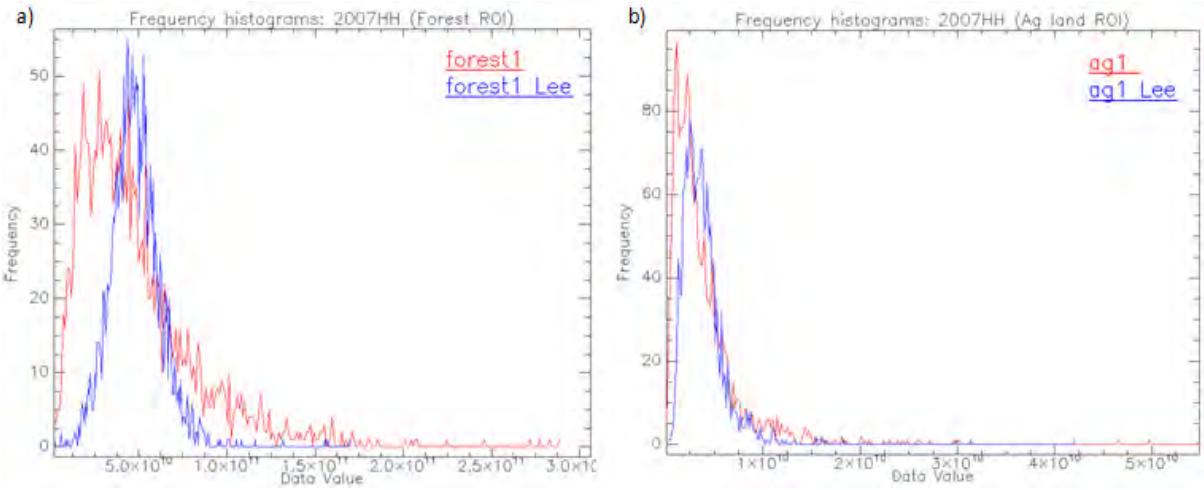

Figure 26. Frequency histograms for ROIs identified on multi-looked (unfiltered; in red) and Lee filtered data (3x3 window, ENL=1.9; in blue): a) ROI extracted in forested terrain; and b) ROI extracted over agricultural land.

It should be noted that the results of Lee filtering using the SARscape basic filter module and ENVI's adaptive filtering module are not consistent. Figure 27 illustrates the results of applying both Lee filters on multi-looked HH intensity ALOS PALSAR data. The ENVI result is clearly better, with less smoothing and enhancement of point targets in the filtered result.

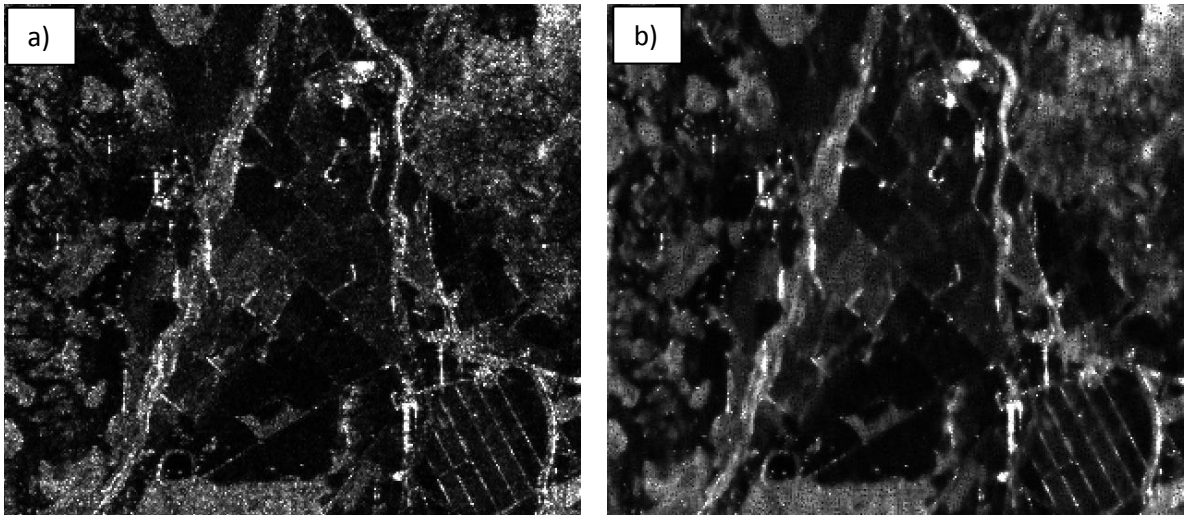

Figure 27. Comparison of Lee filtering in a) ENVI and b) SARscape, on multi-looked HH ALOS PALSAR intensity data. The results are inconsistent, with a greater degree of smoothing and enhancement of point targets following application of the SARscape Lee filter.

4.3 Multi-temporal filters

Multi-temporal filters exploit the space-varying temporal correlation of speckle between a co-registered time-series of SAR images. There are 2 multi-temporal filters available in ENVI SARscape, including De Grandi and Anisotropic Non-Linear Diffusion (ANLD). The De Grandi filter is an optimum weighting filter that balances differences in reflectivity between images of a time-series (ITT VIS, 2010). Proper co-registration of images is essential as the filter assumes that each pixel in the time-series is similarly illuminated, i.e., has similar viewing geometry, and referenced to the same map coordinates (Sarmap, 2009). The multi-temporal ANLD filter uses time-series statistics but is completely independent of the data source and acquisition geometry (ITT VIS, 2010).

In Figure 28, the multi-temporal De Grandi filter is applied to time-series multi-looked HH ALOS PALSAR intensity data in NE Tasmania. The filter is selected by navigating through the main ENVI SARscape menu > Basic > Filtering > Multi-temporal (Figure 28a). Input and output filenames are first entered, followed by selection of the De Grandi filter. A second menu opens (Figure 28b) where the required value for ENL is entered. The ENL was estimated for several ROIs and values ranged between 2.1 - 3.3 and 0.8 - 2.4 for forest and paddock respectively in multi-date imagery. Using an average ENL value of 2.0, the results of filtering the time-series (2007 - 2009) is shown in Figure 29. The impact of changing the ENL is demonstrated in Figure 30. Bright scattered pixels are more evident in images filtered using a higher ENL. Multi-date filtered images have slightly smoother texture but good feature preservation. Frequency histograms for multi-looked and De Grandi filtered data and for ROIs extracted over forested terrain and agricultural land are show in Figure 31.

a)

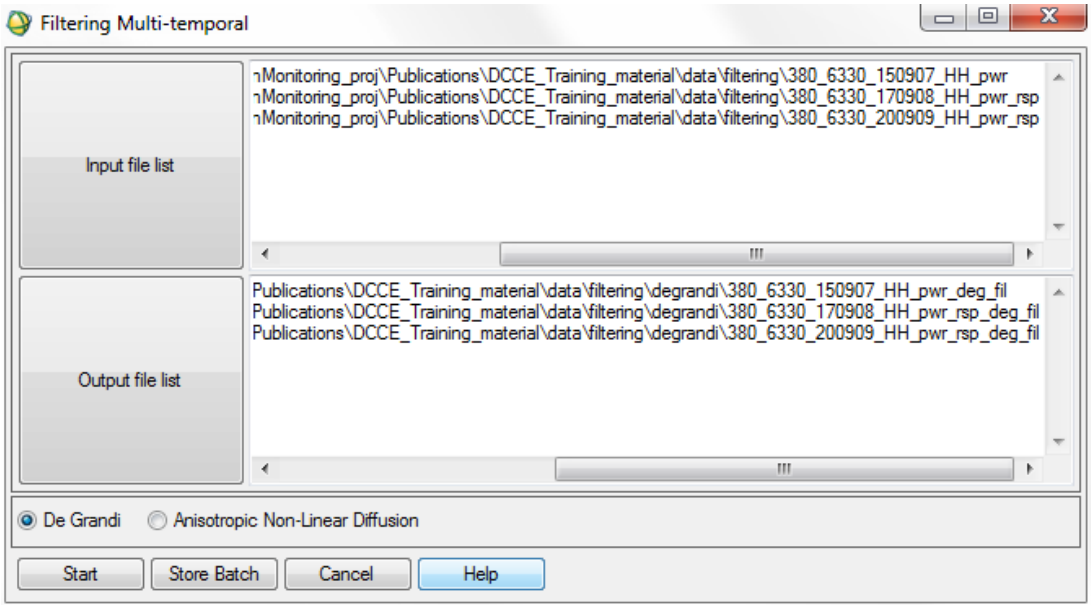

b)

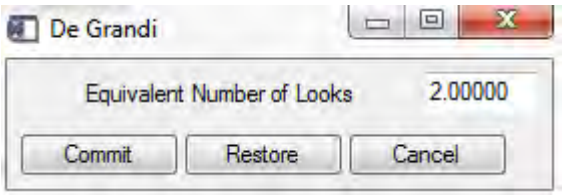

Figure 28. Multi-temporal filtering in SARscape: a) The basic multi-temporal filter menu; and b) De Grandi filter parameters menu. In the example, the De Grandi filter is applied to a time-series of multi-looked HH ALOS PALSAR data using an ENL value of 2.0.

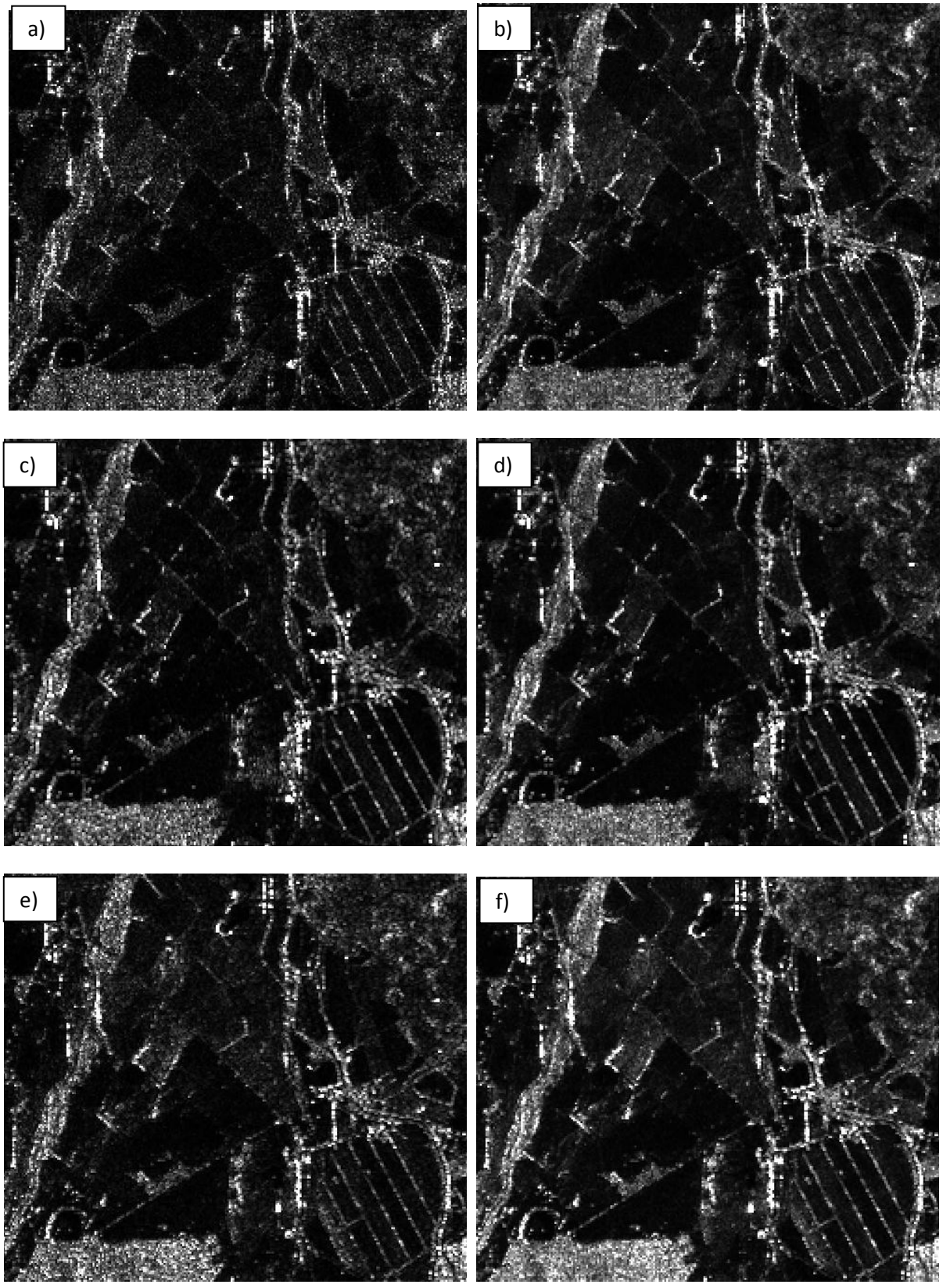

Figure 29. Multi-temporal De Grandi filtering applied to ALOS PALSAR multi-looked (ML) data in SARscape: a) ML 2007 HH; b) De Grandi filtered 2007 HH; c) ML 2008 HH; d) De Grandi filtered 2008 HH; e) ML 2009 HH; and f) De Grandi filtered 2009 HH. An ENL of 2.0 was applied in all cases.

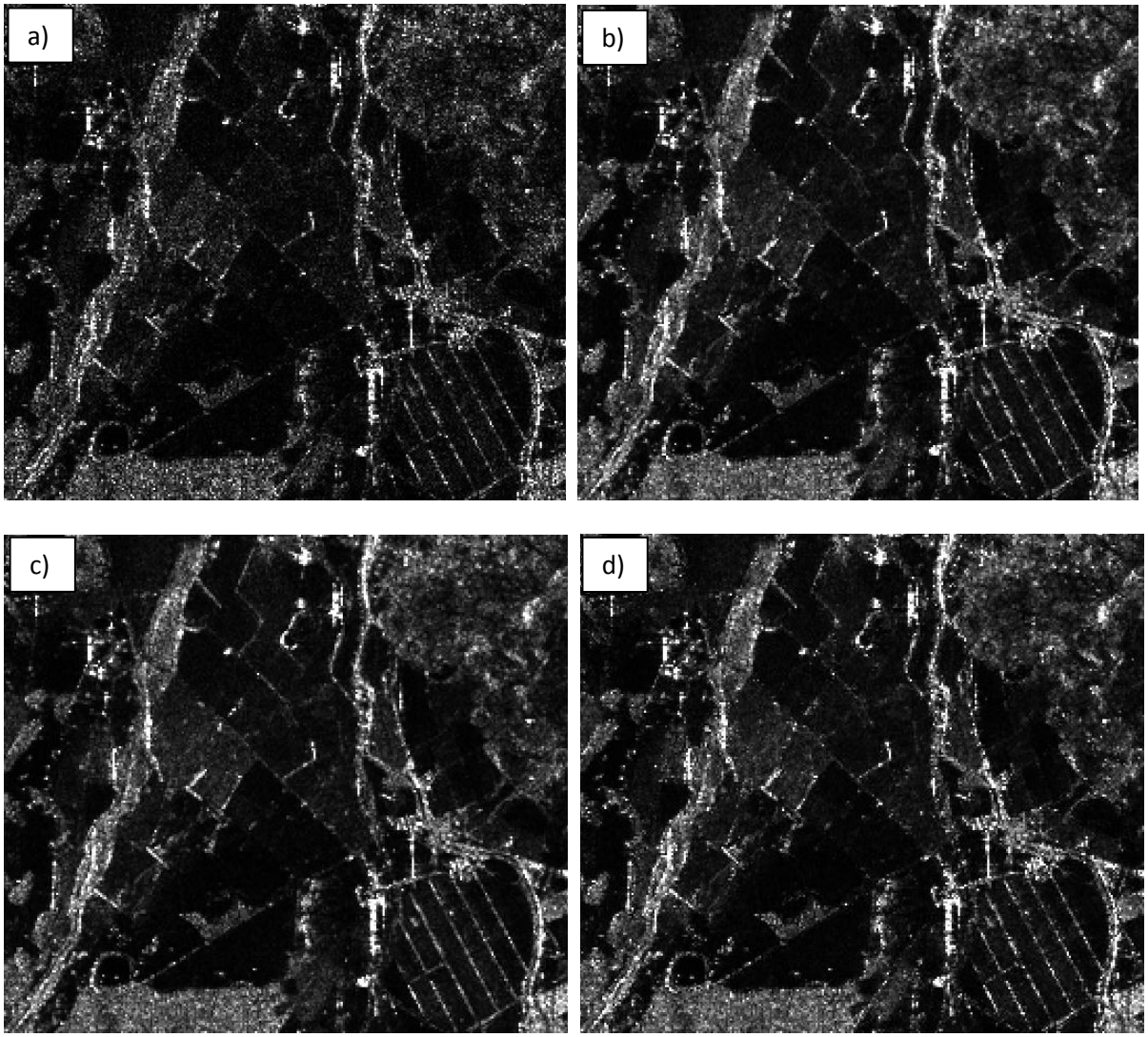

Figure 30. The impact of increasing the Equivalent Number of Looks (ENL) parameter: a) Multi-looked HH ALOS PALSAR intensity data for 2007, and De Grandi filter results using an ENL of b) 0.8; b) 2.0; and d) 3.3.

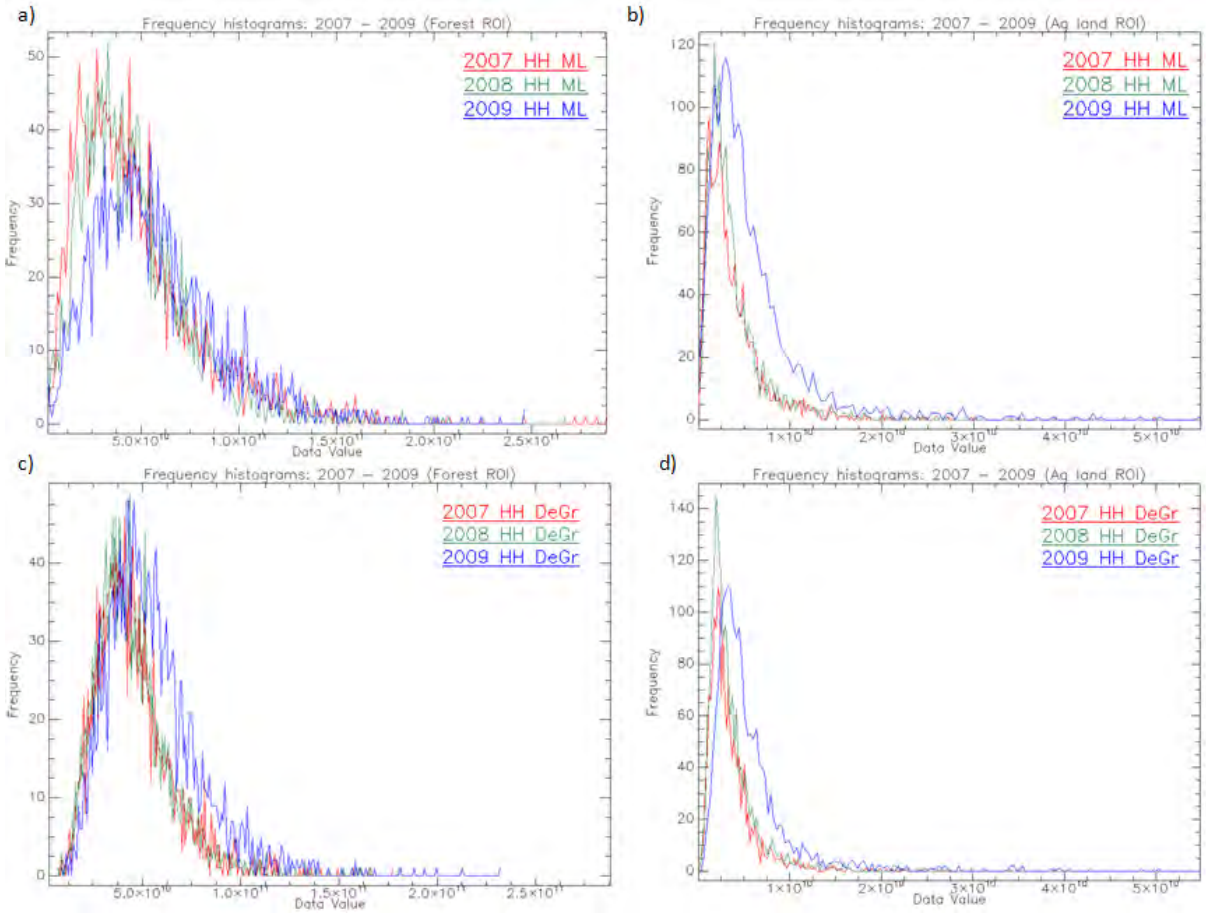

Figure 31. Frequency histograms for ROIs identified on multi-looked (unfiltered) and De Grandi filtered data (ENL=2.0): ROI extracted in forested terrain in ML data; b) ROI extracted over agricultural land in ML data; c) De Grandi filtered multi-date HH data for forested ROI; and d) De Grandi filtered multi-date HH data for agricultural land ROI.

The effect of multi-temporal filtering on time-series ALOS PALSAR data is illustrated in Figure 32. A spatial profile has been extracted across multi-date ML and filtered data, extending through a patch of forest and agricultural land. The 2007 ML data exhibit higher overall intensity values compared to images acquired in 2008 and 2009. This has been preserved in the filtered data. The data distribution is more varied in the multi-looked data, whereas similar trends are observed in the filtered data.

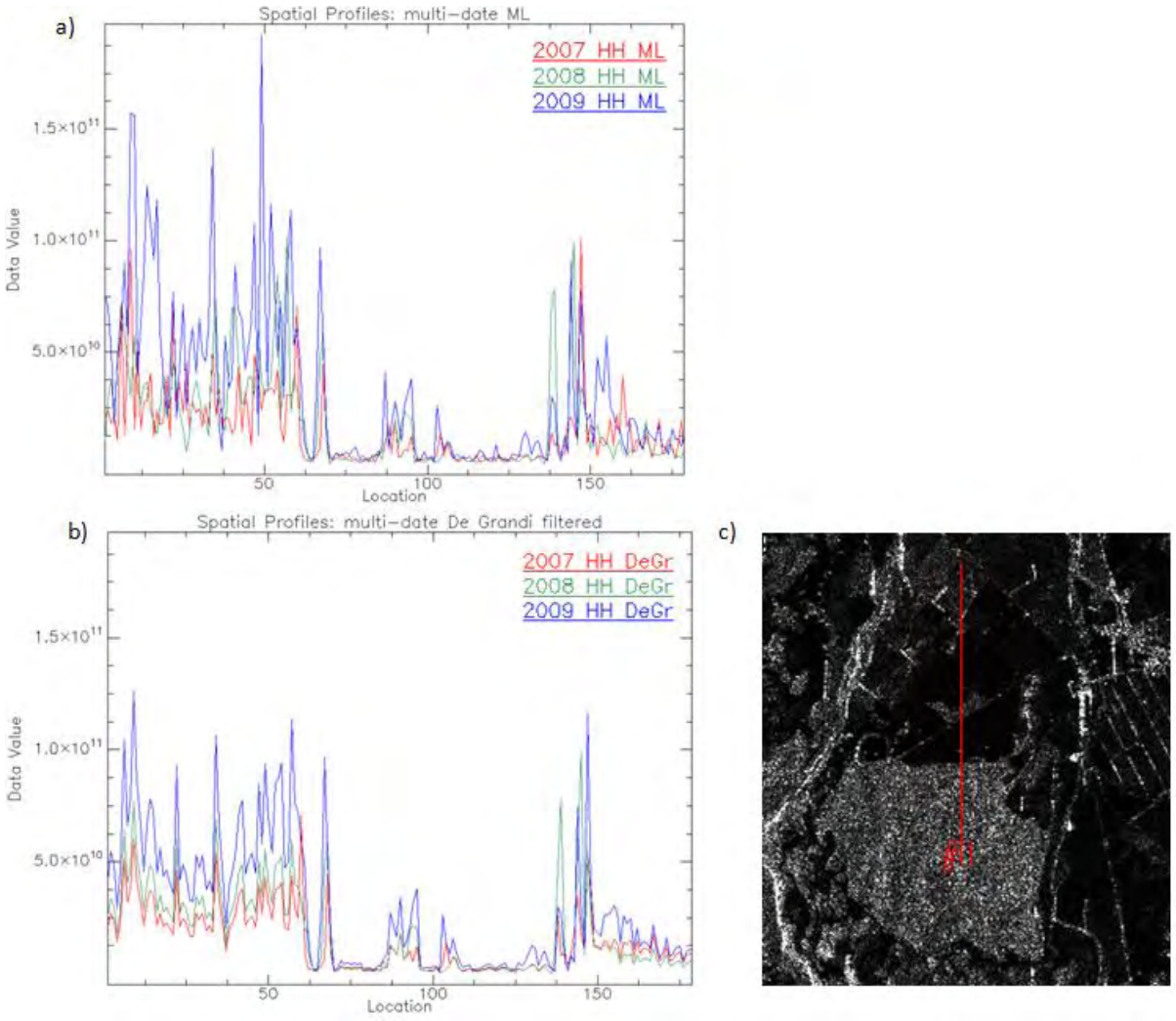

Figure 32. The effect of multi-temporal De Grandi filtering on multi-date ALOS PALSAR data. Spatial profiles extracted over a) multi-looked data; and b) Filtered data. The transect extends across forest and agricultural land (c).

4.4 Gamma and Gaussian filters

These filters are based on Gamma and Gaussian distributed scene models and effectively reduce speckle while preserving image texture and spatial resolution. In highly textured images, an *a priori* first order statistical model is required to preserve scene texture at the optimal spatial resolution (ITT VIS, 2010). The Gamma models are the most appropriate for SAR clutter, and when modified by an independent complex-Gaussian speckle model (for SLC data) or a Gamma speckle model (for multi-look data), result in K-distributed clutter. Gaussian models are also useful for multi-channel SAR data, with multivariate *a priori* scene distributions. Filtering of SLC data is preferable in, for example, urban areas with discrete bright scatterers; otherwise single channel detected filters can be used for scenes dominated by distributed scatters such as Gamma MAP (single-date) and Gamma DE MAP (multi-date; F. Holecz, Pers. Comm.).

There are 3 groups of Gamma and Gaussian filters available within ENVI SARscape:

i. Single channel detected
   - Gamma-Gamma Maximum A Posteriori (MAP)

- Gamma-Distribution-Entropy MAP (DE MAP)
- Gamma A Posteriori Mean

ii. Multi-channel detected
- Gamma-Gaussian MAP
- Gaussian-Gaussian MAP
- Gaussian-DE MAP

iii. Complex
- SLC Gaussian-DE MAP
- Complex Gaussian-Gamma MAP

In Figure 33, the Gamma MAP filter is applied to multi-looked HH ALOS PALSAR intensity data in NE Tasmania. The filter is selected by navigating through the main ENVI SARscape menu > Gamma and Gaussian filtering > Single channel detected > Gamma MAP. Input and output file names are specified, followed by selection of the Gamma MAP filter, and required parameters including ENL of 1.9 and window size of 3x3. Filtered results for 2007 HH data are illustrated in Figure 34.

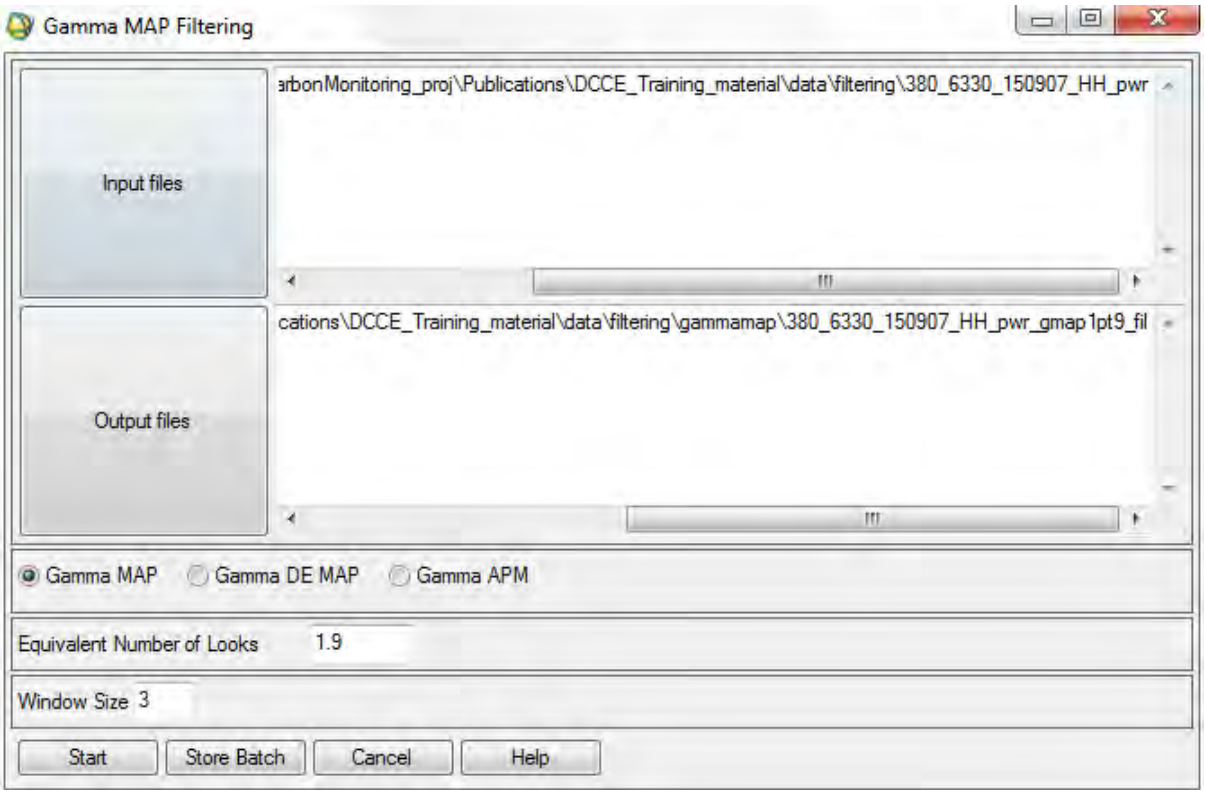

Figure 33. Single channel Gamma MAP filtering in SARscape: The basic filter menu with parameter selection: ENL = 1.9 and 3x3 window size.

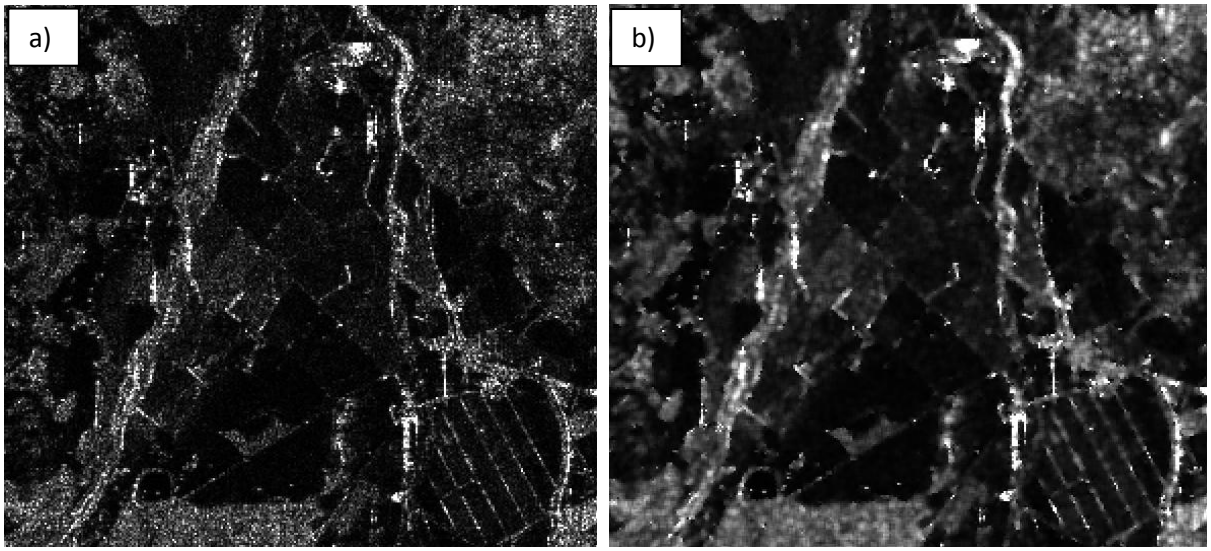

Figure 34. Single channel detected Gamma MAP filtering in SARscape. In the example, the Gamma MAP filter is applied to multi-looked HH ALOS PALSAR intensity data using an ENL of 1.9 and window size of 3. Multi-looked data shown in (a) and filtered data in (b).

The effect of changing the ENL value when applying the Gamma MAP filter is illustrated in Figure 35. ENL values of 0.9, 1.9 and 2.5 were used, with a common 3x3 window size. Scattered bright pixels are more evident in filtered images with higher ENL parameter. Some fence lines and edges appear thicker but smoothing is evident, particularly in forested areas in all filtered images.

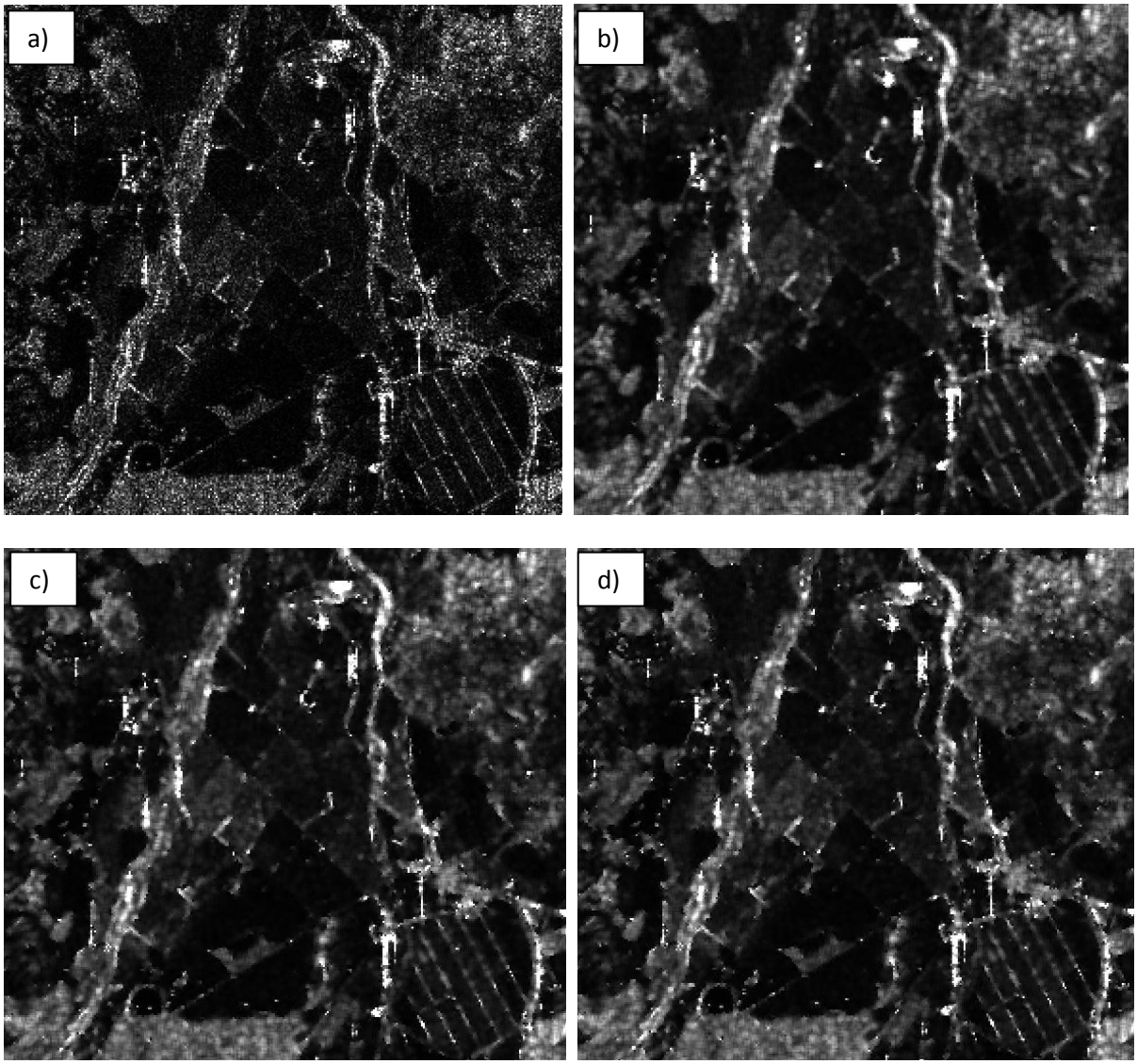

Figure 35. The impact of changing the ENL parameter when applying Gamma MAP filter in SARscape: a) Multi-looked 2007 HH intensity ALOS PALSAR data; and Gamma MAP filter results using an ENL value of b) 0.9; c) 1.9 and d) 2.5.

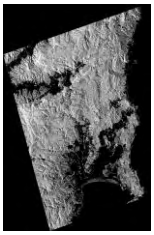

5. ORTHORECTIFICATION AND RADIOMETRIC CALIBRATION

This section describes the procedures for orthorectification of SAR data and radiometric calibration. The impact of DEM quality on the orthorectification process is discussed. Options for assessing the geographic accuracy of orthorectified products are outlined.

5.1 Orthorectification and radiometric calibration

5.1.1 Orthorectification

SAR sensors measure the power ratio (i.e., backscatter) between the transmitted and received pulse. This ratio is projected onto slant range geometry. Imaging geometry in SAR images is completely different in range (across-track) and azimuth (along-track) directions. This spatial distortion is most evident in the range direction, and largely the result of topographic variations (Sarmap, 2012). Distortion in the range direction is more easily corrected than the smaller, but more subtle distortions occurring in azimuth. Geometric and radiometric correction of data is necessary for inter-comparison of radar images acquired with different sensors, or the same sensor but in different acquisition modes, and for data focussed in different processors (Sarmap, 2012).

Orthorectification or geocoding is the process by which SAR data are converted from slant range to ground range geometry and in a defined cartographic (map coordinate) system. In SARscape, the process employs a rigorous Range-Doppler approach, with (terrain geocoding) or without use of a DEM (ellipsoidal geocoding; ITT VIS, 2010). The DEM or ellipsoid height provides the starting point for calculating the position of each backscatter element with respect to sensor position, velocity vectors and Doppler frequencies, into slant range image coordinates. If precise orbital information is provided, then accurate geocoding achieving sub-pixel accuracy can be performed using nominal sensor parameters without the need for GCPs.

SARscape facilitates the generation of Local Incidence Angle (LIA) and layover/shadow maps during orthorectification. LIA represents the angle between the normal to the backscattering element and incident radiation. In the resulting image, negative angles represent active layover areas, while angles > 90° represent active shadow areas. Those areas unaffected by layover or shadow assume LIA values of $0 \geq LIA \leq 90°$.

5.1.2 Radiometric calibration

Calibration of backscatter values is required prior to comparison of images acquired by different sensors, or using different observation modes, or at different times of year. SAR data are radiometrically calibrated using standard radar equations to correct for systematic errors and brightness variations due to terrain. Corrections are applied for the following:

i. Scattering area - real illuminated area of each pixel as a result of topography and incidence angle;
ii. Antenna gain pattern - variation in range direction of the ratio of the signal received or transmitted compared to an isotropic antenna; and

iii. Range spread loss - variation in backscatter with sensor-to-ground distance variation from near to far range.

Radiometric normalisation is then applied to correct for the effects of incidence angle on backscatter intensity. The variations in backscattering coefficient are most pronounced in the range direction. The variations can be compensated for using 2 methods:

i. Cosine correction - based on a modified cosine model (Ulaby and Dobson, 1989):

$$\sigma^\circ_{norm} = \sigma^\circ_{cal} (\cos \vartheta_{norm} / \cos \vartheta_{inc})^n$$

Where n is a weighting factor (ranging between 2 and 7) depending on image acquisition mode; ϑ_{norm} is the incidence angle at scene centre; and ϑ_{inc} is the LIA referencing the ellipsoid.

ii. Semi-empirical correction - backscatter dependency is estimated through linear regression of the cosine of LIA and the backscattering coefficient in logarithmic form.

Calibrated data are represented by a normalised dimensionless number. The corresponding value in decibels (dB) can be calculated by applying the following to intensity (I) data:

$$dB = 10*log_{10}(I)$$

In a final step, images are resampled to the desired output pixel size. If a DEM is used in the geocoding process, the image is automatically resampled using 4th order cubic convolution.

Orthorectification and radiometric calibration are applied in the same step in SARscape (Figure 36). In the example, multi-looked, Lee filtered ALOS PALSAR data (2007 HH) is the input for terrain geocoding using an available 25 m DEM. 4th order cubic convolution (CC) is used to resample to 12.5 m spatial resolution. Radiometric calibration and normalisation are applied using the LIA and a semi-empirical correction method.

The influence of the DEM on positional accuracy is illustrated in Figure 37. In the example, multi-looked, Lee filtered ALOS PALSAR 2007 HH data has been terrain geocoded using an available 25 m spatial resolution DEM and radiometrically calibrated and normalised (Figure 37a). The result is compared with similarly processed data but with ellipsoid geocoding applied (Figure 37b). The lack of DEM information leads to significant inaccuracies in the position of features compared to the terrain geocoded example (Figures 37c and d).

Additional products generated during orthorectification are illustrated in Figure 38. The input DEM is used in the calculation of Local Incidence Angle (LIA; Figure 38a) and layover/shadow (Figure 38b). Negative LIA represents layover areas (shown in red) and angles > 90° represent areas affected by shadow.

The impact of radiometric calibration and normalisation is illustrated in Figure 39. In the example, multi-looked, Lee filtered ALOS PALSAR HH data have been terrain geocoded and radiometrically calibrated in (a) and radiometrically calibrated and normalised in (b). Brightness variations across the near to far range are most evident in the calibrated data only. Once data are normalised, there is more homogeneous brightness across the image.

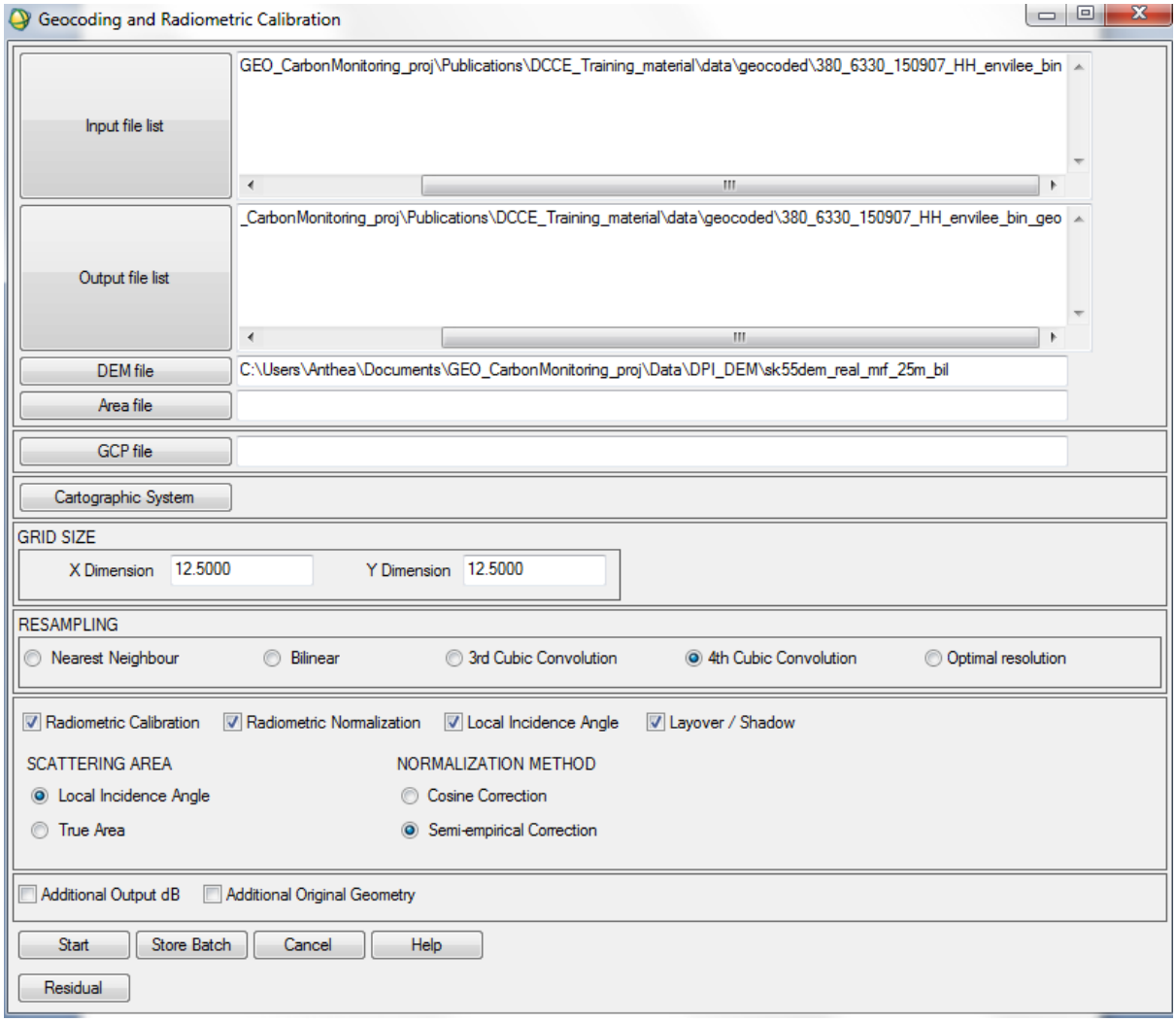

Figure 36. SARscape Geocoding and radiometric calibration menu. In the example, multi-looked, Lee filtered ALOS PALSAR data (2007 HH) is the input for terrain geocoding using an available 25 m DEM. 4th order cubic convolution is used to resample to 12.5 m spatial resolution. Radiometric calibration and normalisation are applied using the LIA and a semi-empirical correction method.

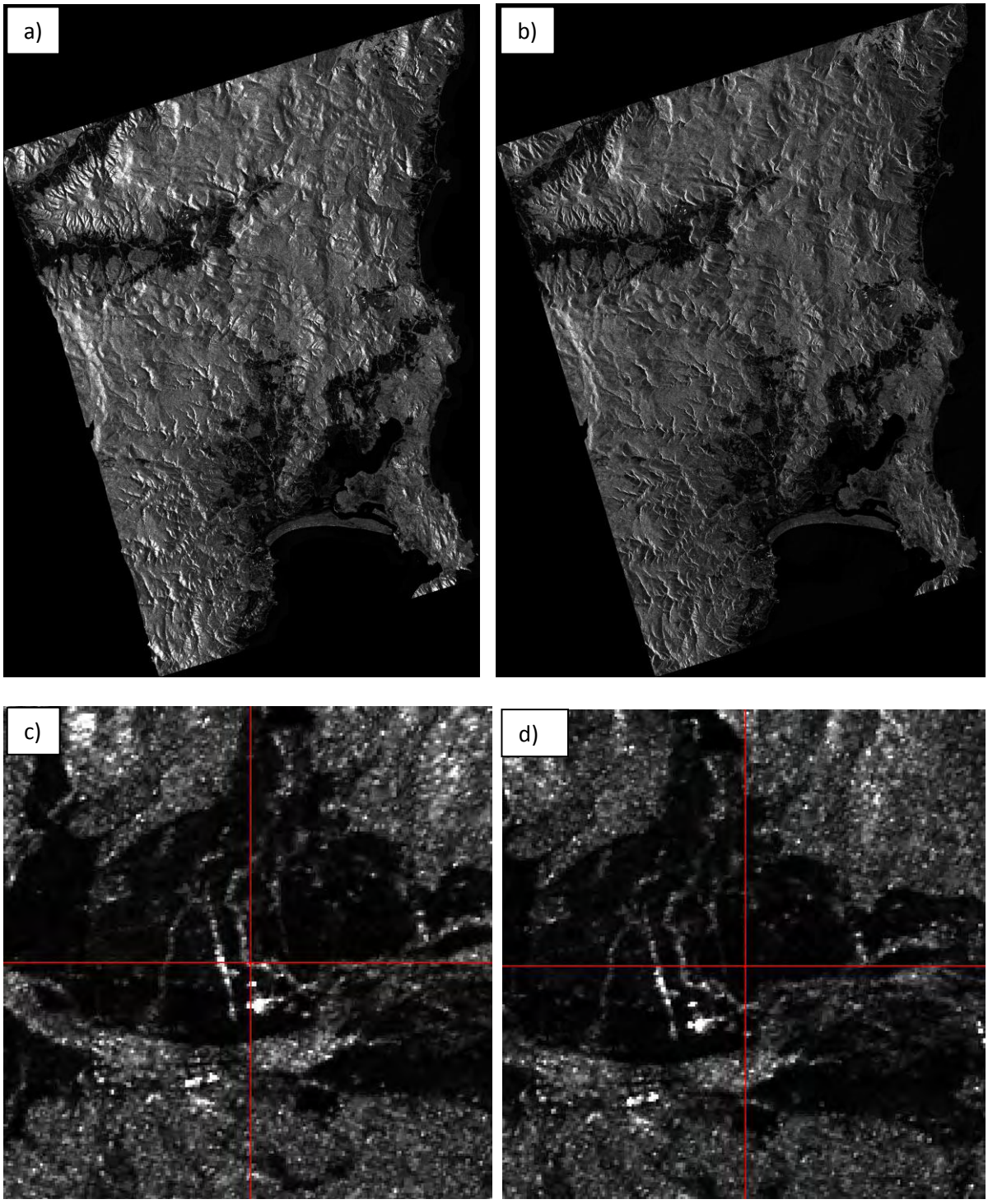

Figure 37. Orthorectification of ALOS PALSAR data: a) Terrain geocoded HH data; and b) Ellipsoid geocoded HH data. Both images have been projected onto the UTM zone 55 South WGS-84 system. Zoomed subsets comparing location accuracy in c) Terrain geocoded image; and d) Ellipsoid geocoded image.

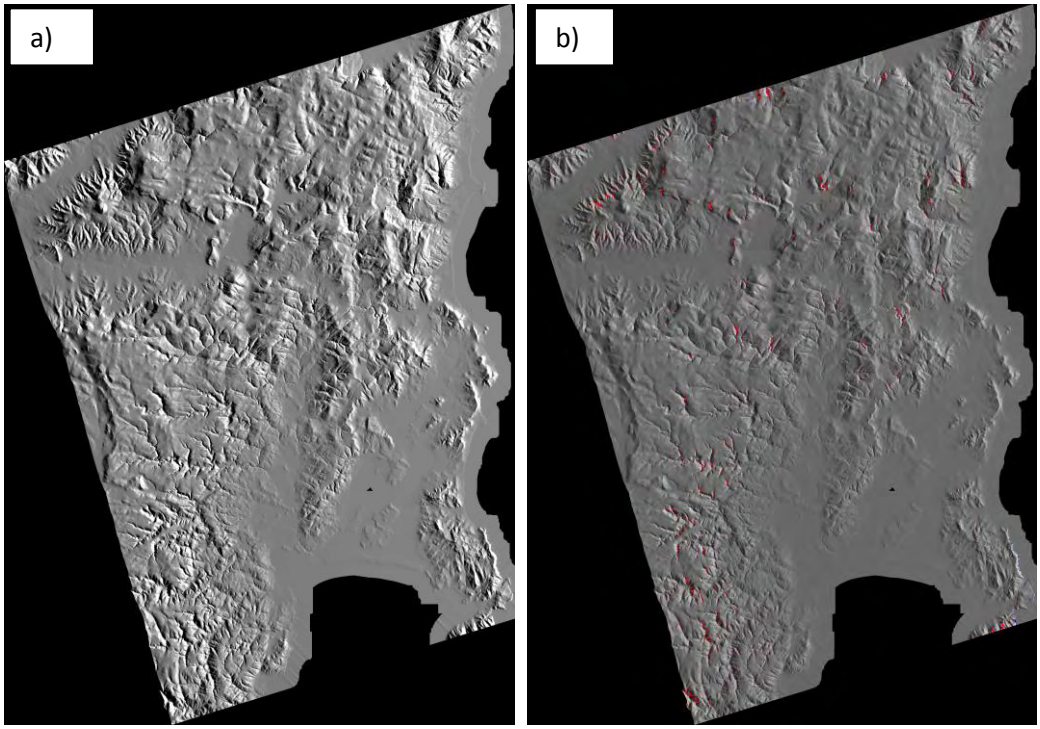

Figure 38. Additional image products generated during orthorectification: a) Local Incidence Angle (LIA); and b) Layover/shadow mask (layover areas in red, shadow areas in blue).

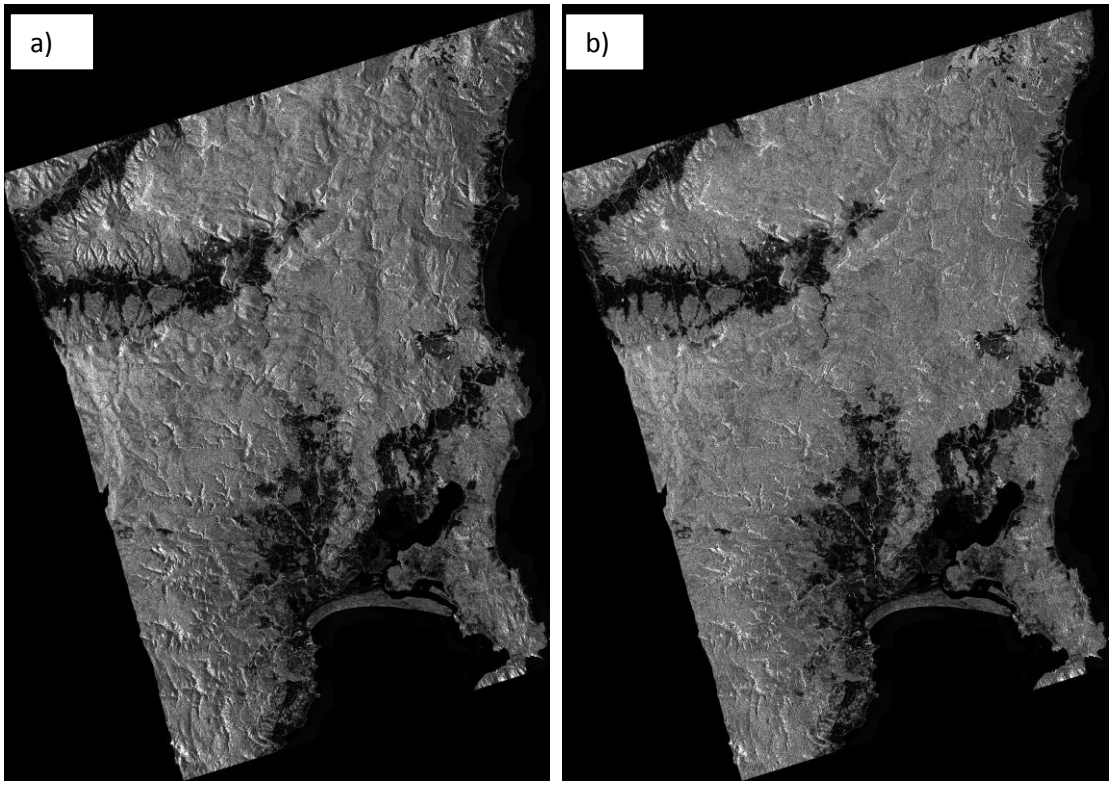

Figure 39. Impact of radiometric calibration and normalisation on the backscattering coefficient: a) Multi-looked, Lee filtered, terrain geocoded and radiometrically calibrated HH data; and b) Similarly processed but radiometrically calibrated and normalised HH data. Brightness variations from near to far range are most evident in the radiometrically calibrated data only. Following normalisation, brightness is more homogeneous across the image.

5.2 Influence of DEM quality on orthorectification

The quality of the DEM is important during orthorectification, particularly in relation to the location of features, stretching effects and generation of local incidence angle information, but also for radiometric calibration. Three DEMs were trialled to investigate the influence of DEM quality on orthorectification of ALOS PALSAR FBD data, including DEMs sourced from ASTER, SRTM (3 arc-sec, v2), and a photo-interpreted DEM available through DPIPWE (Figure 40). In each case, orthorectification was applied using each DEM in turn, resampled to 12.5 m pixels using 4th order cubic convolution, and radiometrically calibrated and normalised.

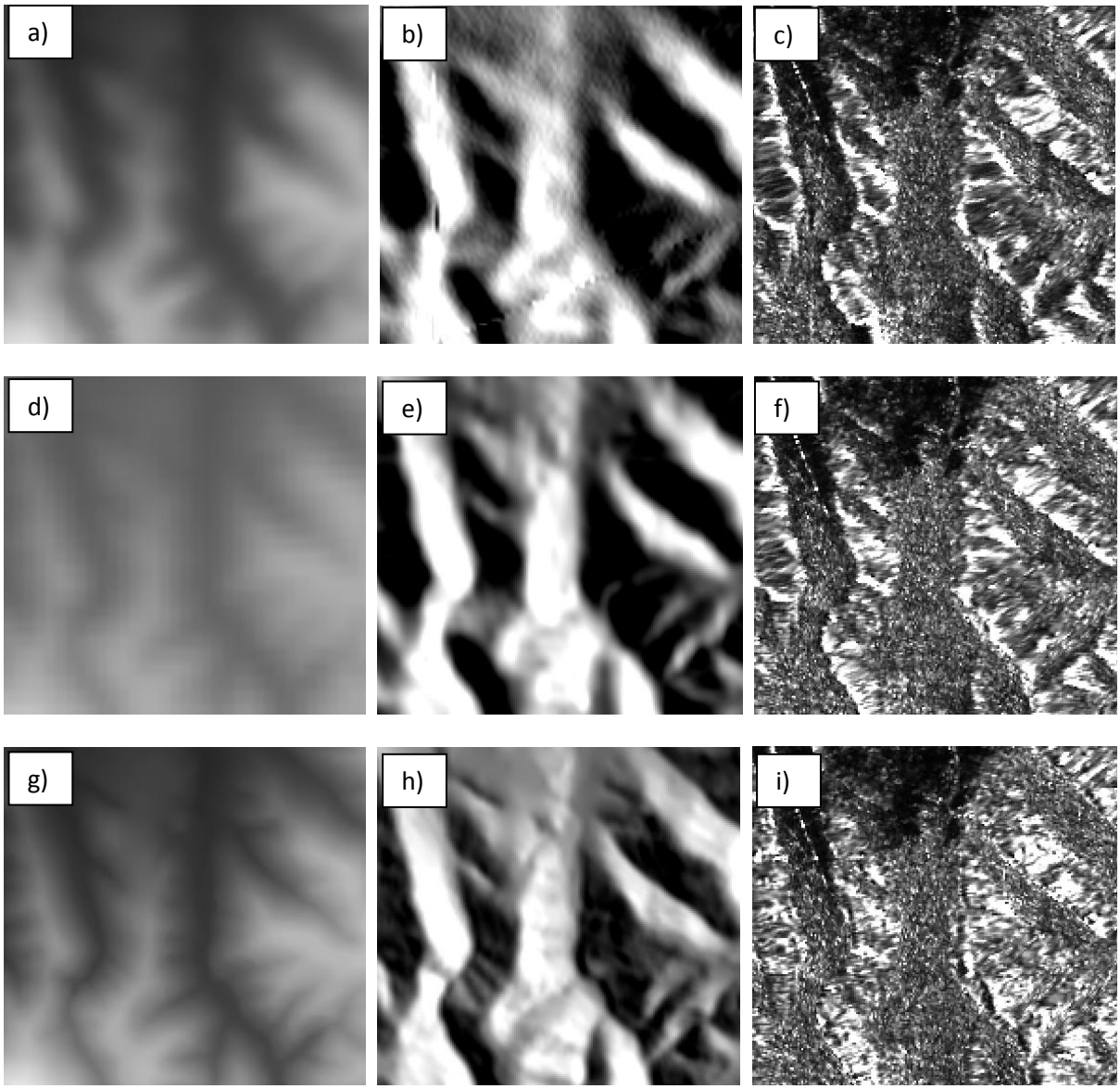

Figure 40. Illustration of DEM quality on orthorectified product. Each row illustrates the result of orthorectification using a specific DEM. Top row: a) ASTER DEM; b) LIA; c) Orthorectified HH. Middle row: d) SRTM 3-arc sec v2 DEM; e) LIA; f) Orthorectified HH. Bottom row: g) DPIPWE DEM; h) LIA; i) Orthorectified HH.

The low quality of the ASTER and SRTM DEMs can be seen in the blocky appearance in (a) and (d), compared to the smoother profile of the DPIPWE DEM in (g). As a result, there are artefacts present

in the LIA image derived from the ASTER DEM (jagged line running diagonally across lower part of image; b) which are subsequently translated in the orthorectified image (c). The LIA generated from the SRTM DEM (e) lacks the fine detail of the DPIPWE DEM derived LIA (h). Very bright areas in the orthorectified images are likely layover. Texture differences are evident in the orthorectified images Depending on the quality of the input DEM, feathering or stretching effects are observed where the process attempts to restore the position and brightness of backscattering elements. Stretching effects are most pronounced in the HH image orthorectified using the ASTER DEM (c).

The DEM used in orthorectification should be well scrutinised prior to use. Voids present in earlier versions of the 3 arc-second SRTM DEM, for example, can introduce odd artefacts in orthorectified images. These artefacts may take the form of spatial distortions in orthorectified data as illustrated in Figure 41. Voids should be filled prior to use in orthorectification, either through an interpolation process or by masking the values in the DEM and setting to a constant value. It should be noted that missing data or masked areas in the DEM will result in NaN values in the orthorectified image, and so it is best to have a complete void-free DEM for use in orthorectification. Later versions of the SRTM DEM are available where such areas have been in-filled using other elevation data. A higher quality DEM should be always be sourced, and many countries will soon have access to the 1 arc-second SRTM DEM, if not the TanDEM-X DEM.

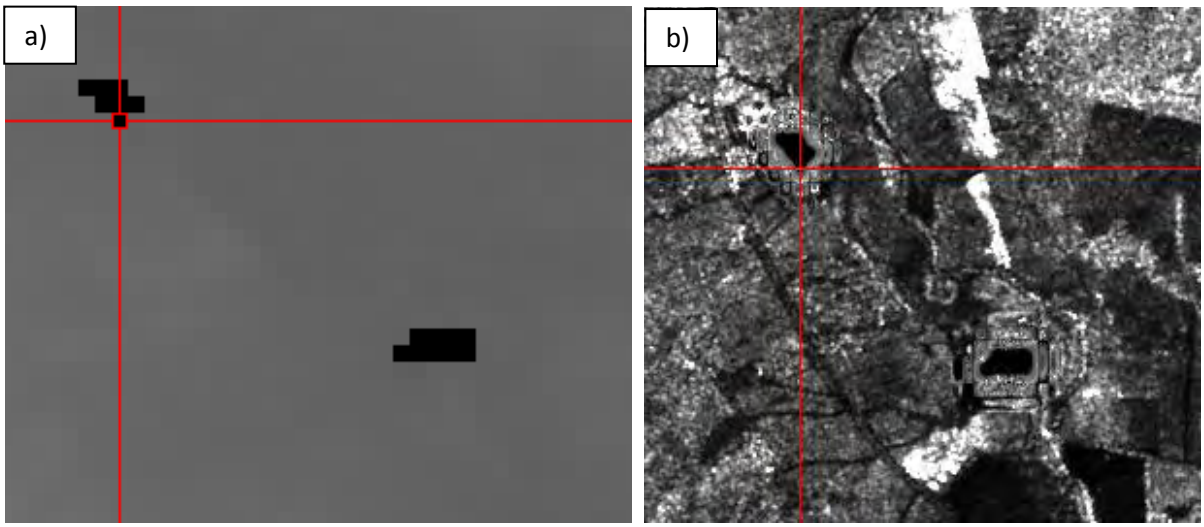

Figure 41. Artefacts in ALOS PALSAR HH data when orthorectified using an unfilled SRTM DEM: a) SRTM DEM with black areas corresponding to no data (value = -32768); and b) Resulting orthorectified HH image with distorted pixels surrounding void pixels in the DEM.

5.3 Registration accuracy assessment

The geographic accuracy of orthorectified images can be assessed both visually and statistically. Images can be resampled to match other airborne or satellite datasets of known higher location accuracy, and linked spatially for quick assessment of co-registration accuracy. Consistency in different parts of the image can be assessed by interactively linking displays and flicking between the two to assess any shifts in position. Alternatively, the position of accurately located GCPs sourced from GPS and field survey or through automated feature detection approaches can be compared to those on orthorectified images. The Root Mean Square Error (RMSE) provides an indication of registration accuracy with respect to the coordinate transformation method. Low values of RMSE are indicative of high registration accuracy.

As an example, co-registration accuracy between orthorectified ALOS PALSAR and Landsat TM data over NE Tasmania was assessed using feature based matching in a process developed by CSIRO (Perth). The routine performs an assessment of sub-pixel registration accuracy based on correlation matching between GCP features in 2 images (raw and base). The PALSAR data is resampled to 25 m pixels to match the Landsat TM and then inverted (greyscale) to generate features of similar brightness/contrast in both the SAR and base image (Landsat), and so optimise the correlation matching. GCPs are then identified on the base image and automatically located on the SAR image.

An example of the correlation summary and combined residuals plot is shown in Figure 42. The co-registration results show that 90 % of the GCPs achieving a high correlation between the 2 images have a registration accuracy of less than 1 pixel (Figure 42a). On average, sub-pixel accuracy between the Landsat TM and PALSAR image is achieved across the scene, and satisfactory co-registration in the western part of the scene is observed (i.e., GCP shifts observed in random directions; Figure 42b). GCPs located in the NE however indicate a significant and consistent shift between the 2 images. This may be due to issues during the orthorectification process of either the Landsat or SAR data, poor selection of GCPs in the NE or the result of genuine changes in land cover between the 2 acquisition dates.

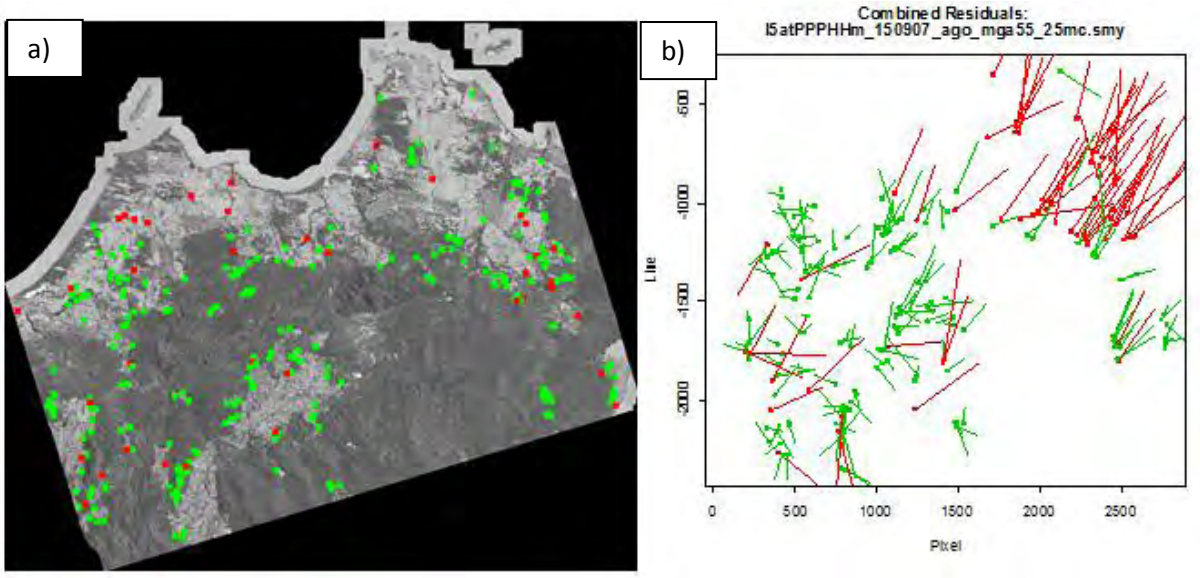

RMSE for all GCPs with corr ≥ 0.85 (232 GCPs)
Pixel: 0.61 Line: 0.71 Comb: 0.94
RMSE for best 90% of GCPs with corr ≥ 0.85
Pixel: 0.47 Line: 0.71 Comb: 0.77

Figure 42. Registration accuracy assessment based on correlation matching between GCPs identified on orthorectified Landsat TM (base) and ALOS PALSAR (raw) HH images: a) Location of GCPs on orthorectified PALSAR image: green dots indicate GCPs with high correlation (> 0.85), and red dots indicate a weaker correlation (< 0.85); and b) Plot of combined residual error, where the dot indicates the position of the GCP in the image, and the associated line provides indication of the displacement error and direction. The red colour denotes those GCPs with errors larger than 1 pixel, while green is used for the opposite.

Visual examples of displacement between orthorectified Landsat TM and PALSAR data are illustrated in Figure 43. Where a significant registration discrepancy occurs, distinct edge effects around feature

boundaries are observed. The SAR data (HH polarisation) is displayed in the green channel, and Landsat TM data (band 5) in the red channel.

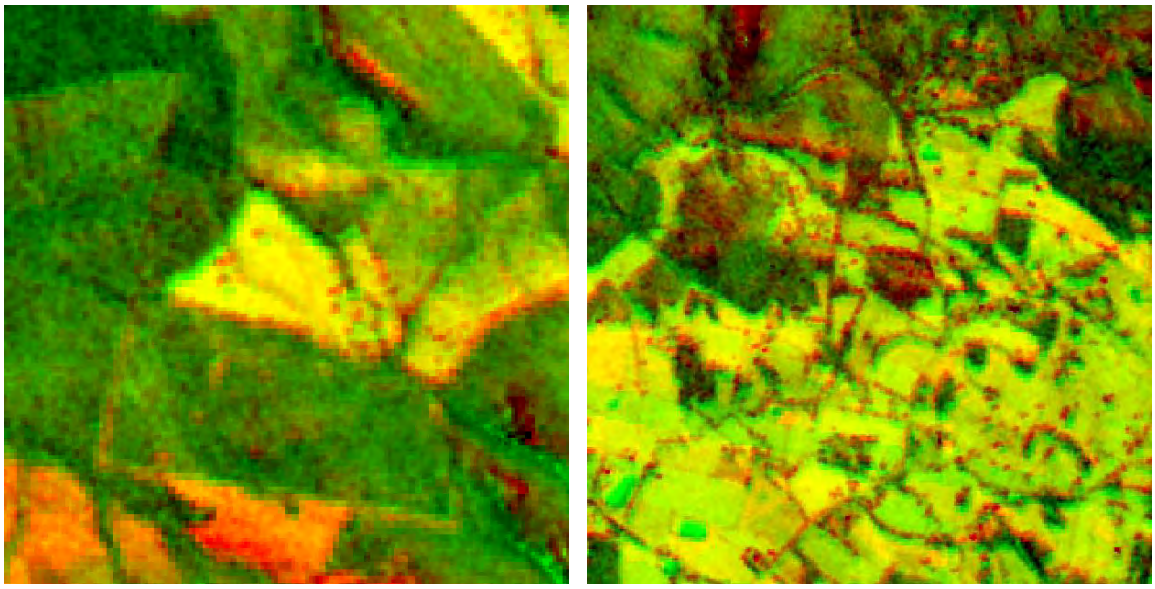

Figure 43. Examples of consistent registration discrepancy between ALOS PALSAR and Landsat TM data: distinct edge effects are observed around feature boundaries.

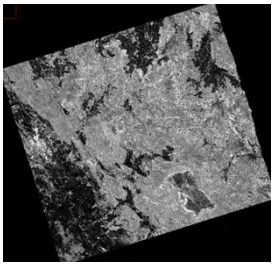

6. TERRAIN ILLUMINATION CORRECTION

This section describes the inherent geometric and radiometric distortions in SAR imagery acquired over steep terrain, and the procedures used to correct these effects. The information for this section has been extracted from Zhou *et al.* (2011). The Terrain Illumination Correction (TIC) routine developed by CSIRO (Zhou *et al.*, 2011) for correction of SAR data acquired for the Tasmania Demonstrator is also described.

6.1 SAR geometric parameters

Due to the side-viewing geometry of SAR, data acquired over steep terrain exhibits significant geometric and radiometric distortions. These distortions mask or reduce the useful backscatter information related to land cover or geophysical parameters. Post-processing of SAR data is required to correct these distortions and so increase the opportunities for land based mapping and monitoring using SAR data.

SAR backscatter is strongly dependent on the slope and aspect of the terrain. Variable terrain height induces both geometric and radiometric distortions within slant or ground range SAR imagery. For radiometry, the dominant effect is due to the variation in ground surface area contributing to the backscatter of each pixel. Corrections for geometric distortion are more widely available in commercial packages, but robust correction of radiometric distortions are either not available or use simplistic methods. Terrain Illumination Correction (TIC) is an essential pre-processing step prior to classification or analysis of SAR data with dependency on absolute values of the backscattering coefficient.

SAR imaging geometry exerts considerable influence on SAR backscatter intensities. Relevant geometric parameters as defined for a ground surface patch are illustrated in Figure 44, where:

- α - the slope angle
- β - the aspect of slope
- γ - the azimuth angle of the sensor
- θ - the nominal incidence angle
- φ - the local incidence angle
- ψ - the complementary to the smallest angle between the surface normal and the image plane
- u - the surface tilt angle in the range direction
- v - the surface tilt angle in the azimuth direction
- σ° - the original backscatter
- σ°_c - the radar backscatter corrected for the local incidence angle

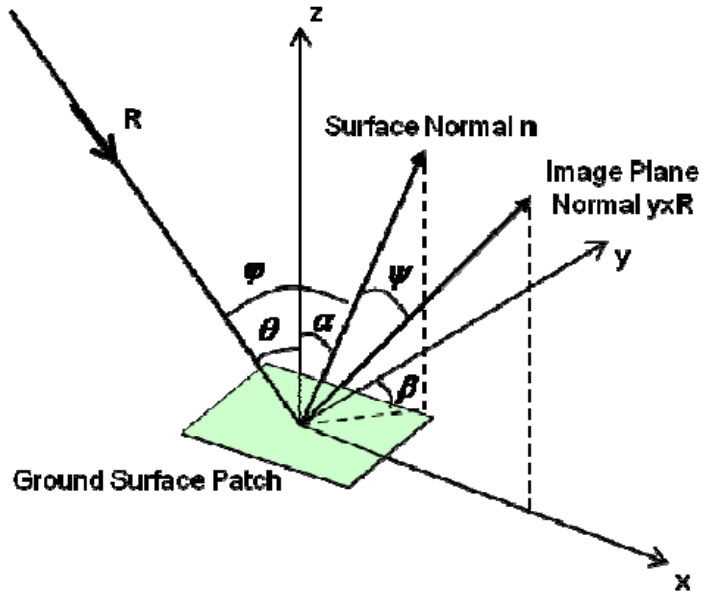

Figure 44. Scattering geometry of a ground surface patch on tilted (sloped) ground and its projection onto SAR image geometry.

Terrain slope and aspect are calculated directly from the input DEM, while other parameters are calculated based on the imaging geometry model. Terrain slope parameters are calculated using an estimation of the gradients in the 2 directions of the coordinate plane of the DEM. A 3x3 pixel window is typically used to calculate the gradients for the centre pixel. The local incidence angle (LIA; φ) is defined as the angle between the local surface normal and the look vector of the incident radar waves. The range component of the local incidence angle ($\theta + u$) is used to determine regions of active layover in the DEM, where u is defined as the angle between the vertical vector and the projection of the surface normal into the Doppler plane. The azimuth component of the LIA (v) is defined as the angle between the local surface normal and the Doppler plane in a perpendicular direction to it.

6.2 Common TIC models

Numerous theoretical and experimental studies in SAR scattering behaviour give rise to certain expectations in radar backscatter properties over vegetated surfaces as related to incidence angle. There are 3 published models that account for terrain induced radiometric variations over rough surfaces:

i. **Semi-empirical methods** - these employ simple trigonometric functions to model the angular dependence of backscatter without addressing complex interactions. Ulaby *et al.* (1986) proposed a simple backscattering model for largely vegetated (diffuse) surfaces, where:

$$\sigma^\circ(\varphi) = \sigma^\circ \cos^p(\varphi)$$

Both σ° and p are polarisation dependent. When p = 1, the scattering coefficient is dependent on $\cos\varphi$, which is the ratio of the projected area to the surface area. When p = 2, the model is based on Lambert's law for optics.

ii. **Statistical models** - wherein layers are represented by dielectric spaces containing random irregularities. Teillet *et al*. (1985) applied a *C* parameter, a function of the linear regression of slope *a* and intercept *b*:

$$\sigma^\circ = a.\cos\varphi + b$$

$$C = b / a$$

The C-correction model is thereby based on the statistical regression as in the following:

$$\sigma^\circ_c = \sigma^\circ \ (\cos\theta + C) / (\cos\varphi + C)$$

Where: σ°_c is radar backscatter corrected for LIA (φ), and σ° is the backscatter before correction.

iii. **Geometric models** - use the sine of LIA to correct the backscattering coefficient (e.g., van Zyl et al., 1993):

$$SCF = \sin\theta / \sin(\theta + u)\cos v$$

Where SCF is the slope correction factor, $\theta + u$ the LIA in range direction, and *v* the surface tilt angle in azimuth direction.

Kellendorfer *et al.* (1998) also proposed a geometric model which uses LIA (φ) to correct radiometric distortion, whereby:

$$\sigma^\circ_c = \sigma^\circ \ (\sin\varphi / \sin\theta)$$

6.3 CSIRO TIC routine

Given Tasmania's steep topography, terrain illumination correction was a necessary pre-processing step prior to classification. A modified TIC routine for SAR data acquired over forest areas on steep terrain was developed by CSIRO (Zhou *et al.,* 2011). A high resolution DEM and satellite position and tracking information are used to correct for illumination differences observed on forward and backward facing slopes in the presence of topography.

The correction is summarised as follows:

$$SCF = \sin(\theta + u)\cos v$$

$$\sigma^\circ_c = SCF^q . \beta^\circ$$

Where q ~$1/p$ (referring to Ulaby *et al.,* 1986), with a value between 0.5 - 1 for diffuse scattering, and β° (beta nought) is the real radar backscatter before processor-induced ellipsoid model nominal area values were applied. When SAR data is acquired over sloping terrain, there is a change in the radar cross section per unit area and a change in polarisation state (i.e., orientation of the radar wave). Compared to L-band HV, HH backscatter is more sensitive to terrain slope and typically sees more of the ground because of greater canopy penetration. As such, L-band HH is used to estimate the LIA (φ). The SCF is then used to correct the HV backscatter.

ALOS PALSAR FBD data acquired over NE Tasmania are used to illustrate the effect of TIC on radar backscatter (Figures 45 - 48). The effect of the TIC on FBD images is evident in the smoother appearance of the surface, where the terrain is seemingly flattened (Figures 45 and 46). A zoomed subset illustrates this flattening of terrain and change in backscattering coefficient (Figure 47). Prior to TIC, illuminated foreslopes appear quite bright and backslopes appear quite dark in HH (c) and HV (d) imagery. In TIC corrected data, the magnitude of the backscatter on foreslopes decreases (e and f; area within red box), while the backscatter increases slightly on the backslopes (e and f; area immediately to NE of red box).

The impact of TIC on backscatter originating from steep forested terrain is illustrated further using spatial profiles (Figure 48). Backscatter is reduced across Illuminated foreslopes (a and b) with low LIA (< 20°; d) and these appear darker in TIC images (i and j). Backscatter is slightly higher for

backslope areas with high LIA (> 60°) following TIC. The TIC has the effect of smoothing out the overall backscatter response across forward and backward facing slopes. Backscatter remains largely unchanged in flat areas, indicative of successful implementation of TIC.

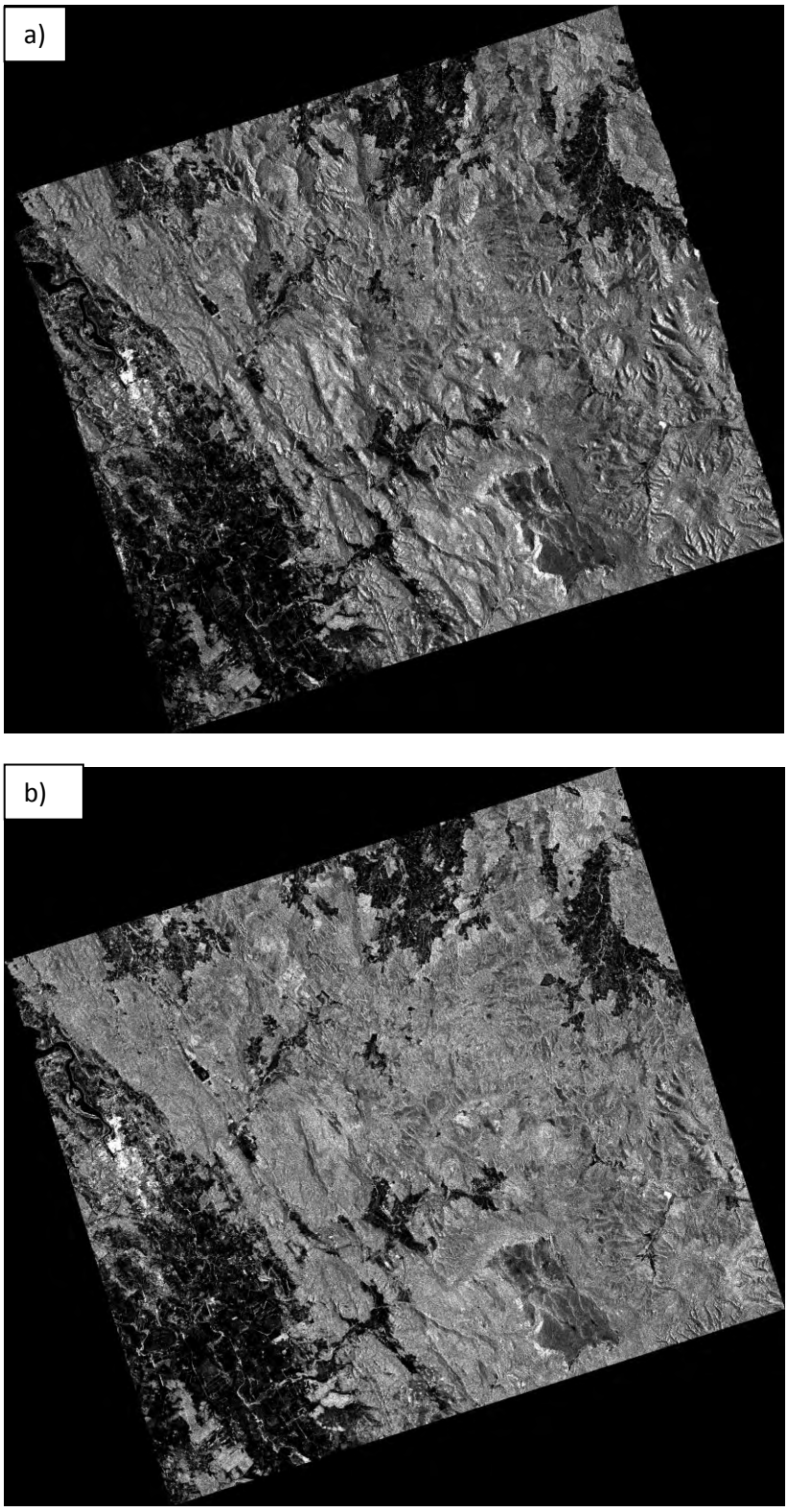

Figure 45. ALOS PALSAR HH data prior to (a) and after Terrain Illumination Correction (b).

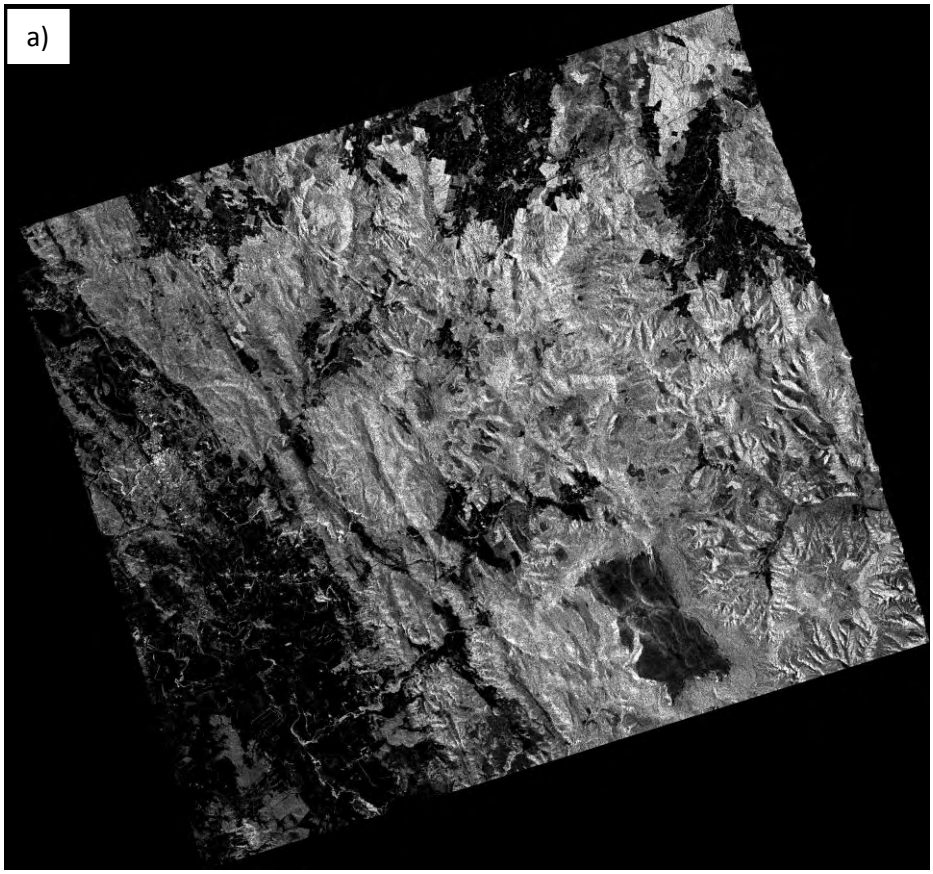

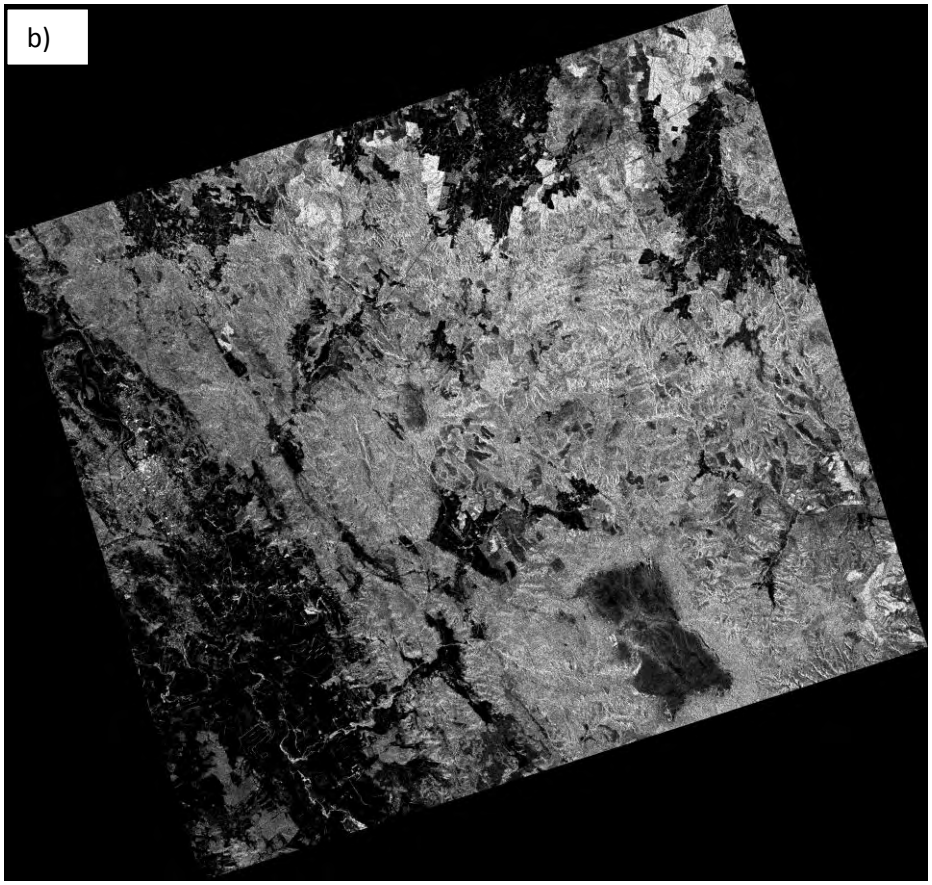

Figure 46. ALOS PALSAR HV data prior to (a) and after Terrain Illumination Correction (b).

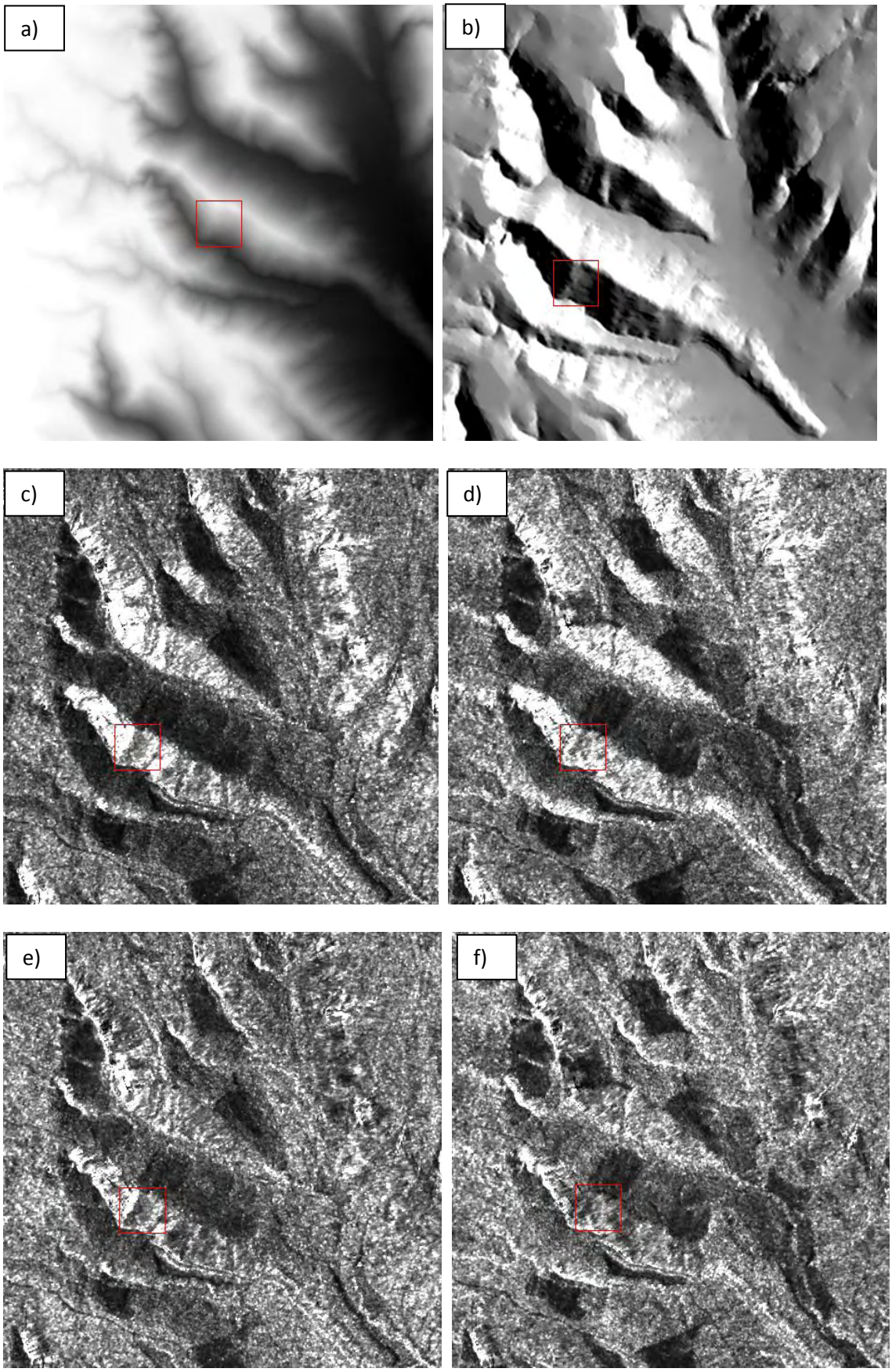

Figure 47. Subsets extracted over steep forested terrain illustrating application of TIC: a) DEM; b) LIA; c) Uncorrected HH image; d) uncorrected HV image; e) TIC HH image; and f) TIC HV image.

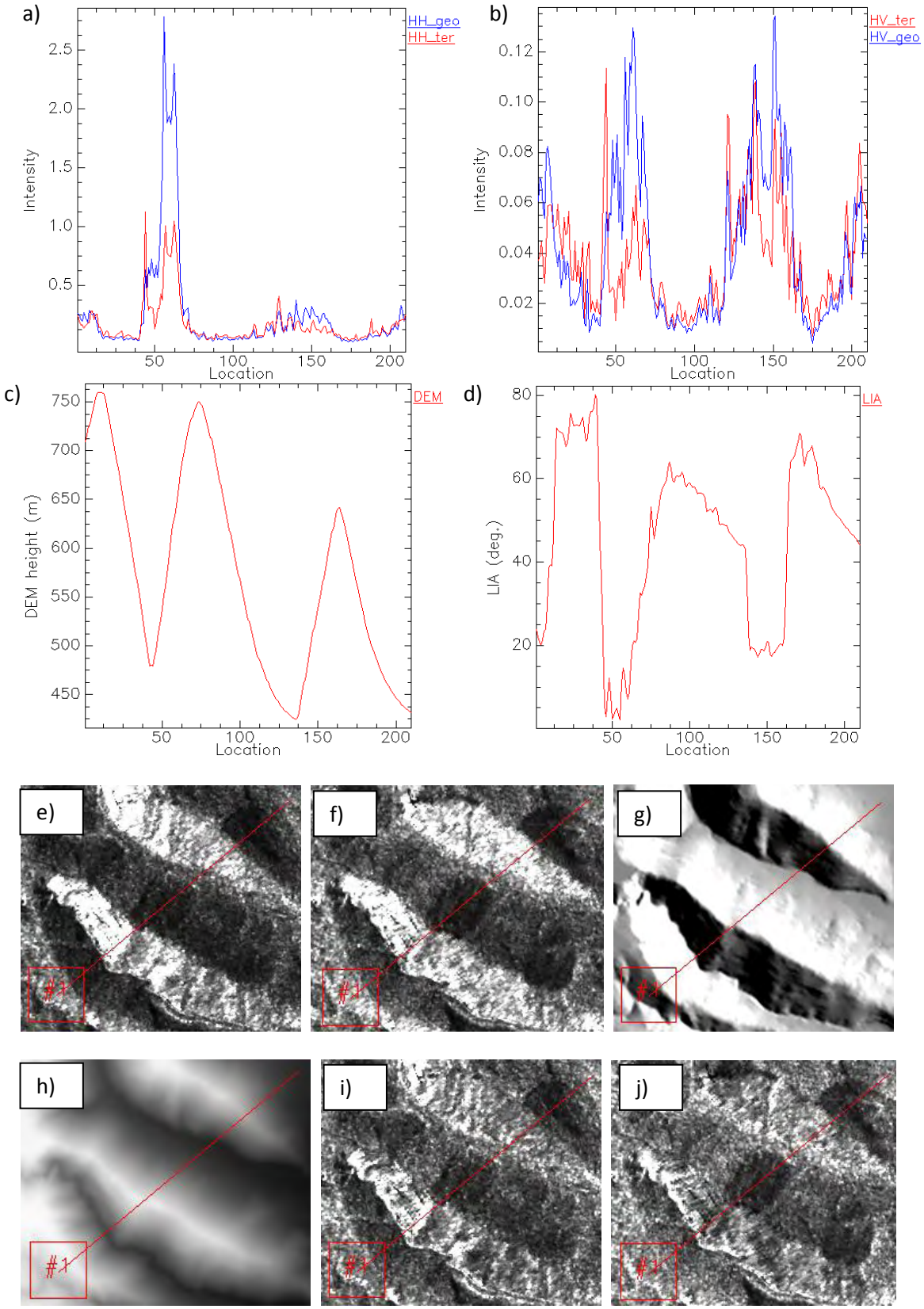

Figure 48. Illustration of changing backscatter for a profile extended across uncorrected and TIC ALOS PALSAR data. Profile extended across: a) Uncorrected (blue) and TIC (red) HH data; b) Uncorrected (blue) and TIC (red) HV data; c) DEM height profile; and d) LIA profile. Profile on image data: e) Uncorrected HH; f) Uncorrected HV; g) LIA; h) DEM; i) TIC HH; and j) TIC HV.

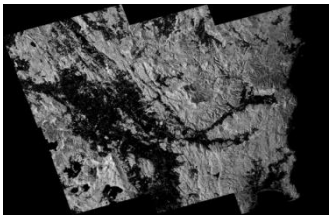

7. MOSAICKING

This section describes options for mosaicking calibrated SAR data to produce seamless, wall-to-wall mosaics.

7.1 Mosaicking strategies

Following orthorectification, radiometric calibration and terrain illumination correction, SAR data acquired over different satellite paths are typically mosaicked to produce wide-area coverage. Automated mosaicking methods are available in SARscape for this task. The methods are grouped in 2 categories:

i. Conventional mosaicking
   - Last pixel – in overlapping areas, the pixel values extracted from the last listed input image are represented in the mosaic
   - Mean – in overlapping areas, the average pixel value is taken
   - Optimal resolution – specific to mosaicking DEM data
   - Precision – specific to DEM and displacement maps
   - Feathering – in overlapping areas, a weighted average of the pixel values within a defined window is taken

ii. Gradient mosaicking – the amplitude ratio is estimated in overlapping areas and correction factors obtained by global optimization

Hereafter, our discussion is limited to SAR image data and so optimal resolution and precision mosaicking methods relevant to DEMs are excluded.

Dealing with SAR data acquired from overlapping paths is a complex process. A total of 51 ALOS PALSAR FBD images acquired over 8 neighbouring paths were required to cover Tasmania. Several hundred images from about 100 paths would be required to cover all of Australia. Choice of mosaicking strategy is dependent on the intended application, which for most involves further analysis, classification of land cover or estimation of biophysical properties. Optimal mosaicking involves minimal redistribution of backscatter values, and preservation of original data. That being the case, SARscape's last pixel method would be used in preference to the mean method. If mosaics are produced for visualisation purposes only, the choice of strategy is less important.

The timing of acquisition of all data required to produce wide-area coverage may impact the final mosaic. For example, the 8 paths of PALSAR data for Tasmania in 2007 were acquired over a 3 month period, between August and October. Neighbouring strips of data from these 8 paths were acquired, on average, about 5 – 7 days apart, up to a maximum of ~24 days apart. This is time enough for real on-ground change to have occurred in the overlapping area of neighbouring path images, due to, for example, land clearing or regrowth activity, and differences in backscatter would be observed. As well, the sensitivity of SAR backscatter to dielectric changes, e.g., an increase in soil or canopy moisture due to rainfall, could have noticeable impact through enhancement of the backscatter response. If rainfall occurred a few days prior to acquisition of the neighbouring strip,

backscatter would be higher across the strip and in the overlapping area, resulting in an obvious seam when mosaicked.

Despite application of averaging or feathering techniques when mosaicking neighbouring paths, the radiometric differences in overlapping areas arising from on-ground change cannot always be compensated for. Further, data processed using different core software releases can be significantly different radiometrically. Consideration needs to be given to initial data selection and mosaicking imagery acquired under similar conditions and using the same core software, together with appropriate use of mosaicking strategies that best minimise these effects.

7.2 Comparison of last pixel and gradient mosaic methods

Application of conventional (last pixel) and gradient mosaicking methods using ALOS PALSAR HH data is illustrated below. In the example, neighbouring, orthorectified TIC images from the same path are used as input to create a mosaic using the last pixel method (Figure 49). The result is not seamless, as illustrated in Figure 50. A jagged line is evident where one image has been overlain on the other. It is possible that the border of each image includes some 'bad pixels' with erroneous data, or depending on the core processor used to focus the SLC data, the same pixel on consecutive frames varies.

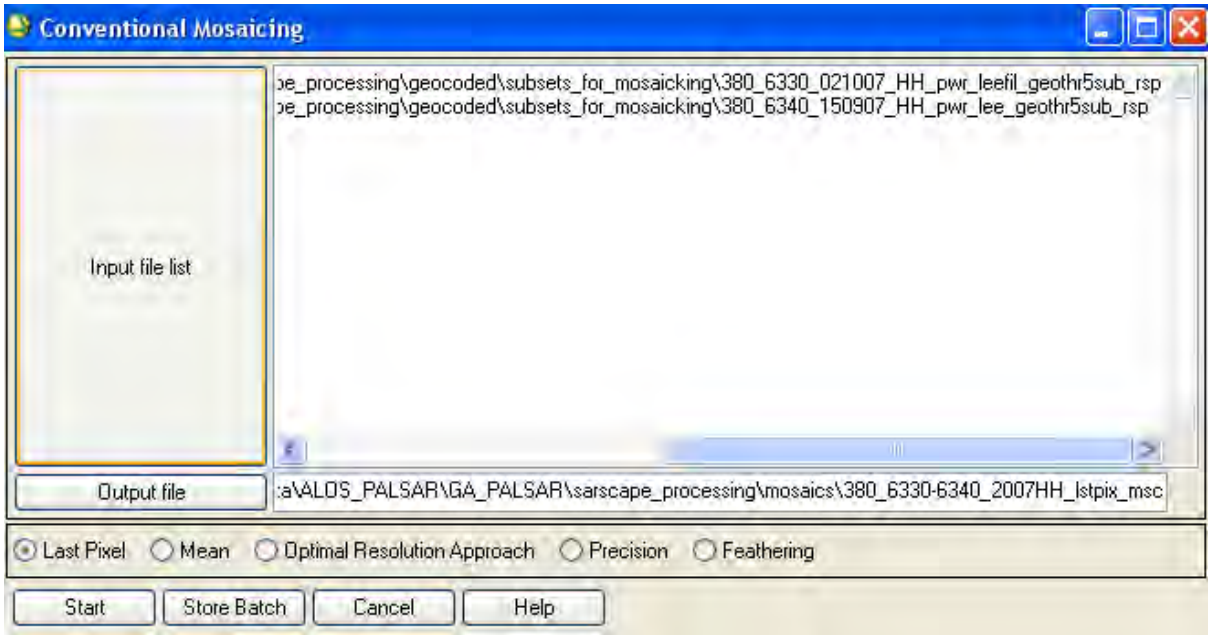

Figure 49. SARscape conventional mosaicking menu. In the example, 2 neighbouring ALOS PALSAR images from the same path are used as input to create a mosaic using the last pixel method.

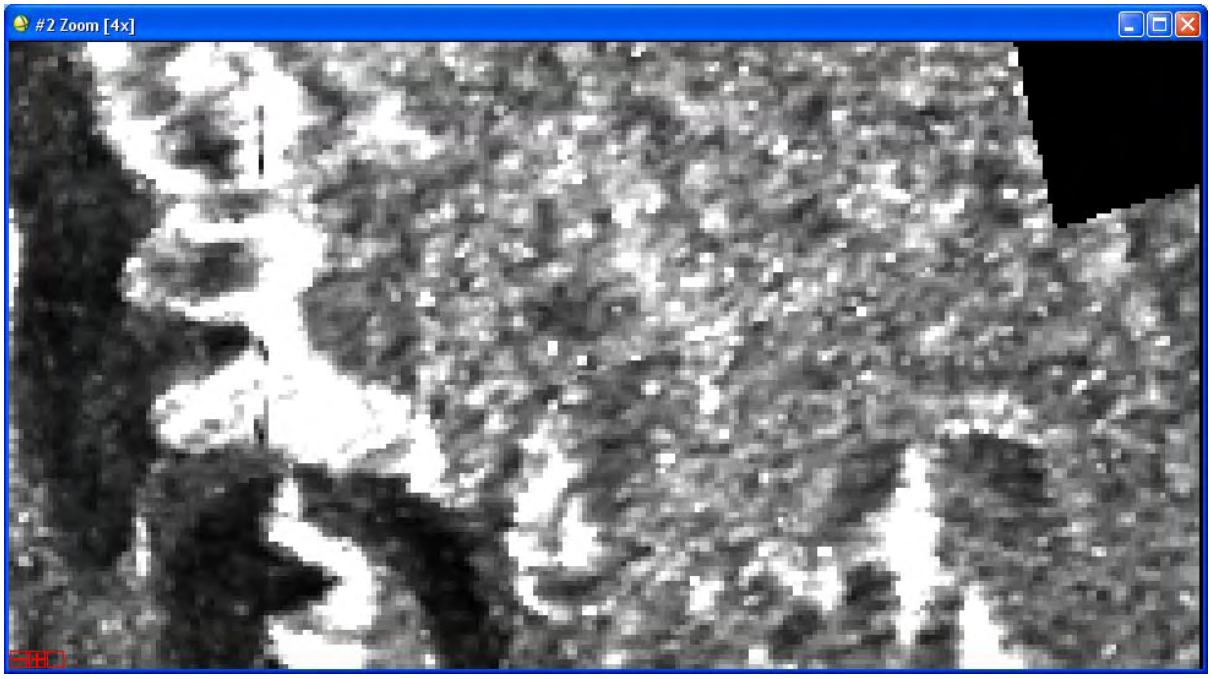

Figure 50. Illustration of seam line evident following mosaicking using last pixel method.

One solution is to cut the border pixels prior to mosaicking. This can be achieved manually by extracting a subset that excludes around 20 pixels near the edge. A polygon shapefile can be created in ENVI (Figure 51a) and used to extract the subset in SARscape's manual selection tool. The extracted subset has squared edges and is now suitable for mosaicking (Figure 51b).

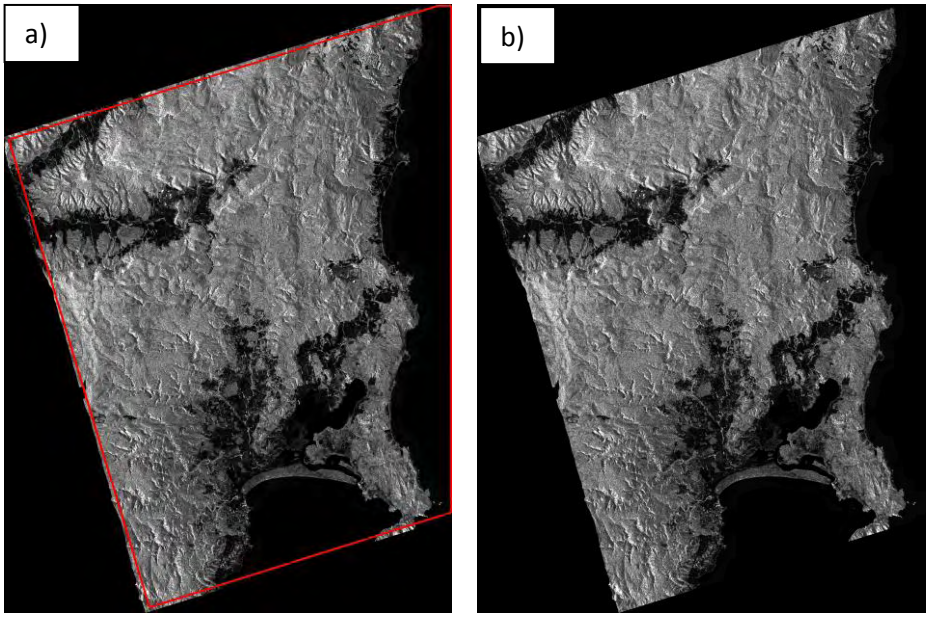

Figure 51. Extraction of subset prior to application of last pixel mosaic method: a) Vector outline overlain on orthorectified TIC imagery; and b) Extracted subset.

A more seamless result is observed when cut images are used as input to last pixel mosaicking (Figure 52). The jagged line evident in the mosaic generated using original (uncut) data (Figure 52a) does not appear in the mosaic generated using cut data (Figure 52b).

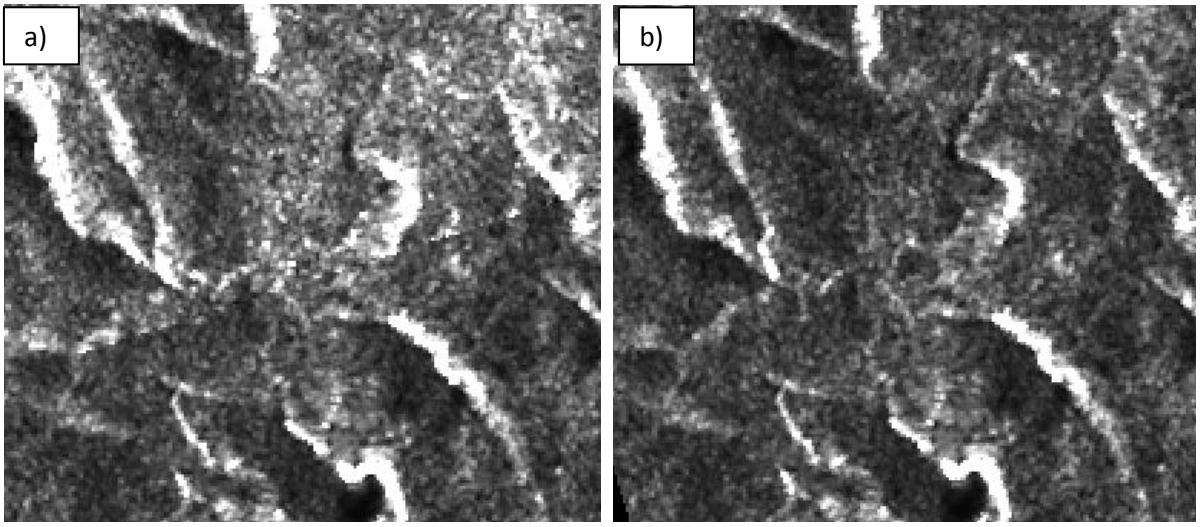

Figure 52. Mosaicking neighbouring images acquired along the same path using last pixel method: a) Images not cut prior to mosaicking; and b) Images cut prior to mosaicking. Minimal seam is evident when mosaicking cut images, compared to using original (uncut) images.

The problem is not observed when gradient mosaicking images acquired from the same path. No seam is evident when uncut (Figure 53a) or cut images (Figure 53b) are used as input to gradient mosaicking. Cutting all images prior to mosaicking does create straight edges however (Figure 54), which improves the visual quality of the final mosaic.

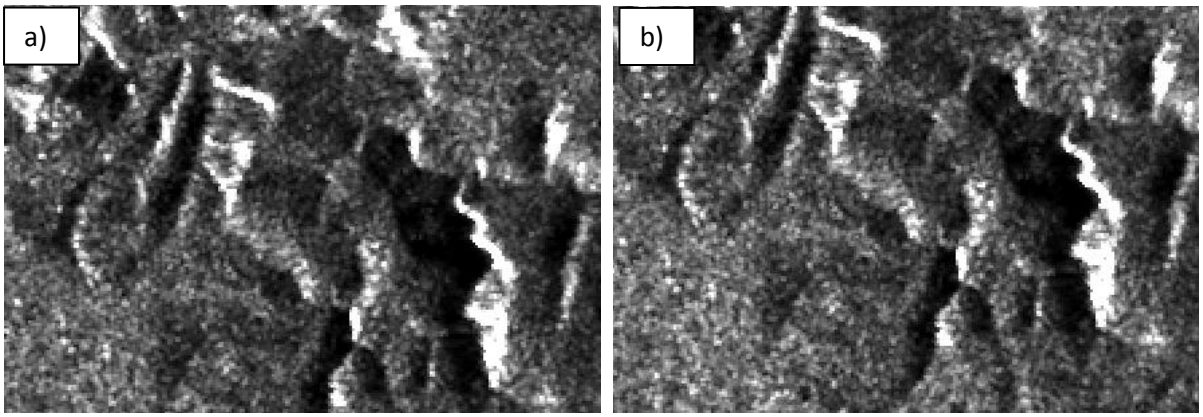

Figure 53. Mosaicking neighbouring images acquired along the same path using gradient mosaic method: a) Images not cut prior to mosaicking; and b) Images cut prior to mosaicking. Result is seamless in both cases.

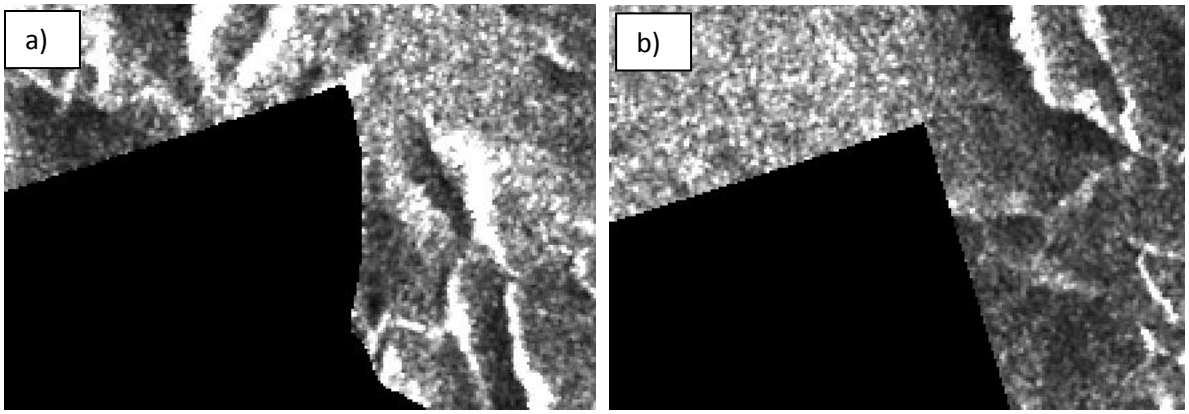

Figure 54. Cutting all images prior to mosaicking creates straight edges which improves the visual quality of the final mosaic: a) Jagged edge observed in lower part of mosaic where input images have not been cut prior to mosaicking; and b) Straight edged mosaic achieved by mosaicking cut images.

When gradient mosaicking, cut lines are automatically generated within the overlapping area. Edge detection techniques are used to identify a suitable location for the cut line, typically following image discontinuities so as to minimise, by calibrating image histograms, the seam line in the mosaic (Sarmap, 2012). Absolute calibration removes the constant and linear trends in all input data. The trends are calculated based on a number of points identified in overlapping areas. In a second refining step, local calibration is applied using Kriging interpolation on a new set of points located along each cut line where the images are mosaicked.

In the example below, 2 images acquired from neighbouring paths are used as input to generate a mosaic using the gradient method (Figure 55). Figure 56 shows the cut line overlain on the gradient mosaic.

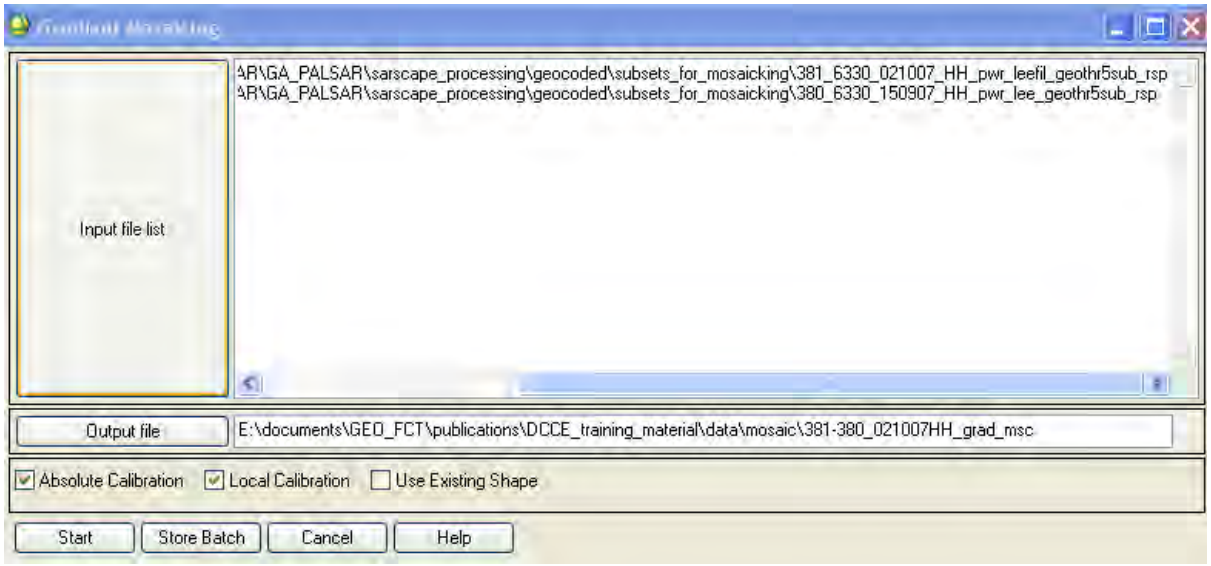

Figure 55. SARscape gradient mosaicking menu. In the example, 2 ALOS PALSAR images from neighbouring paths are used as input to create a mosaic using the gradient method.

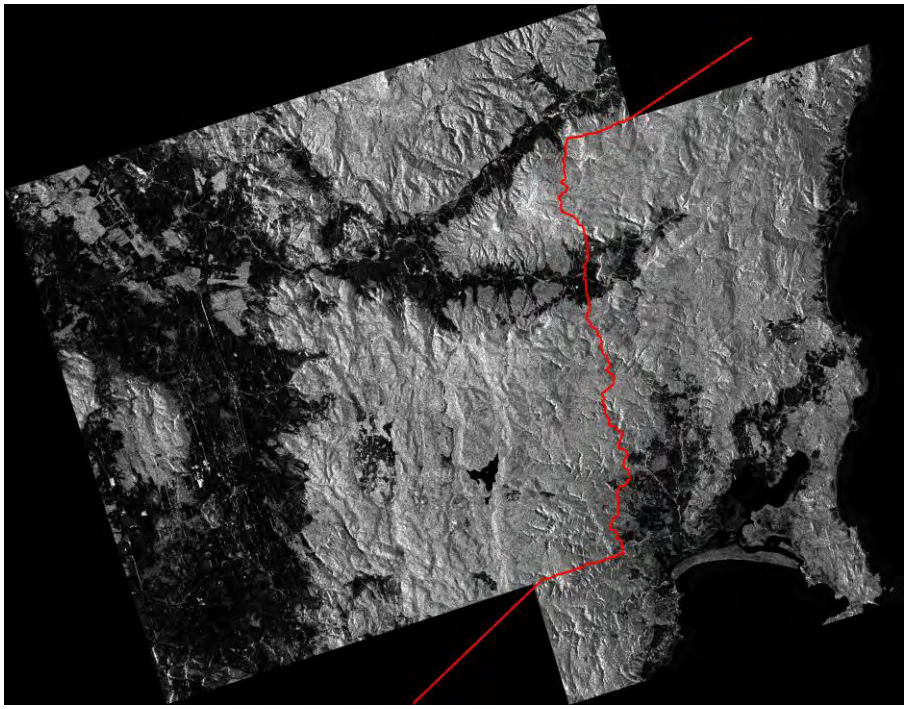

Figure 56. Cut line (in red) automatically generated when gradient mosaicking 2 images from neighbouring paths.

The effect of local calibration around the cut line is illustrated in Figure 57. A transect is extended across the original image and mosaicked data and intensity values compared. The trend in intensity mimics the original data on either side of the cut line. So to the left of the cut line, the intensity values in the mosaic mimic, albeit are slightly higher than the intensity values originating in image 381_6330 (Figure 57a; blue transect – original data vs. red transect – mosaicked data). To the right of the cut line, the intensity values in the mosaic are similar to 380_6330 (Figure 57a; black transect – original data, vs. red transect – mosaicked data). The overall distribution of backscatter values has not changed significantly however, as observed in the frequency histograms for the original and mosaicked data (Figure 58).

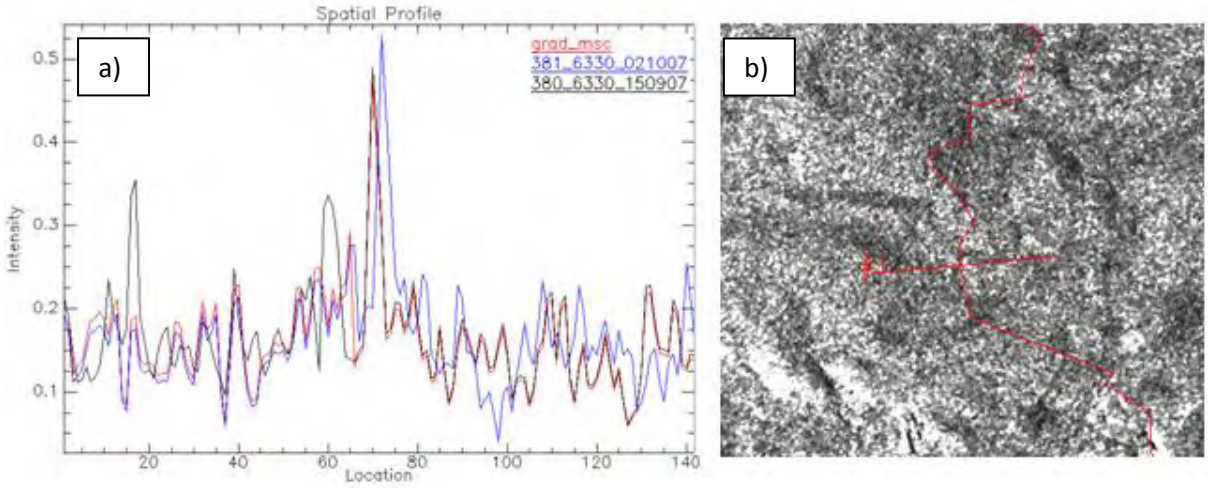

Figure 57. a) Comparison of intensity values extracted along a transect extending across the cut line in the gradient mosaic. The location of the transect (profile #1) is shown in (b).

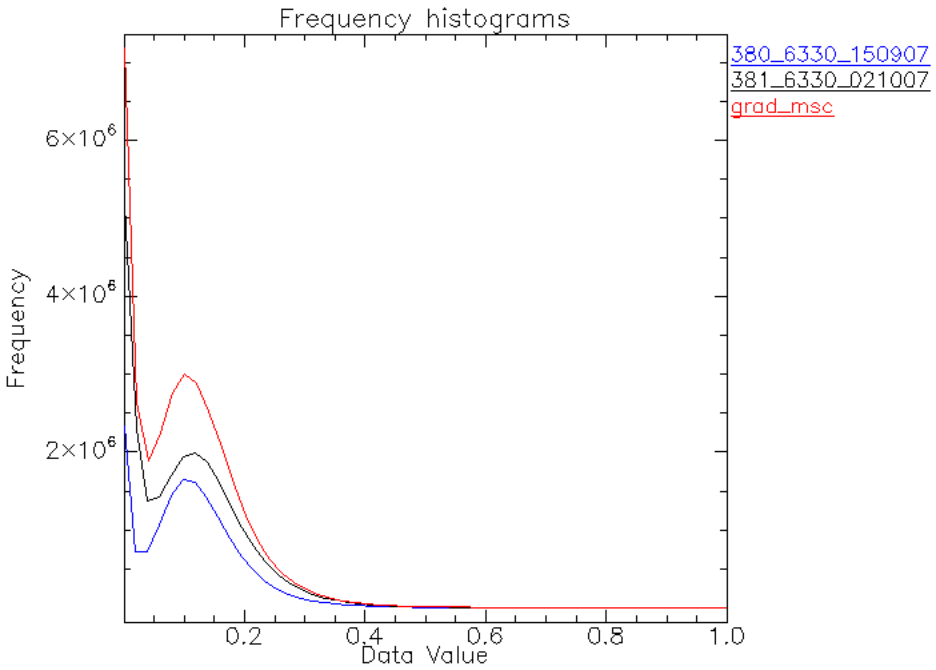

Figure 58. Frequency histograms for neighbouring images (380_6330 and 381_6330) and gradient mosaic.

7.3 Mosaicking strategy to generate wall-to-wall mosaics

The best approach to mosaicking SAR data and generating wall-to-wall seamless mosaics for Tasmania is as follows:

i. Cut the image border of each scene in case there are corrupt (bad value) pixels;

ii. Use last pixel overlay to mosaic all images along the same path (bottom to top) – repeat for all paths;

iii. Gradient mosaic the adjacent mosaicked paths (right to left), selecting absolute and local calibration.

Depending on PC processor and memory allocation, for step (iii), it may be necessary to generate 2 gradient mosaics comprising 4 paths each, and then gradient mosaic these. Ideally the process is completed in 1 gradient mosaic step.

The complete wall-to-wall mosaics generated using ALOS PALSAR, RADARSAT-2 and ENVISAT ASAR data for 2009 are presented in Figures 59 – 61.

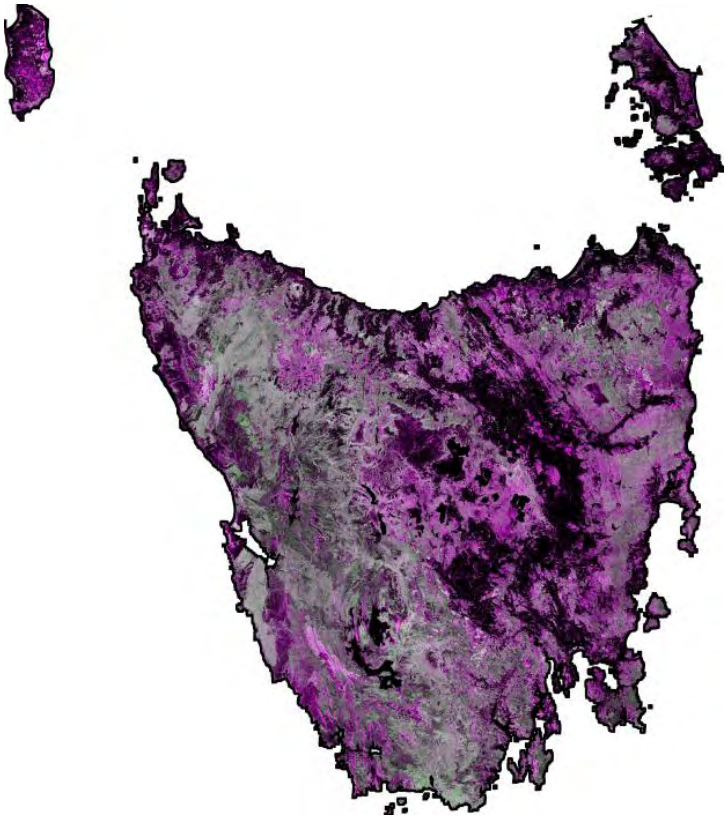

Figure 59. ALOS PALSAR mosaic for 2009: HH:HV:HH in RGB.

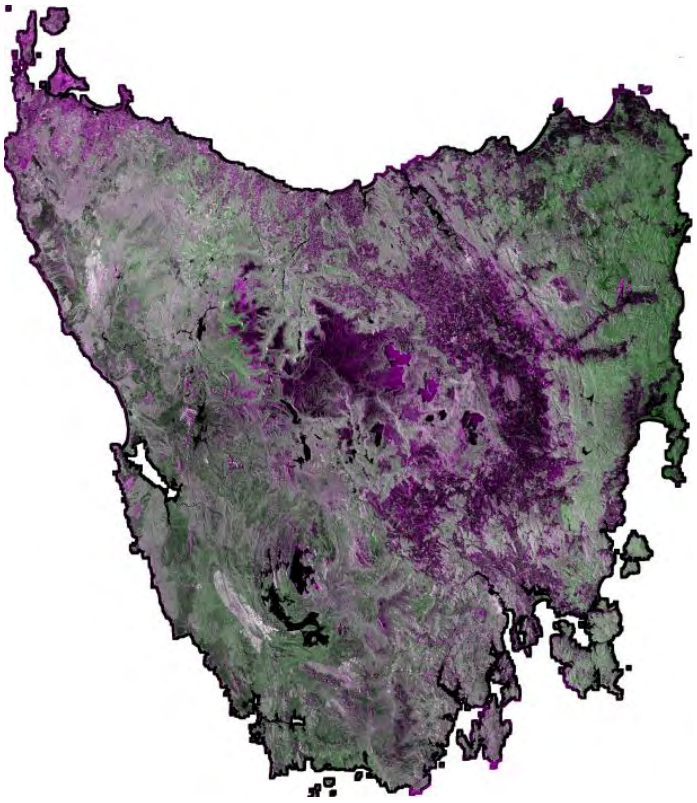

Figure 60. RADARSAT-2 mosaic for August, 2009: VV:VH:VV in RGB.

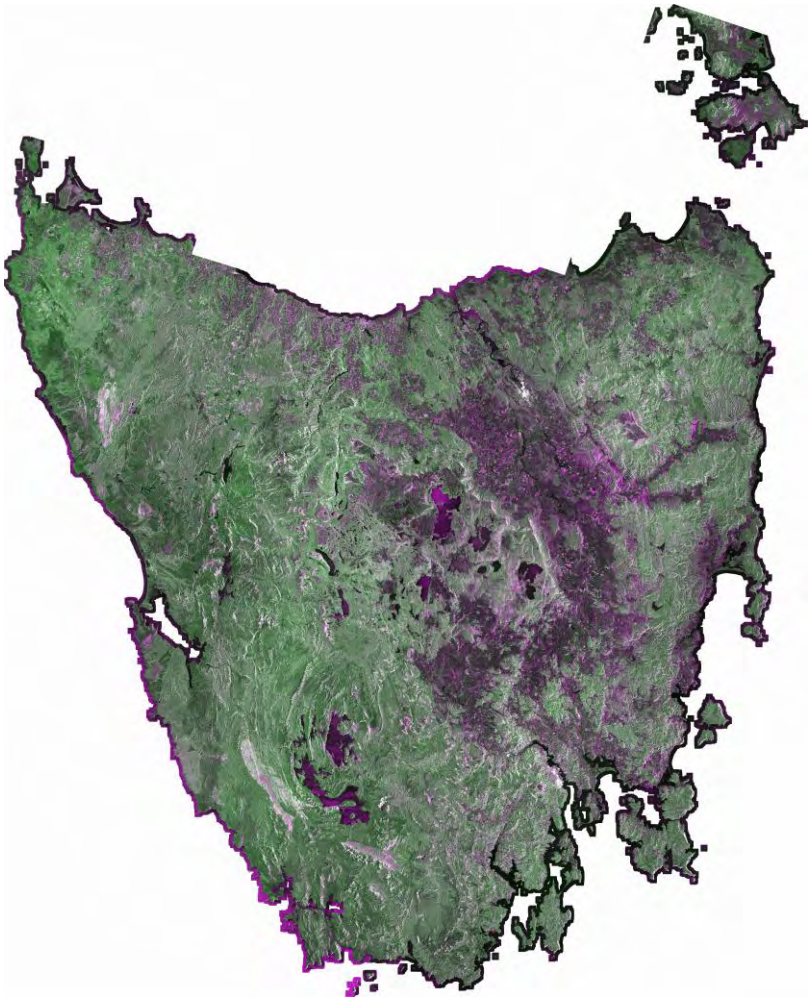

Figure 61. ENVISAT ASAR mosaic for July – Sept, 2009: VV:VH:VV in RGB.

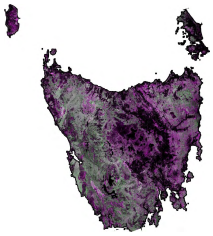

8. IFCI RA SAR PROCESSING SUMMARY

This section summarises the pre-processing steps applied to SAR data to generate seamless, wall-to-wall, orthorectified, radiometrically calibrated and terrain illumination corrected mosaics suitable for analysis of land cover.

8.1 SAR pre-processing workflow

The flowchart from Section 2 is copied here as it illustrates the adopted workflow for pre-processing all SAR data acquired under the IFCI RA Tasmania Demonstrator (Figure 62). SARscape was the software of choice for IFCI RA and was used to import, multi-look, co-register, orthorectify, radiometrically calibrate and mosaic SAR data. Speckle filtering was applied in ENVI. Terrain Illumination Correction (TIC) was applied using code developed by Zhou *et al.* (2011).

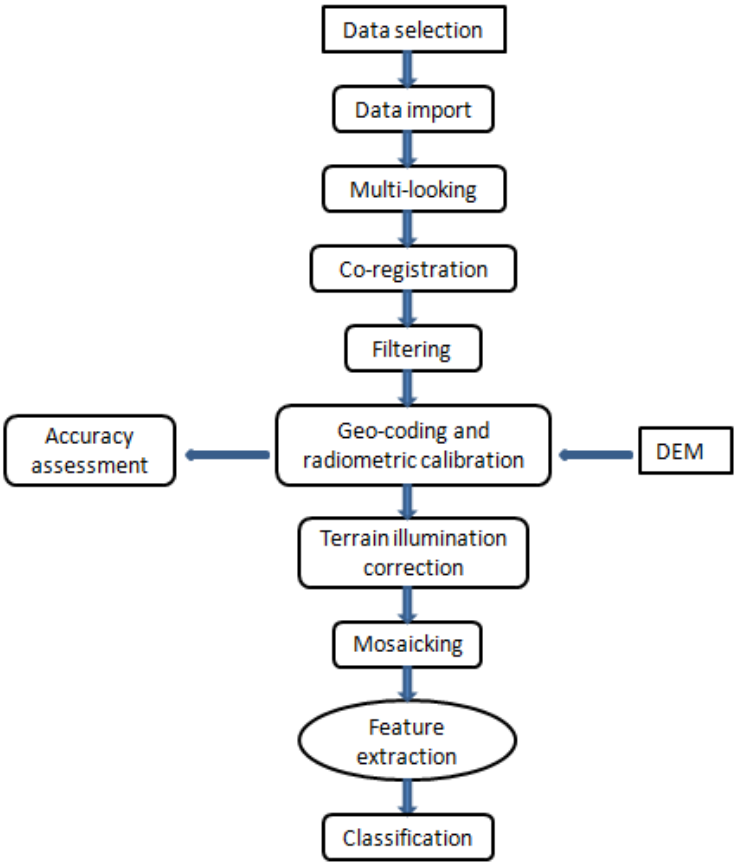

Figure 62. Adopted workflow for pre-processing SAR data acquired under IFCI RA Tasmania Demonstrator.

The following sequence of steps is applied:

i. Data selection
   - Archives are consulted for suitable time-series ALOS PALSAR (2007 – 2011), RADARSAT-2 (2009 – 2010) and ENVISAT ASAR (2009) data.
   - Data are requested in SLC level 1.1 CEOS format.

ii. Data import
   - SLC data are imported through the SARscape standard data formats utility.
   - SARscape generates its own unique set of headers associated with the SLC data.

iii. Multi-looking
   - In SARscape, SLC data are multi-looked using appropriate factors in range and azimuth. The number of looks is based on the desired output geocoded pixel size (set in program defaults prior to running tool).
   - ALOS PALSAR FBD, RADARSAT-2 and ASAR datasets will be orthorectified and resampled to 12.5 m spatial resolution for comparison. The program default for output geocoded pixel size was set to 12.5 m. Appropriate multi-looking factors were applied as follows: 4 looks azimuth, 1 look in range (ALOS PALSAR FBD and PLR), 3 looks azimuth, 1 look range (RADARSAT-2) and 3 looks azimuth, 1 look range (ASAR).
   - ALOS PALSAR FBS data will be orthorectified and resampled to 10 m spatial resolution. The following multi-looking factors were applied: 3 looks azimuth, 1 look in range.

iv. Co-registration
   - Multi-date slant ranges images are automatically co-registered in SARscape.
   - The smallest image (least spatial extent) is used as the reference image.
   - GCPs are used for images dominated by water and not land.

v. Filtering
   - Lee filtering is applied in ENVI using a multiplicative model with appropriate factors to the input data.
   - ALOS PALSAR FBD and PLR data are filtered using a 3x3 window, noise mean of 1 and noise variance of 0.25.
   - ALOS PALSAR FBS data are filtered using a 3x3 window, noise mean of 1 and noise variance of 0.33.
   - RADARSAT-2 data are filtered using a 3x3 window, noise mean of 1 and noise variance of 0.33.
   - ASAR data are filtered using a 3x3 window, noise mean of 1 and noise variance of 0.33.
   - Filtered images are imported back into SARscape as SARscape original files, using the multi-looked file as reference so that header information is preserved.

vi. Geocoding and radiometric calibration
   - Filtered images are orthorectified (terrain geocoded) in SARscape using a 25 m spatial resolution DEM available through DPIPWE.
   - 4^{th} order cubic convolution is selected as the resampling method.
   - Radiometric calibration and normalisation is applied. Calibration of the scattering area uses Local Incidence Angle (LIA) information, and normalisation applies a semi-empirical correction.
   - LIA images and layover/shadow masks are produced as additional outputs.

vii. Co-registration accuracy assessment

- GCPs available from Forestry Tasmania are used to assess the location accuracy of orthorectified images in the NE of the State.
- Visual assessment of co-registration accuracy is undertaken using Landsat TM data available through CSIRO NCAS.
- Correlation matching is applied to select SAR and Landsat images to assess co-registration accuracy in different parts of the State. RMSE and the magnitude and direction of any displacement is calculated.

viii. Terrain Illumination Correction (TIC)

- TIC of orthorectified data is applied using code developed by Zhou *et al.* (2011).
- TIC data are imported back into SARscape for mosaicking.

ix. Mosaicking

- The image border of each scene is cut to exclude corrupt (bad value) pixels. A polygon is manually identified on each image in ENVI and saved as a vector file (shapefile). SARscape's manual selection tool is used to cut each image using the corresponding vector polygon.
- The last pixel overlay method is used to mosaic all cut images belonging to 1 path (from bottom to top). All path mosaics are generated in this way.
- The gradient method is used to mosaic adjacent path mosaics (from right to left), selecting absolute and local calibration to minimise the seam lines.

x. Feature extraction and classification

- The wall-to-wall mosaics generated through application of steps (i) – (ix) are now ready for analysis. Feature extraction and classification will be dealt with in Volume II.

9. REFERENCES

ITT Visual Information Solutions. 2010. Exploring the SARscape modules for ENVI. Outreach Services, ITT VIS (www.ittvis.com).

Kellndorfer J., Pierce, L. E., Dobson, M.C. and Ulaby, F.T. 1998. Toward consistent regional-to-global-scale vegetation characterization using orbital SAR systems. *IEEE Transactions on Geoscience and Remote Sensing*, 36, 5, pp. 1396– 1411.

Lee, J-S., Wen, J-H., Ainsworth, T.L., Chen, K-S. and Chen, A.J. 2009. Improved sigma filter for speckle filtering of SAR imagery. *IEEE Transactions on Geoscience and Remote Sensing*, 47, 1: 202-213.

Lee, J.S., Grunes, M.R. and De Grandi, G. 1997. Polarimetric SAR speckle filtering and its impact on classification. Proceedings of IGARSS, held in Singapore, Aug 308, 1997.

Lucas, R., Armston, J., Fairfax, R., Fensham, R., Accad, A., Carreiras, J., Kelley, J., Bunting, P., Clewley, D., Bray, S., Metcalfe, D., Dwyer, J., Bowen, M., Eyre, T., Laidlaw, M. and Shimada, M. 2010. An evaluation of the ALOS PALSAR L-band backscatter - above ground biomass relationship Queensland, Australia: Impacts of surface moisture condition and vegetation structure. *IEEE Journal of Selected Topics in Applied Earth Observations and Remote Sensing*, 3, 4: 576-593.

Sarmap. 2009. SAR Guidebook: Synthetic Aperture Radar and SARscape. Sarmap, Aug, 2009.

Sarmap. 2012. SARscape v4.4 Help Manual. Sarmap, Feb 2012.

Teillet, P.M., Guindon, B., Meunier, J.F. and Goodenough, D.G. 1985. Slope-aspect effects in Synthetic Aperture Radar imagery. *Canadian Journal of Remote Sensing*, 11, 1, pp. 39-50.

Ulaby, F.T., Moore, R.K. and Fung, A.K. 1986. Microwave Remote Sensing, Active and Passive, vol III. Norwood, MA, Artech House.

Ulaby, F.T and Dobson, C. 1989. Handbook of Radar Scattering Statistics for Terrain. Artech House.

van Zyl J.J. 1993. The effect of topography on radar scattering from vegetated areas. *IEEE Transactions on Geoscience and Remote Sensing*, 31, 1, p.p. 153–160.

Zhang, Z.H., Prinet, V. And Ma, S.D. 2002. A new method for SAR speckle reduction. Proceedings of IGARSS, held in Toronto, Canada, June 24-28, 2002.

Zhou, Z-S., Lehmann, E., Wu, X., Caccetta, P., McNeill, S., Mitchell, A. Milne, A., Tapley, I. and Lowell, K. 2011. Terrain slope correction and precise registration of SAR data for forest mapping and monitoring. Proceedings of the 34th International Symposium on Remote Sensing of Environment (ISRSE), 11-15 April, Sydney.

10. ACKNOWLEDGEMENTS

- The Sarmap team, particularly Francesco Holecz, Stefano Monaco and Alessio Cantone – for their ongoing support and technical assistance with SARscape.

- IFCI RA CSIRO – contribution from Zheng-Shu Zhou in developing the Terrain Illumination Correction (TIC) routine, and Eric Lehmann in SAR and interoperability processing.

- SAR data was provided by CEOS member agencies through agreements with GEO FCT.

- JAXA K&C for provision of ALOS PALSAR data.

- Geoscience Australia (GA) for provision of ALOS PALSAR data.

- Forestry Tasmania – provision of GCPs from a LiDAR control survey for use in registration accuracy assessment.

- Tasmania DPIPWE – provision of state-wide DEM for use in orthorectification of SAR data.

- The Department of Climate Change and Energy Efficiency (DCCEE) for supporting and funding the project.